PVTX and Raman Spectral Properties of Fluids at Elevated Pressures and Temperatures

David Matthew Sublett Jr.

Dissertation submitted to the faculty of the Virginia Polytechnic Institute and State
University in partial fulfillment of the requirements for the degree of

Doctor of Philosophy
In
Geosciences

Robert J. Bodnar, Chair
Mark J. Caddick
Ryan Pollyea
Matthew Steele-MacInnis

December 17th, 2019
Blacksburg, VA

Keywords: Fluids, Microthermometry, Raman Spectroscopy, Intermolecular interactions

PVTX and Raman Spectral Properties of Fluids at Elevated Pressures and Temperatures

David Matthew Sublett Jr.

ABSTRACT

Fluids are associated with a wide range of physical and chemical processes in the Earth, including transporting and concentrating important ore elements such as Cu, Au, Zn, and Pb. Significant amounts of fluid may be generated as a result of dehydration or decarbonation reactions, and the volatile content of a magma is directly linked to the explosivity of eruptions. In most cases, small amounts of the fluids involved in the formation or alteration of rocks are trapped within minerals in the form of fluid inclusions. These fluid inclusions may be studied to understand the composition and pressure and temperature of the original fluid involved in the geologic process of interest, however, an understanding of the composition of the fluid as well as how the fluid behaves under changing pressure and temperature conditions is essential to reconstruct the fluid evolution path based on data obtained from fluid inclusions. Several analytical techniques are involved in the study of fluids, including fluid inclusion microthermometry and Raman spectroscopy. Microthermometry is the heating/cooling of fluid inclusions to observe and record temperatures of phase changes which, in turn, are used to determine properties such as salinity (based on the freezing point depression of liquid), or density based on the temperature at which all phases within the fluid inclusion homogenize to a single phase. Raman spectroscopy is a non-destructive analytical technique that measures the vibrational frequency of molecules in a given material. The Raman spectral properties of fluids act as a "fingerprint" of the chemical species within the fluid and serve to identify both the presence of chemical species, such as H_2O, N_2, CO_2, and CH_4, and the density of the fluid. Microthermometric and Raman spectroscopic experiments involving synthetic fluid systems are necessary to elucidate the pressure-volume-temperature-composition (*PVTX*) and Raman spectral behavior of the fluid systems, which then aids in the study and characterization of natural fluids.

In chapter 1, the partitioning of NaCl and KCl between coexisting immiscible fluid phases during boiling is experimentally determined at temperatures and pressures

relevant to magmatic-hydrothermal systems using synthetic fluid inclusions. The partitioning behavior is then combined with literature data to calculate the Na/K ratio of the original silicate melt phase in a magma body before the exsolution of a fluid phase. In chapter 2, we explore the Raman spectral behavior of N_2, CO_2, and CH_4 in pure, single-component systems from *PT* conditions corresponding to the liquid-vapor curve to elevated temperatures and pressures, and relate the changes in the spectral behavior to changes in the bonding environment of the molecules through intermolecular attraction and repulsion. In chapter 3, the observations and relationships determined for pure fluids and described in chapter 2 are used to explore the Raman spectral properties of N_2, CO_2, and CH_4 in the N_2-CO_2-CH_4 ternary system and the manner in which the spectral behavior of each component in the system varies with changing temperature, pressure, molar volume, and fugacity.

PVTX and Raman Spectral Properties of Fluids at Elevated Pressures and Temperatures

David Matthew Sublett Jr.

GENERAL AUDIENCE ABSTRACT

Water and other fluids play an important role in the formation of mineral deposits that are the source of the many metals, such as copper, silver, gold, and others, that are needed by a modern technological society. In addition, water and other fluids affect the way rocks behave under stress and can promote earthquakes and influence the explosivity of volcanoes. When minerals in a rock form, often small amounts of the fluid will be trapped within the minerals in the form of fluid inclusions. These fluid inclusions contain samples of the fluid involved in the geologic process of interest and can be studied using a variety of methods to determine the chemistry and the temperature and pressure conditions of rock formation. Two of the many methods used to study fluid inclusions are microthermometry and Raman spectroscopy. Microthermometry involves heating and/or cooling the fluid inclusion while it is being observed on a microscope, and this method can be used to determine the salinity of water in the inclusion and the fluid density. The density of the fluid may then be used to determine the pressure or temperature at which the fluid was encapsulated into the rock, and by extension the temperature and pressure at which the rock formed. Raman spectroscopy is an analytical technique in which a rock or fluid is illuminated using a laser. The laser light interacts with the rock or fluid and gains or loses energy, and this change in energy serves as a “fingerprint” to identify the molecules in the rock or fluid. The Raman spectrum can also be used to determine fluid density because the signal generated when the laser interacts with the fluid depends on the density of the fluid. Experiments on fluids at carefully-controlled laboratory conditions are necessary to understand the behavior of fluids trapped in natural samples.

In chapter 1, the preference of sodium and potassium to go into either a liquid or a gas phase during boiling at high pressures and temperatures is determined. In chapter 2, gases containing only nitrogen, carbon dioxide, or methane are studied using Raman spectroscopy and the changes in the Raman behavior of the gases with changing pressure and temperature are related to molecular interactions. In chapter 3, the results from

chapter 2 are used to understand the Raman behavior of nitrogen, carbon dioxide, and methane in gas mixtures as pressure and temperature are changed and how this relates to the interactions of the molecules.

Acknowledgements

I want to thank my advisor, Bob, for all of his support throughout the years. I am a much better scientist having worked with Bob than I ever would have been without. I also want to thank Charles Farley for showing me how to operate and fix many of the apparatuses that I used, and the many enjoyable conversations while using and fixing them. The graduate students in the VT Fluids group, both past and present, have also made my time as a graduate student quite enjoyable, providing entertaining conversations on science, pedagogy, and, occasionally, nothing really important at all.

I am eternally grateful to my family for always supporting my academic endeavors, especially my Papaw, who instilled in me a love of nature, history, and the pursuit of knowledge. Finally, I want to thank my wife, Jennica Sublett, for all of her love and support. If it was not for having her in my life, I do not know where I would be, but it certainly would not be writing a Ph. D. dissertation.

Attributions

This dissertation includes the collaborative work of my co-authors who contributed to these chapters which appear or are expected to appear as articles in peer-reviewed journals.

Chapter 1 was published as Sublett D. M., Gonzalez M. M., and Bodnar R. J. (2018) Synthetic fluid inclusions XXI: Partitioning of Na and K between liquid and vapor in the H_2O-NaCl-KCl system at 600-800°C and 500-1000 bars. *Geochim. Cosmochim. Acta* **235**, 173-188. ***D. M. Sublett*** was responsible for synthesizing and measuring fluid inclusions, and writing the manuscript. *M. M. Gonzalez* provided synthetic fluid inclusion samples. *R. J. Bodnar* contributed to data interpretation and the preparation and editing of the manuscript.

Chapter 2 was (recently) accepted for publication as Sublett D. M., Sendula E., Lamadrid H., Steele-MacInnis M., Spiekermann G., Burruss R. C., and Bodnar R. J. (In press) Shift in the Raman symmetric stretching band of N_2, CO_2, and CH_4 as a function of temperature, pressure, and density. *J. Raman Spec.* ***D. M. Sublett*** was responsible for collecting the Raman spectral data and writing the manuscript. *E. Sendula* provided measurements on CO_2 above 200°C and contributed to data interpretation and the preparation and editing of the manuscript. *H. Lamadrid, M. Steele-MacInnis, G. Spiekermann, R. C. Burruss,* and *R. J. Bodnar* contributed to data interpretation and the preparation and editing of the manuscript.

Chapter 3 will be submitted to the *Journal of Raman Spectroscopy* after being reviewed by the co-authors. It is currently to be presented as Sublett D. M., Sendula E., Lamadrid H., Steele-MacInnis M., Spiekermann G., and Bodnar R. J. (In prep) Raman spectral behavior of N_2, CO_2, and CH_4 in N_2-CO_2-CH_4 gas mixtures from 22-200°C and 10-500 bars. *J. Raman. Spec.* ***D. M. Sublett*** was responsible for collecting the Raman spectral data and writing the manuscript. *E. Sendula, H. Lamadrid, M. Steele-MacInnis, G. Spiekermann, R. C. Burruss,* and *R. J. Bodnar* contributed to data interpretation and the preparation and editing of the manuscript.

Table of Contents

Chapter 1: Synthetic fluid inclusions XXI. Partitioning of Na and K between liquid and vapor in the H_2O-NaCl-KCl system at 600-800°C and 500-1000 bars

Abstract

The synthetic fluid inclusion technique was used to determine the partitioning behavior (distribution constant) of Na and K between coexisting liquid and vapor phases in the H_2O-NaCl-KCl system at 500-1000 bars, 600-800°C, and for fluids with initial Na/K molar ratios of 3:1, 2:1, 1:1, 1:2 and 1:3. Compositions of coexisting liquid and vapor phases in the binary H_2O-KCl system were also determined. Distribution constants for sodium ($D_{Na}^{L/V}$) and potassium ($D_{K}^{L/V}$) were calculated from salinities of the synthetic fluid inclusions determined by microthermometry. For a given temperature, pressure and molar Na/K ratio, the distribution constants for Na and K between liquid and vapor are essentially equal, with only a slight preference for Na to partition into the vapor phase and for K to partition into the liquid phase. As such, fluid phase immiscibility and the subsequent physical separation of the liquid and vapor phases owing to buoyancy differences are unlikely to lead to fluids with variable Na/K in different parts of magmatic-hydrothermal systems. The liquid-vapor partitioning behavior obtained here is consistent with previously determined Na/K partitioning between granitic melts and exsolved magmatic aqueous fluids, and with compositions of hydrothermal fluids and associated feldspars in potassic alteration zones of porphyry copper deposits.

1. Introduction

Fluid-rock interactions are ubiquitous in the Earth's crust (Yardley and Bodnar, 2014), and the composition and mineralogy of altered rocks depends on various factors, including the temperature and pressure conditions, rock chemistry, and composition of the fluid phase(s). Much of our knowledge of the physics and chemistry of fluid-rock interactions comes from studies of economic mineral deposits (c.f., Lowell and Guilbert, 1970; Beane and Titley, 1981; Beane and Bodnar, 1995; Sillitoe, 2010). In the porphyry-epithermal environment, sodium- and potassium-bearing minerals are characteristic alteration phases, and these phases show systematic distributions in time and space (Lowell and Guilbert, 1970; Hedenquist et al., 2017). Potassium feldspar ($KAlSi_3O_8$) and biotite [$K(Mg,Fe)_3AlSi_3O_{10}(OH)_2$] characterize early, deep alteration in the cores of porphyry systems, with later sericite (K-mica; [$KAl_2(AlSi_3O_{10})(OH)_2$]) associated with phyllic alteration often overprinting and occurring peripheral to the potassic core. Adularia ($KAlSi_3O_8$), illite [$K_{0.6\text{-}0.85}(Al,Mg)_2(Si,Al)_4O_{10}(OH)_2$] and alunite [$KAl_3(SO_4)_2(OH)_6$] are common alteration products in the overlying and genetically related epithermal environment. In the porphyry environment, sodium-bearing phases are less common, with albite ($NaAlSi_3O_8$) occasionally occurring in the low temperature peripheral propyllitic zone. Some porphyry systems, such as at Yerington, Nevada, show a deep sodium-calcium metasomatism in place of the more typical potassic alteration (Carten, 1986).

The common occurrence of potassium and, to a lesser extent, sodium-bearing phases associated with fluid-rock interaction is consistent with fluid inclusion studies that have established that sodium and potassium are generally the two most abundant cations in fluids associated with porphyry and epithermal deposits. This conclusion is based on early studies that identified halite and sylvite daughter minerals in fluid inclusions from these deposits (c.f., Roedder, 1971; Bodnar and Beane, 1980) and more recent laser ablation-inductively coupled plasma-mass spectrometry (LA-ICP-MS) analyses of individual fluid inclusions (summarized in Bodnar et al., 2014). Thus, developing a better understanding of the physical and chemical processes that distribute Na and K in the porphyry-epithermal environment will contribute to our understanding of fluid evolution associated with ore formation in this environment.

Phase separation or immiscibility (sometimes referred to as boiling) is common in the porphyry-epithermal environment (Henley and McNabb, 1978; Bodnar, 1995; Moncada et al., 2017). During this process, a single-phase fluid separates into a high density, high salinity brine coexisting with a low density, low salinity vapor (Bodnar et al., 1985). The various elements and chemical species contained in the fluid before phase separation are often partitioned disproportionately between the two coexisting immiscible fluid phases (Candela and Piccoli, 1995; Williams et al., 1995). For example, sulfur and some elements that form sulfide complexes (such as Cu) preferentially partition into the vapor phase while chlorine and elements that form chloride complexes (such as Ag) preferentially partition into the liquid phase (Heinrich et al., 1999). Owing to significant differences in buoyancy, the liquid and vapor phases tend to separate physically, with the vapor migrating upwards in the system and the liquid phase remaining at depth and sometimes flowing to deeper levels (Henley and McNabb, 1978). Phase separation is also an important depositional mechanism in many ore systems (Williams-Jones and Heinrich, 2005). As such, understanding how the different fluid components are distributed between the liquid and vapor phases has significant implications concerning not only the distribution of alteration assemblages but also the distribution of ore-forming components within the overall magmatic-hydrothermal system.

The system H_2O-NaCl-KCl has commonly been used to approximate the composition of magmatic-hydrothermal fluids associated with porphyry copper deposits (PCD). Phase relations in the ternary H_2O-NaCl-KCl system have been described by various authors (Sterner et al., 1988; Hall et al., 1988; Chou, 1987; Chou et al., 1992; Sterner et al., 1992; Anderko and Pitzer, 1993; etc.). However, few experimental data are available for the H_2O-NaCl-KCl system in the two-phase liquid + vapor region. Fournier and Thompson (1993) and Foustoukos and Seyfried Jr (2007) describes the composition of the vapor phase in this ternary system but do not provide information on the composition of the liquid phase in equilibrium with the vapor. Abundant experimental data are available for the binary H_2O-NaCl sub-system in the two-phase liquid + vapor field (e.g., Sourirajan and Kennedy, 1962; Bodnar et al., 1985; Bischoff and Pitzer, 1989; etc.) and relatively fewer experimental data are available for the binary H_2O-KCl system in the two-phase liquid + vapor region (e.g., Khaibullin and Borisov 1966; Shmulovich et al., 1995; Hovey et al., 1990).

In this study, experiments were performed in the two-phase liquid + vapor region of the H_2O-NaCl-KCl system at 600, 700, and 800°C, 500, 750, and 1000 bars, and molar ratios of Na/K of 1:3, 1:2, 1:1, 2:1, and 3:1 using the synthetic fluid inclusion technique (Sterner and Bodnar, 1984). Distribution constants for sodium and potassium between the coexisting liquid and vapor phases were calculated from compositions of liquid and vapor extracted from microthermometric data. We note that here we adopt the IUPAC (2014) recommended usage that defines the distribution constant as the concentration of a component in one phase divided by its concentration in a second immiscible phase. Moreover, the IUPAC (2014; page 1067) reports that the term “partition coefficient” is obsolete and should not be used. Experiments were also performed in the two-phase liquid + vapor region of the H_2O-KCl system at 500, 600, 700, and 800°C and 300, 500, 750, and 1000 bars and the data were used to determine compositions of coexisting liquid and vapor in this binary system. Data for the H_2O-KCl system were combined with phase equilibrium data for H_2O-NaCl from the literature to develop a more holistic interpretation of the partitioning behavior of sodium and potassium across the complete compositional spectrum in the H_2O-NaCl-KCl ternary system.

2. Methods

2.1 Formation of Synthetic Fluid Inclusions

Synthetic fluid inclusions were prepared following the methods of Sterner and Bodnar (1984) and are summarized below. Fluid inclusions (FI) were synthesized in thermally fractured, inclusion free, ~4 mm diameter Brazilian quartz cores by sealing the core in a 5 mm OD, 20 mm long platinum capsule along with ~60 µL of a solution of known composition. The composition of the starting solution was 10 wt% total salinity with Na/K molar ratios of 3:1, 2:1, 1:1, 1:2, 1:3, or 0:1 (for experiments in the H_2O-KCl system). The capsules were then weighed, heated to ~120°C for 1-2 hours, and then checked for weight loss to ensure that the capsules were properly sealed. The capsules were then loaded into a cold-seal pressure vessel and placed in a furnace and taken to the experimental conditions. Phase relationships of the binary H_2O-NaCl system determined by Bodnar et al. (1985) and Sourirajan and Kennedy (1962) were used to approximate the heating path in order to avoid entering the two-phase region before the experimental PT conditions were reached (see Bodnar et al., 1985, their Fig. 13). Once the experimental temperature was reached and the temperature was stabilized, phase separation was induced by rapidly lowering the pressure to the experimental pressure within the two-phase region. At the experimental PT conditions, the fractures healed and subsequently trapped one (or both) of the two immiscible fluid phases to produce synthetic FI. Run durations varied from four days for the higher PT runs (e.g., 1000 bars/800°C) to 14 days for the lower *PT* runs (e.g., 500 bars/600°C). At the conclusion of the run, the cold-seal pressure vessels were removed from the furnaces and the samples were cooled in air. After the cold seal vessels reached room temperature, the capsules were removed from the bombs, cleaned, and weighed to ensure that the capsule did not leak during the experiment. Samples showing a measureable difference in weight that was greater than the precision of the balance used (~±0.000x grams – approximately 0.06 grams of solution was originally loaded into the capsules) were discarded. The cores were then removed from the capsules and cut into ~1 mm thick disks that were doubly polished in preparation for petrographic and microthermometric analysis.

2.2 Petrographic and Microthermometric Methods

Phase separation (immiscibility) at experimental trapping conditions was evidenced by the presence of two different types of FI coexisting in the same healed fracture, one that trapped the liquid phase at the *PT* conditions (Fig. 1a) and one that trapped the vapor phase (Fig. 1b). Evidence of immiscibility was found for all experimental *PT* combinations except for FI trapped at 1000 bars/600°C for all Na/K molar ratios, and those trapped at 750 bars/600°C for Na/K molar ratios of 1:2, 1:3 and 0:1. At these *PTX* conditions, the fluid did not undergo immiscibility and remained a single-phase fluid for the duration of the run, as evidenced by FI of only one type in the sample. Moreover, FI trapped in the one-phase field all had a salinity and Na/K ratio equal to that of the solution originally loaded into the capsule.

FI that trapped the high salinity liquid phase in the two-phase field in the H_2O-NaCl-KCl system became saturated with respect to NaCl and KCl during cooling from formation conditions, and halite and sylvite daughter minerals precipitated in the FI (Fig. 1a, c). Some liquid-rich FI formed at higher pressures remained metastable (described below) during cooling from formation conditions to room temperature. FI that trapped the liquid phase in the H_2O-KCl system became saturated in KCl and a sylvite daughter mineral precipitated during cooling (Fig. 2a). During cooling of FI that trapped the vapor phase a liquid condensed from the trapped vapor to produce a vapor-rich FI at room temperature (Figs. 1b, 2b).

For liquid-rich FI trapped at higher pressures, the FI contained only liquid and vapor at room temperature, even though the salinity of the liquid phase was such that halite and/or sylvite should have precipitated during cooling from formation conditions. Such metastability was observed in all FI trapped at 1000 bars and in some FI trapped at 750 bars. The reason that these

FI failed to nucleate halite and/or sylvite during cooling from formation conditions is that the liquid salinity is only slightly in excess of that required to reach saturation in these phases because the *PT* trapping conditions were close to the top of the solvus (in *PX* space) where the liquid salinity decreases rapidly with increasing pressure as the critical point is approached, as discussed in more detail below. To facilitate nucleation of daughter minerals in the metastable FI, the samples were cooled to liquid nitrogen temperatures (~-190°C) and re-heated to room temperature using a Linkam THMSG 600°C programmable heating/cooling stage mounted on a petrographic microscope. In most cases, daughter minerals precipitated as a result of cooling and reheating to room temperature, and the dissolution temperatures of the daughter minerals could then be measured to determine the composition of the FI, as described below. An FI showing this type of metastable behavior is shown in Fig. 3 where, after cooling from formation conditions to 25°C the FI contains only liquid and vapor. Following cooling to ~-190°C and subsequent re-heating, numerous solids are present in the FI (-5.3°C). Further heating to 25°C results in an FI containing numerous small halite and sylvite crystals. With time, the smaller crystals dissolve as the larger crystals grow (Ostwald ripening), finally resulting in an FI containing only a single halite and a single sylvite crystal (in addition to liquid and vapor). This ripening process may be accelerated by cycling the temperature by gradually heating the FI by several tens of degrees followed by cooling to room temperature and repeating this process several times.

In one sample formed at 700°C, 1000 bars from a fluid with an initial Na/K ratio of 1:3, only a sylvite daughter mineral precipitated during initial cooling from formation conditions, and thus the ice melting temperature was used in conjunction with the sylvite dissolution temperature to determine the composition of the liquid-rich FI in that sample. For FI that contained both sylvite and halite daughter minerals, the composition was determined based on the dissolution temperatures of the halite and sylvite daughter minerals and the phase relationships for the H_2O-NaCl-KCl ternary system described by Sterner et al. (1988). The methodology is shown in Fig. 4 and described here. On Fig. 4, the composition of a liquid that is in equilibrium with both sylvite and halite, and thus lies on the halite-sylvite cotectic, is shown by point A. We note that along the halite-sylvite coexistence curve from the peritectic point to a temperature of ~140°C, the system displays peritectic behavior as evidenced by the fact that NaCl exhibits retrograde solubility in the presence of sylvite over this temperature range. As the temperature increases, the composition of the liquid in equilibrium with both sylvite and halite moves along the halite-sylvite cotectic as the daughter minerals dissolve into the liquid until one of the phases (in this case sylvite) dissolves completely (point C on Fig. 4). With continued heating the composition of the liquid in equilibrium with halite follows a line extending from the halite-sylvite cotectic towards the NaCl apex as the halite daughter mineral continues to dissolve and becomes smaller (i.e., point D on Fig. 4). With continued heating the halite dissolves completely (point E on Fig. 4). Point E thus represents the composition of the liquid that was trapped in the FI. All vapor-rich FI nucleated a sylvite daughter mineral and ice upon cooling from room temperature to ~-190°C. We note that during cooling from trapping conditions to room temperature, a small amount of liquid condenses from the originally trapped vapor to produce an inclusion that at room temperature contains a small volume proportion of liquid with a density of ~1g/cm^3 and a larger volume proportion of a vapor with a density of ~0.0000x g/cm^3. At room temperature and below essentially all of the mass in vapor-rich FI is therefore contained within the liquid phase. As such, we determine the composition of the liquid phase in the vapor-rich inclusions, and this represents the composition of the vapor phase that was trapped at experimental conditions. The composition of the vapor-rich FI was determined by measuring the dissolution temperatures of the sylvite daughter mineral and ice and interpreting these data using the phase relationships given by Hall et al. (1988) for the ice stable field of the H_2O-NaCl-KCl ternary (Fig. 5). Following cooling to ~-190°C the FI is heated and at the eutectic temperature (-22.9°C for H_2O-NaCl-KCl) a liquid forms and is in equilibrium with three solid phases (ice, hydrohalite, and sylvite; point A on Fig. 5). With further heating above -22.9°C, one of the solid phases dissolves completely (hydrohalite in all samples in this study) and the composition of the liquid in the FI moves along the cotectic of the remaining two solid phases (sylvite and ice) until one of the solid phases completely dissolves (in this case sylvite; point C on Fig. 5). For vapor-rich FI in this study, sylvite is always the solid phase that disappears along the ice-sylvite cotectic during heating. With continued heating the composition of the liquid in the FI moves away from the cotectic and towards the H_2O apex until the ice dissolves completely (point D on Fig. 5). The composition of the vapor that was in equilibrium with the liquid phase at the experimental *PT* conditions is defined by the point on the ternary where the line extending from the sylvite-ice cotectic to the H_2O apex intersects with the isotherm corresponding to the final ice melting temperature (point D; Fig. 5).

In many cases, FI that trapped the vapor phase also trap some liquid along with the vapor because the liquid phase is the phase that "wets" the mineral surface. Thus, the vapor-rich FI rarely trap only a single fluid phase. The mixed trapping results in a FI composition that is different from the true composition of the vapor that was in equilibrium with the liquid at the experimental *PT* conditions. Thus, the measured salinity of the FI that trapped the vapor phase (along with variable amounts of the liquid phase) is always higher than the true salinity of the vapor phase owing to the much higher salinity of the liquid phase that was trapped along with the vapor. The measured salinity of the resultant FI varies in proportion to the relative amounts of liquid and vapor that were trapped in the vapor-rich FI. Trapping of liquid along with the vapor phase at the experimental *PT* conditions is manifest by variable ice melting temperatures within a group of vapor-rich FI within the same healed fracture. FI that trapped significant amounts of liquid along with the vapor are often recognizable based on room temperature phase relationships that are intermediate between FI that trapped only liquid and those that trapped mostly vapor and only small amounts of liquid (Fig. 1c).

In a binary H_2O-salt system, such as H_2O-NaCl, trapping variable amounts of liquid along with the vapor results in a range in final ice melting temperatures, as shown by Bodnar et al. (1985; their Fig. 9). In this case, the salinity that provides the best approximation of the true salinity of the vapor phase is that which corresponds to the highest ice melting temperature (lowest salinity), as described by Bodnar et al. (1985). However, in a three component system such as H_2O-NaCl-KCl, the composition of the trapped vapor phase is determined from the final ice melting temperature and the dissolution temperature of the second-to-last solid phase. If the cation ratio (Na/K in this case) of the liquid and vapor phases are significantly different, mixing results in variations in the dissolution temperature of the second-to-last solid phase as well as the final melting temperature of the ice. That is, owing to the different cation ratios in the liquid and vapor phases, the point at which the second-to-last solid disappears and the liquid composition leaves the cotectic and moves towards the H_2O apex varies in proportion to the relative amounts of liquid and vapor that were trapped. This, in turn, affects the trajectory that the liquid path follows through the ice stable field as ice melts and affects the point at which the path intersects the isotherm corresponding to final ice melting. Additionally, because trapping liquid along with vapor modifies the total salinity, the isotherm corresponding to final ice melting varies in response to variations in the proportions of liquid and vapor that were trapped. Because both temperatures (second-to-last phase disappearance and ice melting temperature) are necessary to determine the composition (salinity and Na/K ratio) of the vapor-rich FI, approximating the true composition of the vapor phase in the ternary system is not as straightforward as with a binary H_2O-salt system.

The method used in this study to approximate the composition of the vapor phase when both the dissolution temperature of the second-to-last and the last solid phases are highly variable is illustrated in Fig. 6. In the ternary system H_2O-NaCl-KCl, the compositions of the liquid and vapor phases that are in equilibrium at formation conditions represent the end points of a tie line that must pass through the bulk composition. In the present study, the bulk composition is known, and the composition of the liquid phase is known reasonably well and shows little variability because FI that trap the liquid usually do not trap any vapor along with the liquid. Moreover, the composition of the liquid phase is easily determined from the measured halite and sylvite dissolution temperatures as described above. Assuming that vapor-rich FI trapped some unknown amount of higher salinity liquid along with the vapor, those vapor-rich FI that show the highest ice melting temperature (corresponding to the lowest salinity) represent the FI that trapped the smallest proportion of liquid and, therefore, most closely approximate the true vapor composition. Thus, the intersection of the tie line extrapolated from the composition of the liquid phase through the bulk composition to its intersection with the isotherm corresponding to the highest ice melting temperature provides the best approximation of the composition of the vapor phase in equilibrium with liquid at the trapping conditions.

The NaCl/KCl ratios of the coexisting liquid and vapor phases are determined by connecting tie-lines from the H_2O apex through the composition of the liquid and vapor phases and intersecting with the NaCl-KCl binary (dashed black lines in Fig. 6). This method is most useful when NaCl/KCl ratios in the liquid and vapor phases are significantly different, such as the example shown in Fig. 6 where the resulting NaCl/KCl ratio of the vapor is ~1:3 while the resulting NaCl/KCl ratio for the liquid is ~2:1. If these two fluids were to mix, the resulting dissolution temperatures measured for the second-to-last solid phase (sylvite) in the vapor-rich FI would likely vary by up to several degrees depending on the proportion of liquid trapped along with the vapor. This method is also useful when the sylvite daughter phase does not nucleate during cooling. In some vapor-rich FI in the H_2O-NaCl-KCl system in the present study, the FI did not nucleate a sylvite daughter mineral during cooling. These vapor-rich FI that failed to nucleate a sylvite daughter mineral during cooling tended to be smaller (~5 μm or less) with a melting temperature of ice greater than ~-2°C (i.e., low salinity), and were more commonly observed when the initial Na/K molar ratios were 3:1 and 2:1.

3. Results

3.1 Equilibrium Fluid Compositional Data

The Na/K ratios of the liquid and the vapor are nearly identical at all trapping conditions. Thus, trapping of small amounts of liquid along with the vapor has an insignificant effect on the Na/K ratio of the vapor-rich FI and on the dissolution temperature of sylvite in vapor-rich FI. Fig. 7 shows the dissolution temperature (T_m) of sylvite vs. T_m of ice for every vapor-rich FI in which both temperatures were measured in this study. The FI with the highest T_m of ice (lowest salinity) was assumed to most closely approximate the true composition of the vapor phase, and as such the highest T_m of ice measured for each pressure, temperature, and composition (*PTX*) condition was used to approximate the composition of the vapor phase in equilibrium with liquid at that condition. Compositions of FI were calculated from the microthermometric data using the FORTRAN program SALTY developed by Bodnar et al. (1989). The equilibrium compositions of the liquid and vapor phases at various *PT* conditions in the H_2O-NaCl-KCl system are listed in Table 1.

Salinities of FI that trapped the liquid in the H_2O-KCl system were determined by measuring the dissolution temperature of the sylvite daughter mineral and referring this value to the known solubility of KCl as a function of temperature. Compositions of FI that trapped the vapor in the H_2O-KCl system were determined by measuring the melting temperature of ice and referring this value to the known relationship between salinity and freezing point depression of ice in the system H_2O-KCl (Hall et al., 1988). As with the ternary fluid compositions, salinities of both the liquid-rich and vapor-rich FI in the H_2O-KCl system were calculated using the program SALTY (Bodnar et al. 1989). As with vapor-rich FI in the ternary system, the FI with the highest T_m of ice (lowest salinity) was used to estimate the salinity of the vapor phase in equilibrium with liquid. The equilibrium compositions of the liquid and vapor phases at various *PT* conditions for the H_2O-KCl system are given in Table 2.

We note that a vapor bubble was present in all liquid-rich inclusions at the temperature of disappearance of the final solid (halite or sylvite). Steele-MacInnis and Bodnar (2013) examined the effect of the vapor bubble on the calculated composition of the liquid phase in H_2O-NaCl synthetic FI. They found that the errors in salinity associated with ignoring the vapor bubble are generally small. The magnitude of the error increases as the difference between the solid dissolution temperature and the liquid-vapor homogenization temperature increases, with an error of less than ~1.5 wt% NaCl when the difference is on the order of several hundred degrees Celsius. In most samples in this study, the measured salinities of the liquid phase are in excess of 60 wt%, and a difference of 1.5 wt% is not considered to be significant, especially considering that the range in measured salinities for some samples is larger than 1.5 wt% (see Tables 1 and 2). As such, the salinities of the liquid phase presented in Tables 1 and 2 ignore the effect of the vapor bubble.

3.2 Determination of Liquid-Vapor Distribution Constants for Sodium and Potassium

The distribution constant for sodium between the coexisting liquid and vapor phases, $D_{Na}^{L/V}$, at any given *PT* is expressed as the ratio of the molal concentration of sodium in the liquid phase, c_{Na}^{L}, to the molal concentration of sodium in the vapor phase, c_{Na}^{V}:

$$D_{Na}^{L/V} = \frac{c_{Na}^{L}}{c_{Na}^{V}} \quad [1]$$

Similarly, the distribution constant for potassium, $D_{K}^{L/V}$, at any given PT is expressed as the ratio of the molal concentration of potassium in the liquid phase, c_{K}^{L}, to the molal concentration of potassium in the vapor phase, c_{K}^{V}:

$$D_{K}^{L/V} = \frac{c_{K}^{L}}{c_{K}^{V}} \quad [2]$$

As mentioned above, the highest ice melting temperature (lowest salinity) obtained from vapor-rich FI in a given sample, and the average composition of liquid-rich FI in a given sample were used to calculate the distribution constants. The distribution constants for sodium and potassium in the H_2O-NaCl-KCl system calculated from equations 1 and 2, respectively, are listed in Table 3. Additionally, the distribution constants for chlorine were calculated using the same approach as for sodium and potassium, and are listed in Table 3.

The distribution constants for sodium and potassium were fitted using the following relationship

$$Log\left(D_{i}^{L/V}\right) = \frac{A}{T} + (B \cdot P) + C \quad [3]$$

where *P* is the pressure in bars, *T* is temperature in Celsius, $D_{i}^{L/V}$ is the distribution constant for either Na or K, and *A*, *B*, and *C* are fitting parameters listed in Table 4. The form of the relationship between the distribution constant and temperature and pressure in equation 3 was chosen because it follows a linearized Van't Hoff function, *log(D)* vs. 1/*T*. The exchange of sodium and potassium between the coexisting liquid and vapor phases is essentially an equilibrium reaction where the distribution constant is the equilibrium constant and, as such the mathematical relationship is reasonable. The pressure dependence term was added to account for the fact that as pressure increases, the compositions of liquid and vapor approach each other and become equal at the critical point.

Over the *PTX* range studied, the Na/K ratio in the liquid phase is essentially equal to that in the coexisting vapor phase. This result is consistent with the observation that T_m of sylvite in vapor-rich FI did not vary significantly, even though T_m of ice (representing the total salinity) showed considerable variation (Fig. 7). This indicates that any liquid that may have been trapped along with the vapor had a negligible effect on the Na/K ratio of the vapor-rich FI. Therefore, the Na/K ratio of the liquid must be similar to the Na/K ratio of the vapor that is in equilibrium with the liquid at the trapping conditions. The distribution constant for sodium is plotted versus the distribution constant for potassium in Fig. 8, with a linear fit of the data (in black) lying slightly above the 1:1 line that indicates equal partitioning between the liquid and vapor phases. The nearly 1:1 correlation of the distribution constants indicates that sodium and potassium are partitioned in nearly equal proportions between liquid and vapor. There is only a slight preference for potassium to go into the liquid phase and for sodium to prefer the vapor phase. The Na/K ratio of the liquid phase in equilibrium with vapor is plotted versus the Na/K ratio of the initial solution (before phase separation) in Fig. 9. The majority of the data fall within the area bounded by the grey dashed lines, which represent a ±10% variation from the 1:1 line that corresponds to identical Na/K ratios in both the starting solution and in the liquid phase after phase separation. The Na/K ratio of the immiscible liquid phase is essentially equivalent to the Na/K ratio of the starting bulk solution that was sealed inside the capsule at the beginning of the experiments, as evidenced by the data plotted on Fig. 9, which is only possible because Na and K partition in equal proportions between the liquid and vapor phases.

4. Discussion

The experimental results obtained here are in good agreement with data reported by Lagache and Weisbrod (1977) on partitioning of sodium and potassium in the system albite-orthoclase-

H_2O-NaCl-KCl. Starting with a fluid with an initial Na/K ratio of 3:1, these workers observed that the initial single-phase fluid separated into coexisting liquid and vapor phases in the range 300-660°C and 0.2-2 kbars. The equilibrium constant, which they defined as $C = \frac{m_{KCl}}{m_{NaCl}}$ indicated that KCl is preferentially partitioned into the liquid phase and NaCl is preferentially partitioned into the vapor phase. The slight preference of potassium for the liquid phase relative to sodium is also in good agreement with data of Shinohara et al. (1989) who studied the partitioning behavior of sodium and potassium between the coexisting liquid and vapor phases at 1.2 kbars, and found that the K/Na ratio in the liquid was slightly elevated compared to the vapor phase, indicating a slight preference for potassium to partition into the liquid phase. The equation of state for H_2O-NaCl-KCl developed by Anderko and Pitzer (1993) also predicts slightly higher X_{NaCl}/X_{KCl} ratios in the vapor relative to the coexisting liquid, indicating that sodium preferentially partitions into the vapor relative to potassium during phase separation.

Salinities of the coexisting liquid and vapor phases for the ternary H_2O-NaCl-KCl system and the binary H_2O-KCl system from the present study are plotted on ternary diagrams along with data for the H_2O-NaCl system from by Bodnar et al. (1985) in Fig. 10. The results show that the two-phase liquid + vapor region expands with increasing temperature and decreasing pressure. At all *PT* conditions except 750 bars and 600°C, the total salinity of the liquid phase in equilibrium with vapor initially increases when KCl is added to the H_2O-NaCl system or when NaCl is added to the H_2O-KCl system, i.e., as the composition moves away from the two binaries and into the ternary. This suggests that, at a given temperature and pressure, the immiscibility gap is wider in the ternary system compared to the binary systems. According to the results of this study, the miscibility gap is widest for a liquid in equilibrium with a vapor with an Na/K ratio between 1:1 to 3:1, and it narrows as the vapor composition becomes either more potassium or more sodium rich. Our results also show that fluids with a total salinity of 10 wt% and Na/K ratios of 1:2, 1:3, and 0:1 are in the single-phase fluid field at 600°C and 750 bars, indicating that at 600°C the maximum pressure on the solvus moves to lower values as the bulk composition becomes more potassium rich. Over most of the *PT* range studied, the two-phase region extends to higher salinities for more sodium-rich compositions, compared to potassium-rich compositions, especially at 600°C and 500 and 750 bars, and at 800°C and 750 and 1000 bars (Fig. 10). Based on the trend shown in Fig. 10 for 1000 bars and 700°C and 800°C, it is reasonable to assume that the top of the solvus at 700°C and 800°C also moves to lower pressures at a given temperature as the fluid becomes more potassium rich. It is worth noting that results from the present study show some disagreement with data from Shmulovich et al. (1995). Their results indicate that an H_2O-KCl fluid with a total salinity of 10 wt% is in the two-phase liquid + vapor field at 600°C and 750 bars, whereas our results indicate a single-phase fluid at these conditions.

Because sodium and potassium are partitioned in essentially equal proportions between coexisting liquid and vapor phases during phase separation, the measured Na/K ratio in either the liquid phase or the vapor phase can be used to determine the Na/K ratio in the initial single-phase fluid before phase separation occurred, assuming that the fluid composition is reasonably well approximated by the H_2O-NaCl-KCl system. The sodium and potassium concentrations obtained from natural brine (liquid) FI from porphyry copper deposits (PCD), normalized to the three-component H_2O-NaCl-KCl system, are plotted on Fig. 11. The majority of the data fall within the Na/K molar ratio range of 0.64-3.8. The natural fluid inclusions are thought to represent magmatic fluids that have exsolved from a crystallizing, sub-volcanic intermediate composition magma. Compositions of fluid inclusions that trapped the magmatic fluid may be used to infer the Na/K ratio of the melt from which they exsolved. The experimentally determined distribution constant for sodium and potassium between melt and aqueous fluid $\left(D_{Na/K}^{m/aq}\right)$ in granitic systems ranges from ~0.74 (Shinohara et al., 1989, Kravchuk et al., 1993, Carron and Lagache, 1980, etc.) to ~0.40 (Student and Bodnar, 1999, Webster, 1992, Kilinc and Burnham, 1972, etc.). Because Na and K are partitioned in essentially equal proportions between liquid and vapor phases at magmatic conditions, the Na/K ratio observed in either of the coexisting immiscible fluid phases can be assumed to represent the Na/K ratio in the bulk fluid that exsolved from the magma. The range in Na/K observed in natural liquid-rich FI in PCD (~0.64-3.8) (Fig. 11), combined with experimentally determined partition coefficients for sodium and potassium between the melt and magmatic fluid (~0.74-0.4), indicates an Na/K molar ratio of the original melt (before exsolution of a magmatic-fluid phase) is between ~0.26 and 2.8 for the magmatic-hydrothermal systems shown in Fig. 11. The Na/K ratio of granitic melts from various localities inferred from melt inclusion studies are also plotted on Fig. 11. Of the 300 data points representing MI from 15 different studies of silicic (granitic) rocks, ~96 % of the calculated Na/K ratios are within the range predicted from compositions of natural liquid-rich FI from similar magmatic-hydrothermal environments. Some studies (see Zajacz et al., 2009 and references therein) have shown that Na can diffuse from natural fluid and melt inclusions hosted in quartz. The potential for loss of Na and other post-entrapment modifications should be taken into consideration when applying the above method to determine the Na/K ratio of a melt using natural fluid inclusions.

We can use the feldspar-fluid partitioning behavior determined by Orville (1963) to predict the composition of a fluid that would be in equilibrium with alkali feldspar in magmatic-hydrothermal systems. While few data are available on compositions of feldspars from the potassic alteration zone in porphyry copper deposits, the fluid that would be in equilibrium with K-feldspar from a PCD in Macedonia (Serafimovski et al., 2008) falls within the range shown on Fig. 11.

Experimental data from this study allow us to infer the *PTX* phase behavior in the system H_2O-NaCl-KCl, as shown on Fig. 12. In this ternary system, as in most aqueous electrolyte systems, the compositions of the liquid and vapor phase approach each other in the vicinity of the critical point. Stated differently, the vapor phase can become quite saline and enriched in chloride ions near the critical point. This, in turn, has important implications for ore formation in magmatic-hydrothermal deposits where numerous studies have suggested that the vapor phase plays a key role in the transport of metals. Thus, as shown on Fig. 12, metal transport in the vapor phase as chloride species would be enhanced at pressures that are just below the top of the solvus for a given temperature. Moreover, because the vapor phase is more buoyant it will physically separate from the liquid phase and migrate into the upper reaches of the magmatic-hydrothermal system, thus providing an effective means to transport metals from the deeper porphyry environment into the shallower epithermal environment.

5. Conclusions

Because Na and K are partitioned in equal proportions between coexisting liquid and vapor phases over the range of *PT* conditions examined, data from fluid inclusions in magmatic-hydrothermal systems can be used to infer compositions of the initial magmatic fluid that exsolved from magmas as well as the Na/K ratio of the igneous melt. The examples presented above document the internal consistency and good agreement between Na/K partitioning between liquid and vapor determined in this study, and previously determined Na/K partitioning behavior between granitic melts and exsolved magmatic aqueous fluids, and between feldspars associated with potassic alteration and magmatic/hydrothermal fluids. The method described here offers the potential to examine mineral-melt-fluid(s) partitioning behavior in more complex systems, and over a wider range of *PTX* conditions.

Acknowledgements

The authors thank Héctor Lamadrid and Charles Farley for assistance and instruction in the laboratory. We would also like to thank Matt Steele-MacInnis for many useful discussions on the topic. Review comments and suggestions by Yuan Li and two anonymous reviewers helped to significantly improve the data interpretations and presentation. This material is based in part on work supported by the National Science Foundation under grant numbers 1019770 and 1624589 to RJB.

References

Anderko A. and Pitzer K. S. (1993) Phase equilibria and volumetric properties of the system $KCl-H_2O$ and $NaCl-KCl-H_2O$ above 573K: Equation of state representation. *Geochim. Cosmochim. Acta* **57**, 4885-4897.

Anderson Jr A.T., Newman S., Williams S.N., Druitt T.H., Skirius C., and Stloper E. (1989) H_2O, CO_2, Cl, and gas in Plinian and ash-flow Bishop rhyolite. *Geology* **17,** 221-225.

Audetat A., Pettke T., Heinrich C., and Bodnar R.J. (2008) Special paper: The composition of magmatic-hydrothermal fluids in barren and mineralized intrusions. *Econ. Geol.* **103,** 877-908.

Azbej T. (2006) The role of fluids in geological processes. Ph. D. thesis, Virginia Tech.

Bacon C.R., Newman S., and Stolper E. (1992) Water, CO_2, Cl, and F in melt inclusions in phenocrysts from three Holocene explosive eruptions, Crater Lake, Oregon. *Amer. Mineral.* **77,** 1021-1030.

Badanina E.V., Veksler I.V., Thomas R., Syritso L.F., and Trumbull R.B. (2004) Magmatic evolution of Li-F, rare-metal granites: A case study of melt inclusions in the Khangilay complex, Eastern Transbaikalia (Russia). *Chem. Geol.* **210,** 113-133.

Beane R. E. and Bodnar R. J. (1995) Hydrothermal fluids and hydrothermal alteration in porphyry copper deposits. In *Porphyry Copper Deposits of the American Cordillera* (eds. F.W. Pierce and J. G. Bohm) Arizona Geological Society Digest 20, Tucson, AZ. pp.83-93

Beane R. E. and Titley S.R. (1981) Porphyry copper deposits: Part II. Hydrothermal alteration and mineralization. *Soc. Econ. Geol.* **75**, 235-269.

Bischoff J.L. and Pitzer K.S. (1989) Liquid-vapor relations for the system $NaCl-H_2O$: Summary of the P-T-X surface from 300°C To 500°C. *Amer. J. Sci.* **289,** 217-248.

Bodnar R. J. (1995) Fluid-inclusion evidence for a magmatic source for metals in porphyry copper deposits. In *Magmas, Fluids and Ore Deposits* (ed. J. F. H. Thompson) Mineralogical Association of Canada Short Course Series. **23,** 139-152.

Bodnar R. J. and Beane R. E. (1980) Temporal and spatial variations in hydrothermal fluid characteristics during vein filling in preore cover overlying deeply buried porphyry copper-type mineralization at Red Mountain, Arizona. *Econ. Geol.* **75,** 876-893.

Bodnar R. J., Burnham C. W. and Sterner S. M. (1985) Synthetic fluid inclusions in natural quartz. III. Determination of phase equilibrium properties in the system H_2O-NaCl to 1000°C and 1500 bars. *Geochim. Cosmochim. Acta* **49,** 1861-1873.

Bodnar R. J., Lecumberri-Sanchez P., Moncada D., and Steele-MacInnis M. (2014) Fluid inclusions in hydrothermal ore deposits. In *Treatise on Geochemistry*, second edition (ed. H. D. Holland and K. K. Turekian). Elsevier, Oxford, **13**, 119-142.

Bodnar R. J., Sterner S. M., and Hall D. L. (1989) SALTY; a Fortran program to calculate compositions of fluid inclusions in the system NaCl-KCl-H_2O. *Comp. & Geos.* **15**, 19-41.

Candela P.A., and Piccoli P.M. (1995) Model ore-partitioning from melts into vapor and vapor/brine mixtures. In *Magmas, Fluids and Ore Deposits* (ed. J. F. H. Thompson) Mineralogical Association of Canada Short Course Series. **23,** 101-128.

Carron J-P. and Lagache M. (1980) Étude expérimentale du fractionnement des éléments Rb, Cs, Sr, et Ba entre feldspaths alcalins, solution hydrothermales et liquids silicates dans le systéme Q·Ab·Or·H_2O a 2 kbar entre 700 et 800°C. *Bull. Mineral.* **103,** 571-578. [in French]

Carten R. B. (1986) Sodium-calcium metasomatism; chemical, temporal, and spatial relationships at the Yerington, Nevada, porphyry copper system. *Econ. Geol.* **81**(6), 1495-1519.

Chou I-M. (1987) Phase relations in the system NaCl-KCl-H_2O. III: Solubilities of halite in vapor-saturated liquids above 450°C and redetermination of phase equilibrium properties in the system NaCl-H_2O to 1000 °C and 1500 bars. *Geochim. Cosmochim. Acta* **51**, 1965-1975.

Chou I-M., Sterner S. M., and Pitzer K.S. (1992) Phase relations in the system NaCl-KCl-H_2O: IV: Differential thermal analysis of the sylvite liquidus in the KCl-H_2O binary, the liquidus in the NaCl-KCl-H_2O ternary, and the solidus in the NaCl-KCl binary to 2 kb pressure, and a summary of experimental data for thermodynamic-PTX analysis of solid-liquid equilibria at elevated P-T conditions. *Geochim. Cosmochim. Acta* **56**, 2281-2293.

Davidson P., Kamenetsky V., Cooke D., Frikken P., Hollings P., Ryan C., Van Achterbergh E., Mernagh T., Skarmeta J., Serrano L., and Vargas R. (2005) Magmatic precursors of hydrothermal fluids at the Rio Blanco Cu-Mo deposit, Chile: Links to silicate magmas and metal transport. *Econ. Geol.* **100,** 963-975.

Dunbar N.W. and Hervig R.L. (1992) Volatile and trace element composition of melt inclusions from the lower Bandelier Tuff: Implications for magma chamber processes and eruptive style. *J. Geophys. Res.* **97,** 15151-15170.

Förster H.J., Tischendorf G., Trumbull R.B., and Gottesmann B. (1999) Late-collisional granites in the Variscan Erzebirge, Germany. *J. Petrol.* **40,** 1613-1645.

Fournier R. O. and Thompson J. M. (1993) Composition of steam in the system NaCl-KCl-H_2O-quartz at 600°C. *Geochim. Cosmochim. Acta* **57**, 4365-4375.

Foustoukos D. I. and Seyfried Jr W. E. (2007) Quartz solubility in the two-phase and critical region of the NaCl-KCl-H_2O system: Implications for submarine hydrothermal vent systems at 9°50'N East Pacific Rise. *Geochim. Cosmochim. Acta* **71**, 186-201.

Haapala I. and Thomas R. (2000) Melt inclusions in quartz and topaz of the topaz granite from Eurajoki, Finland. *J. Czech Geol. Soc.* **45,** 149.

Hall D. L., Sterner S. M., and Bodnar R. J. (1988) Freezing point depression of NaCl-KCl-H_2O solutions. *Econ. Geol.* **83**, 197-202.

Hansteen T.H. and Lustenhouwer W.J. (1990) Silicate melt inclusions from a mildly peralkaline granite in the Oslo paleorift, Norway. *Mineral. Mag.* **54,** 195-205.

Hedenquist J. W., Arribas A. R., and Aoki M. (2017) Zonation of sulfate and sulfide minerals and isotopic composition in the Far Southeast porphyry and Lepanto epithermal Cu-Au deposits, Philippines. *Resource Geology* **67**(2), 174-196.

Heinrich C. A., Günther D., Audétat, A., Ulrich, T., and Frischknecht R. (1999) Metal fractionation between magmatic brine and vapor, determined by microanalysis of fluid inclusions. *Geology* **27**(8), 755-758.

Henley R.W. and McNabb A. (1978) Magmatic vapor plumes and ground-water interaction in porphyry copper emplacement. *Econ. Geol.* **73,** 1-20.

Hildreth W. (1981) Gradients in silicic magma chambers: Implications for lithospheric magmatism. *J. Geophys. Res.* 86, 10153-10192.

Hovey J. K., Pitzer K. S., Tanger IV J. C., Bischoff J. L., and Rosenbauer R. J. (1990) Vapor-liquid phase equilibria of potassium chloride-water mixtures: Equation-of-state representation for KCl-H_2O and NaCl-H_2O. *J. Phys. Chem* 94, 1175-1179.

IUPAC (2014) International Association of Pure and Applied Chemistry, Compendium of Chemical Terminology, Gold Book, Version 2.3.3, 2014-02-24, edited by A. D. McNaught and A. Wilkinson.

Khaibullin I. K. and Borisov N. M. (1966) Experimental investigation of the thermal properties of aqueous and vapor solutions of sodium and potassium chlorides at phase equilibrium. *High Temp.* **4**, 489- 494.

Kilinc I.A. and Burnham C.W. (1972) Partitioning of chloride between a silicate melt and coexisting aqueous phase from 2 to 8 kilobars. *Econ. Geol.* **67,** 231-235.

Klemm L. M., Pettke T., Heinrich C. A., and Campos E. (2007) Hydrothermal evolution of the El Teniente Deposit, Chile: Porphyry Cu-Mo ore deposition from low-salinity magmatic fluids. *Econ. Geol.* **102**(6), 1021-1045.

Knight C.L. and Bodnar R. J. (1989) Synthetic fluid inclusions: IX. Critical PVTX properties of NaCl-H_2O solutions. *Geochim. Cosmochim. Acta* **53,** 3-8.

Kravchuk I.F., Malinin S.D., Senin V.G., and Bannykh L.N. (1993) K and Na fractionation in a system formed by an aluminosilicate melt and an aqueous chloride fluid. *Geochem. Int.* **30,** 1172-1185.

Lagache M., and Weisbrod A. (1977) The system: Two alkali feldspars-KCl-NaCl-H_2O at moderate temperatures and low pressures. *Contrib. Mineral. Petrol.* **62**, 77-101.

Lerchbaumer L. and Audetat A. (2012) High Cu concentrations in vapor-type fluid inclusions: An artifact? *Geochim. Cosmochim. Acta* **88,** 255-274.

Lowell J. D. and Guilbert J. M. (1970) Lateral and vertical alteration-mineralization zoning in porphyry ore deposits. *Econ. Geol. Bull. Soc.* **65**(4), 373-408.

Lu F., Anderson A.T., and Davis A.M. (1992) Melt inclusions and crystal- liquid separation in rhyolitic magma of the Bishop Tuff. *Contrib. Mineral. Petrol.* **110,** 113-120.

Moncada D., Baker D., and Bodnar R.J. (2017) Mineralogical, petrographic and fluid inclusion evidence for the link between boiling and epithermal Ag-Au mineralization in the La Luz area, Guanajuato Mining District, Mexico. *Ore Geol. Rev.* **89,** 143-170.

Orville P. M. (1963) Alkali ion exchange between vapor and feldspar phases. *Amer. J. Sci.* **261,** 201-237

Pudack C., Halter W.E., Heinrich C. A., and Pettke T. (2009) Evolution of magmatic vapor to gold-rich epithermal liquid: The porphyry to epithermal Transition at Nevados de Famatina, Northwest Argentina. *Econ. Geol.* **104**, 449-477.

Reyf F.G., Seltmann R., and Zaraisky G.P. (2000) The role of magmatic processes in the formation of banded Li, F-enriched granites from the Orlovka tanalum deposit, Transbaikalia, Russia: Microthermometric evidence. *Can. Mineral.* **38,** 915-936.

Roedder E. (1971) Fluid inclusion studies on the porphyry type ore deposits at Bingham, Utah, Butte, Montana, and Climax, Colorado. *Econ. Geol.* **66,** 98- 120.

Roman D.C., Cashman K.V., Gardner C.A., Wallace P.J., and Donovan J.J. (2006) Storage and interaction of compositionally heterogeneous magmas from the 1986 eruption of Augustine Volcano, Alaska. *Bull. Volcanol.* **68,** 240-254.

Rusk B.G., Reed M.H., Dilles J.H., Klemm L.M., and Heinrich C.A. (2004) Compositions of magmatic hydrothermal fluids determined by LA-ICP-MS of fluid inclusions from the porphyry copper-molybdenum deposit at Butte, MT. *Chem. Geol.* **210,** 173-199.

Saito G., Kazahaya K., Shinohara H., Stimac J., and Kawanabe Y. (2001) Variation of volatile concentration in a magma system of Satsuma-Iwojima volcano deduced form melt inclusion analyses. *J. Volcanol. Geoth. Res.* **108,** 11-31.

Schmitt A.K. (2001) Gas-saturated crystallization and degassing in large-volume, crystal-rich dacitic magmas from the Altiplano-Puna, northern Chile. *J. Geophys. Res.* **106,** 30561-30578.

Serafimovski T., Dolenec T., Tasev G., Rogan N., and Dolenec M. (2008) The composition of major minerals from the Buchim porphyry copper deposit, Republic of Macedonia. *Geologica Macedonia* **22,** 17-26.

Shinohara H., Iiyama T., and Matsuo S. (1989) Partition of chlorine compounds between silicate melt and hydrothermal solutions: I. Partition of NaCl-KCl. *Geochim. Cosmochim. Acta* **53,** 2617-2630.

Shmulovich K. I., Tkachenko S. I., and Plyasunova N. V. (1995) Phase equilibria in fluid systems at high pressures and temperatures. In *Fluids in the Crust* (eds. K. I. Shmulovich, B. W. D. Yardley, and G. G. Gonchar) Chapman & Hall, London. pp. 193-214

Signorelli S., and Capaccioni B. (1999) Behaviour of chlorine prior and during the 79 A.D. Plinian eruption of Vesuvius (southern Italy) as inferred from the present distribution in glassy mesostases and whole-pumices. *Lithos* **46,** 715-730.

Sillitoe R. (2010) Porphyry copper systems. *Econ. Geol.* **105,** 3-41.

Sourirajan S. and Kennedy G. C. (1962) The system H_2O-NaCl at elevated temperatures and pressures. *Amer. J. Sci.* **260**, 115-141.

Steele-MacInnis M. and Bodnar R. J. (2013) Effect of the vapor phase on the salinity of halite-bearing aqueous fluid inclusions estimated from the halite dissolution temperature. *Geochim. Cosmochim. Acta* **115,** 205-216.

Sterner S. M. and Bodnar R. J. (1984) Synthetic fluid-inclusions in natural quartz I. Compositional types synthesized and applications to experimental geochemistry. *Geochim. Cosmochim. Acta* **48,** 2659-2668.

Sterner S. M., Chou I-M., Downs R. T., and Pitzer K.S. (1992) Phase relations in the system NaCl-KCl-H_2O: V. Thermodynamic-PTX analysis of solid-liquid equilibria at high temperatures and pressures. *Geochim. Cosmochim. Acta* **56**, 2295-2309.

Sterner S. M., Hall D. L., and Bodnar R. J. (1988) Synthetic fluid-inclusions V. Solubility relations in the system NaCl-KCl-H_2O under vapor-saturated conditions. *Geochim. Cosmochim. Acta* **52,** 989-1005.

Student J.J. and Bodnar R.J. (1999) Synthetic fluid inclusions XIV: Coexisting silicate melt and aqueous fluid inclusions in the haplogranite- H_2O-NaCl-KCl system. *J. Petrol.* **40,** 1509-1525.

Thomas J.B., Bodnar R.J., Shimizu N., and Sinha A.K. (2002) Determination of zircon/melt trace element partition coefficients form SIMS analysis of melt inclusions in zircon. *Geochim. Cosmochim. Acta* **66,** 2887-2901.

Thomas R. and Klemm W. (1997) Microthermometric study of silicate melt inclusions in Variscan granites from SE Germany: Volatile contents and entrapment conditions. *J. Petrol.* **38,** 1753-1765.

Thomas R., Webster J. D., and Davidson P. (2006) Understanding pegmatite formation: the melt and fluid inclusion approach. In *Melt Inclusions in Plutonic Rocks* (ed. J. D. Webster). Min. Assoc. Can. Short Course 36, Ottawa, ON. pp. 189-210.

Ulrich T., Gunther D., and Heinrich C. A. (2002) The evolution of a porphyry Cu-Au deposit, based on LA-ICP-MS analysis of fluid inclusions: Bajo de la Alumbrera, Argentina. *Econ. Geol.* **97,** 1889-1920.

Wallace P.J., Anderson Jr A.T., and David A.M. (1999) Gradients in H_2O, CO_2, and exsolved gas in a large-volume silicic magma system: Interpreting the record preserved in melt inclusions from the Bishop Tuff. *J. Geophys. Res.* **104,** 20097-20122.

Webster J.D. (1992) Water solubility and chlorine partitioning in Cl-rich granitic systems: Effects of melt composition at 2 kbar and 800°C. *Geochim. Cosmochim. Acta* **56,** 679-687.

Webster J.D., and Duffield W.A. (1991) Volatiles and lithophile elements in Taylor Creek Rhyolite: Constraints from glass inclusion analysis. *Amer. Mineral.* **76,** 1628-1645.

Williams T.J., Candela P.A., and Piccoli P.M. (1995) The partitioning of copper between silicate melts and two-phase aqueous fluids: an experimental investigation at 1 kbar, 800 °C and 0.5 kbar, 850 °C. *Contrib. Mineral. Petrol.* **121** (4), 388-399.

Williams-Jones A. E., and Heinrich, C. A. (2005) Vapor transport of metals and the formation of magmatic-hydrothermal ore deposits. *Econ. Geol. Bull. Soc.* **100**(7), 1287-1312.

Yardley B. W. D. and Bodnar R. J. (2014) Fluids in the continental crust. *Geochemical Perspectives* **3**(1), 1-127.

Zajacz Z., Hanley J. J., Heinrich C. A., Halter W. E., and Guillong M. (2009) Diffusive reequilibration of quartz-hosted silicate melt and fluid inclusions: Are all metal concentrations unmodified? *Geochim. Cosmochim. Acta* **88,** 255-274.

Figures

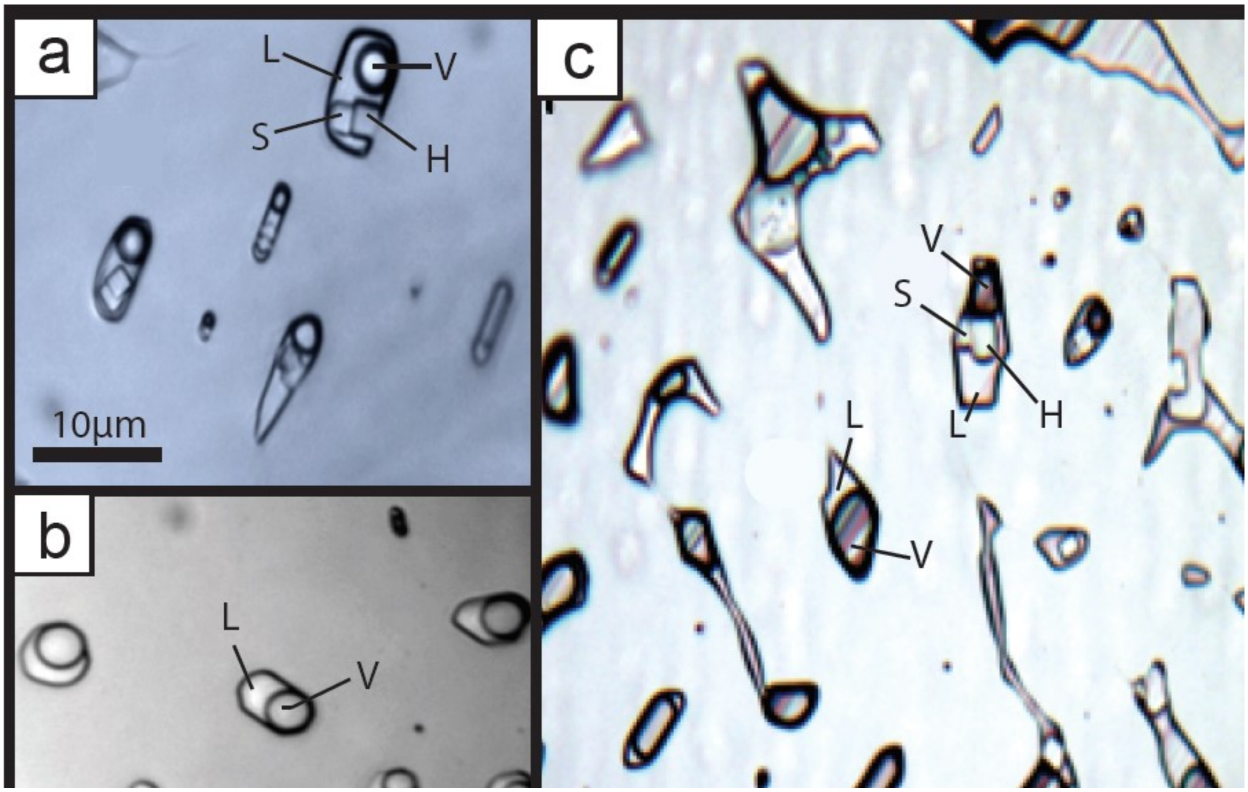

Fig. 1: Photomicrographs of synthetic fluid inclusions (FI) trapped in the two-phase liquid + vapor field in the H_2O-NaCl-KCl system (all photos taken at room temperature). (a) FI that trapped the liquid phase and contain halite (H) and sylvite (S) daughter minerals, along with a liquid (L) and a vapor bubble (V) at room temperature; (b) FI that trapped the vapor phase contain only liquid and a vapor bubble at room temperature; (c) field of view showing some FI that trapped the liquid phase (mostly in the upper portion of the photo), some that trapped the vapor phase (mostly in the lower part of the photo) and some that trapped mixtures of liquid and vapor (mostly in the middle portion of the photo). The formation conditions for (a) are 700°C/500 bars (Na/K=1:1), for (b) are 600°C/750 bars (Na/K=1:1), and (c) 700°C/500 bars (Na/K=3:1).

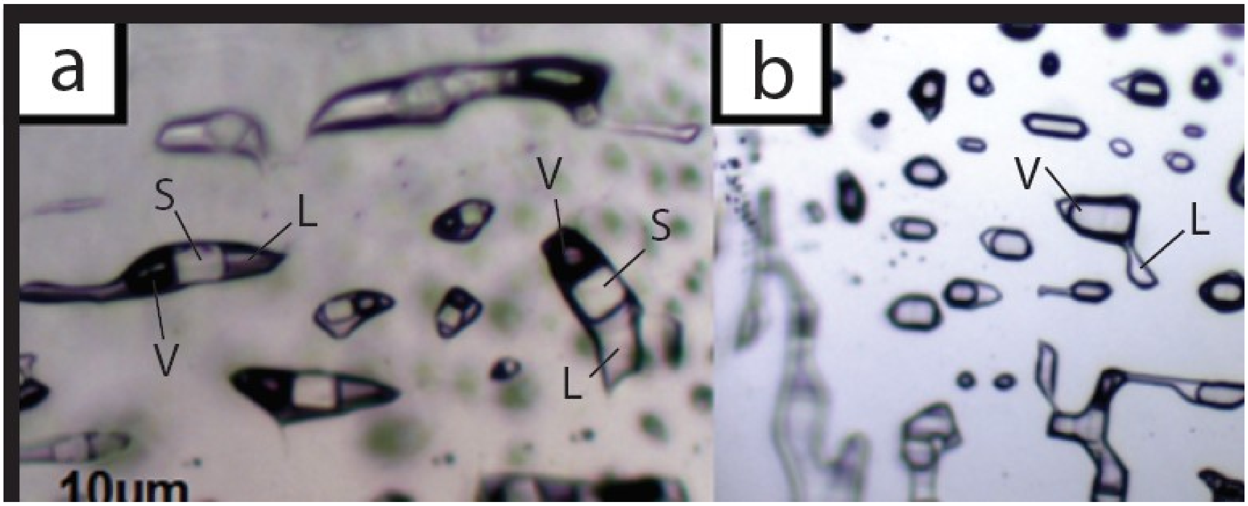

Fig. 2: Photomicrographs of FI that trapped the liquid phase (a) and the vapor phase (b) in the H_2O-KCl system. FI that trapped the liquid phase contain a sylvite daughter mineral along with liquid and vapor at room temperature, while FI that trapped the vapor phase only contain liquid and vapor at room temperature. The formation conditions for (a) and (b) are 700°C/500 bars.

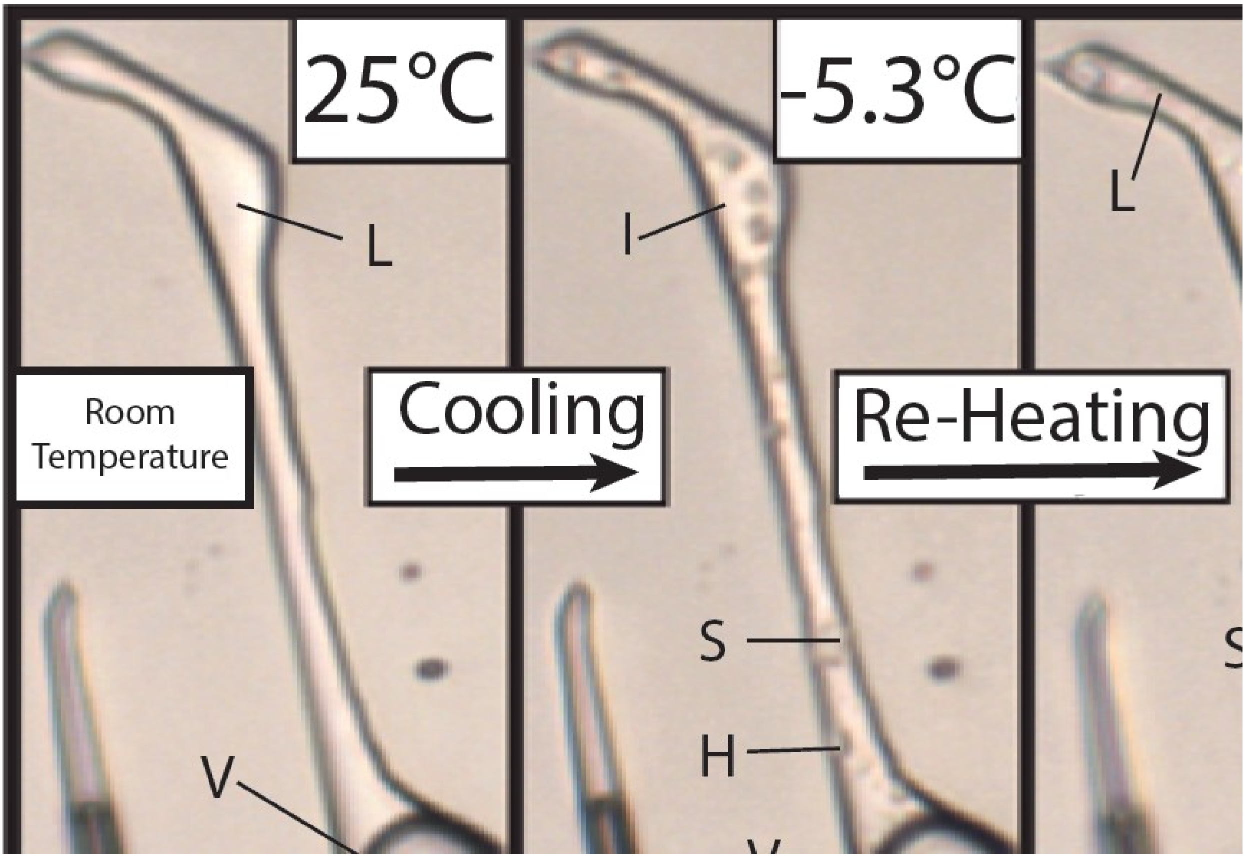

Fig. 3: Photomicrographs of an FI that trapped the liquid phase but which remained as a metastable, super-saturated liquid and did not precipitate daughter minerals during cooling to room temperature. The image on the left shows the FI containing only liquid (L) and vapor (V) at room temperature, after quenching from formation conditions. To nucleate daughter minerals, the FI was cooled to ~-190°C) and then reheated, during which time solid phases precipitated. The center image shows the FI after heating from -190°C to -5.3°C, and the FI contains several small crystals of halite (H) and sylvite (S), as well as ice (I). The image on the right shows the FI at room temperature after cooling to -190°C, showing halite (H) and sylvite (S) daughter minerals. The salinity of the liquid trapped in the FI can then be determined from the dissolution temperatures of the halite and sylvite daughter minerals after they have been nucleated by this temperature cycling process. The formation conditions of this FI are 700°C/1000 bars (Na/K=1:1).

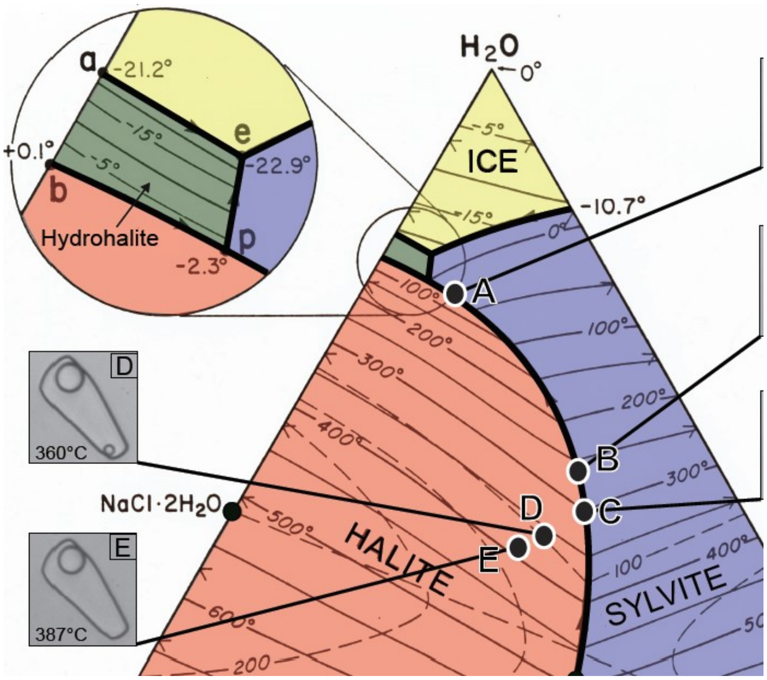

Fig. 4: Phase equilibria in the vapor-saturated H_2O-NaCl-KCl ternary system modified from Sterner et al. (1988), showing an example PTX path followed during heating of a fluid inclusion that contains halite and sylvite daughter minerals. The heavy lines represent cotectics separating fields in which one solid phase (ice, hydrohalite, sylvite or halite) is stable. Light solid lines represent isotherms in degree Celsius, and dashed light lines represent vapor pressures in bars. Point A is on the halite-sylvite cotectic and represents the composition of the liquid in equilibrium with halite and sylvite at room temperature. As the FI is heated, the composition of the liquid moves along the halite-sylvite cotectic until one of the two solid phases completely dissolves (point C; the sylvite daughter mineral completely dissolves in this example). With continued heating, the liquid composition follows a path from point C on the cotectic towards the apex of the remaining solid phase (NaCl in this example) until the solid phase (halite) completely dissolves (point E). At this point, the total salinity, as well as the proportions of NaCl and KCl can be determined. For this example, the halite dissolves at 387°C giving a total salinity of 66.5 wt%, with 29.5 wt% NaCl and 37.0 wt% KCl. Note that the path from the halite-sylvite cotectic to the temperature of halite dissolution is not a straight line but, rather is slightly curved owing to the fact that the "halite" is not pure NaCl but instead contains a small amount of KCl in solid-solution (see Sterner et al., 1988 for a detailed discussion). Note that all temperature units are in °C.

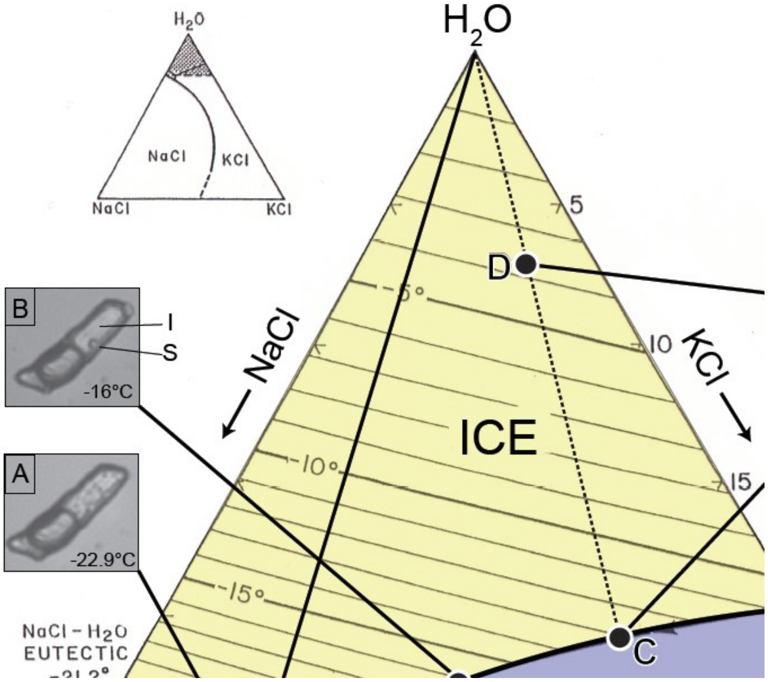

Fig. 5: Phase equilibria in the ice stable region of the H_2O-NaCl-KCl ternary system modified from Hall et al. (1988), showing an example PTX path followed by a FI that trapped the vapor phase in the two-phase field. During reheating from low temperatures (~-190°C), first melting occurs at the eutectic point (-22.9°C for this system) where hydrohalite, sylvite, and ice coexist with liquid and vapor (point A). As the FI is heated further, one of the solid phases will completely dissolve (hydrohalite in this example) and the composition of the liquid phase moves along the cotectic of the remaining two solid phases (the sylvite-ice cotectic in this example) until one of the solid phases (sylvite in this example) dissolves completely (point C). From this point, the composition of the liquid moves directly towards the H_2O apex as the aqueous solution is diluted by melting of ice, until the ice completely dissolves (point D for this example). At this point, the total salinity, as well as the proportions of NaCl and KCl in the inclusion can be determined. For this example, the ice phase melts at –3.8°C giving a total salinity of 7.37 wt%, with 2.09 wt% NaCl and 5.28wt% KCl. If sylvite is the phase that disappears at the eutectic point, then the liquid composition would follow the hydrohalite-ice cotectic until the hydrohalite phase disappears, and the composition would then move towards the ice apex with further heating, as in the previous example. Note that all temperature units are in °C.

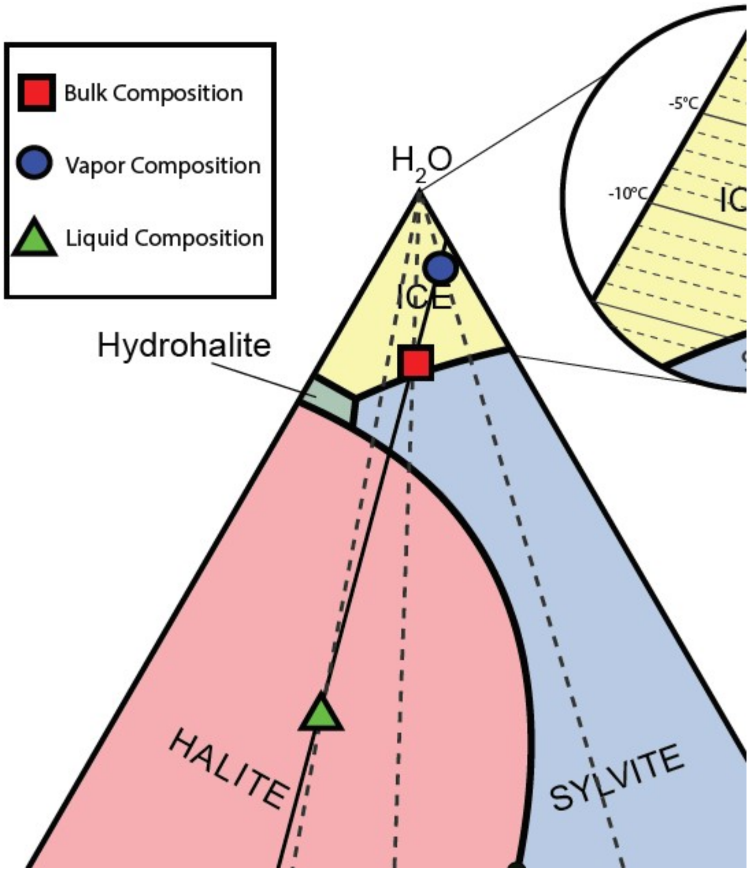

Fig. 6: H_2O-NaCl-KCl ternary system showing the methodology followed to determine compositions of coexisting liquid and vapor phases. The example shows a fluid with a known bulk composition (red square) that was initially loaded into the experimental capsule and which has undergone immiscibility and separated into a vapor phase (blue circle) coexisting with a liquid phase (green triangle) at experimental conditions. Compositions of the liquid and vapor phases must lie along a tie line (solid black line) that passes through the bulk composition. The composition of the liquid phase is obtained from the measured halite and sylvite dissolution temperatures as shown on Fig. 4. The intersection of the tie line that starts at the liquid composition and passes through the bulk composition with the measured ice melting temperature in the vapor-rich inclusion represents the composition of the vapor phase. The Na/K ratio of each phase (liquid and vapor) in equilibrium at the conditions of trapping is determined by a tie line that extends from the H_2O apex and through the composition of the phase (either liquid or vapor; grey dashed lines) to the NaCl-KCl binary.

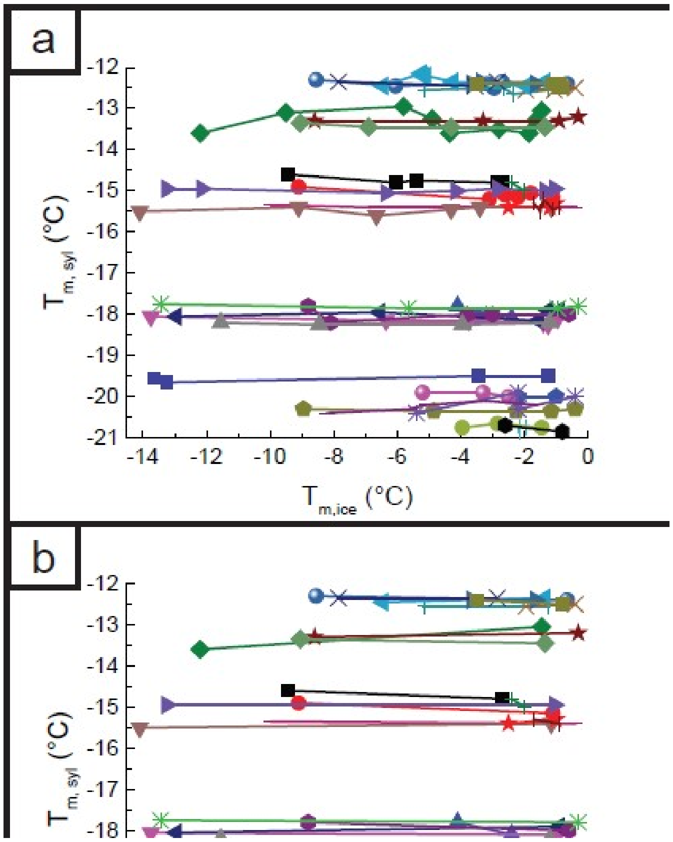

Fig. 7: Melting temperature of ice plotted against the dissolution temperature of sylvite in FI that trapped the "vapor" phase. Fig. 7a shows all data for each sample and Fig. 7b shows only the highest and lowest ice melting temperatures for each sample. The range in salinity (or ice-melting temperature) reflects the fact that FI that trap the vapor phase always trap some small amount of the higher salinity, wetting liquid phase (See Bodnar et al., 1985; their Fig. 9 and Table 1). The sylvite melting temperatures are essentially independent of ice melting temperature, which reflects the nearly 1:1 partitioning of Na and K between liquid and vapor. As a result, trapping of some liquid along with vapor results in an increase in total salinity (and a lower ice-melting temperature) but has a small effect on the sylvite dissolution temperature, which is dependent on the Na/K ratio of the solution. The formation conditions corresponding to the different sample numbers listed on the right are given in Table 1.

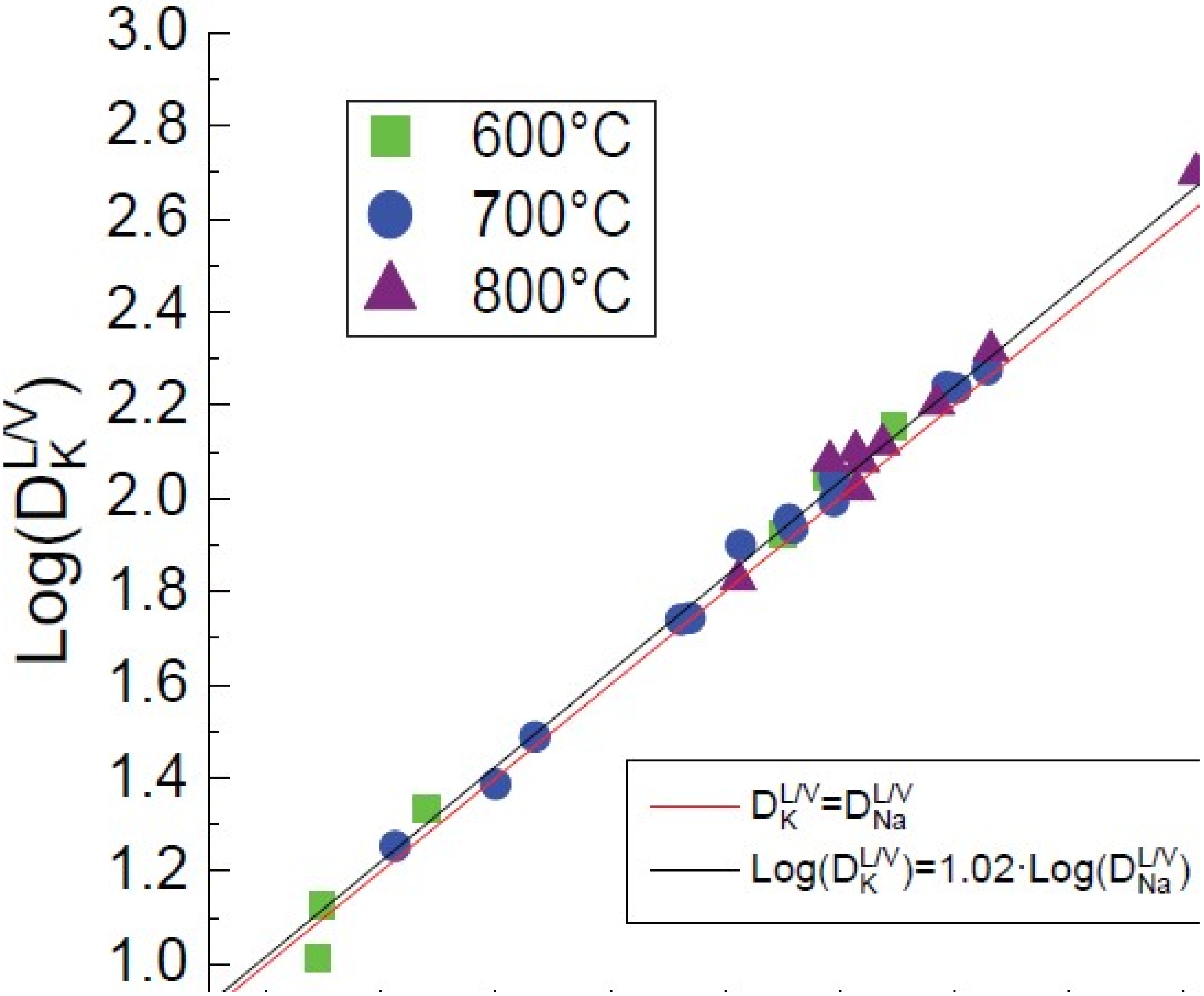

Fig. 8: Distribution constants of sodium plotted versus the distribution constants for potassium, identified according to the temperature of trapping of the FI. The solid red line represents a 1:1 partitioning and the solid black line represents a linear fit of the data. The slope of the fit line is slightly greater than the slope of the 1:1 line, indicating that the liquid phase is slightly more enriched in potassium compared to the vapor phase, i.e., sodium preferentially partitions into the vapor relative to potassium.

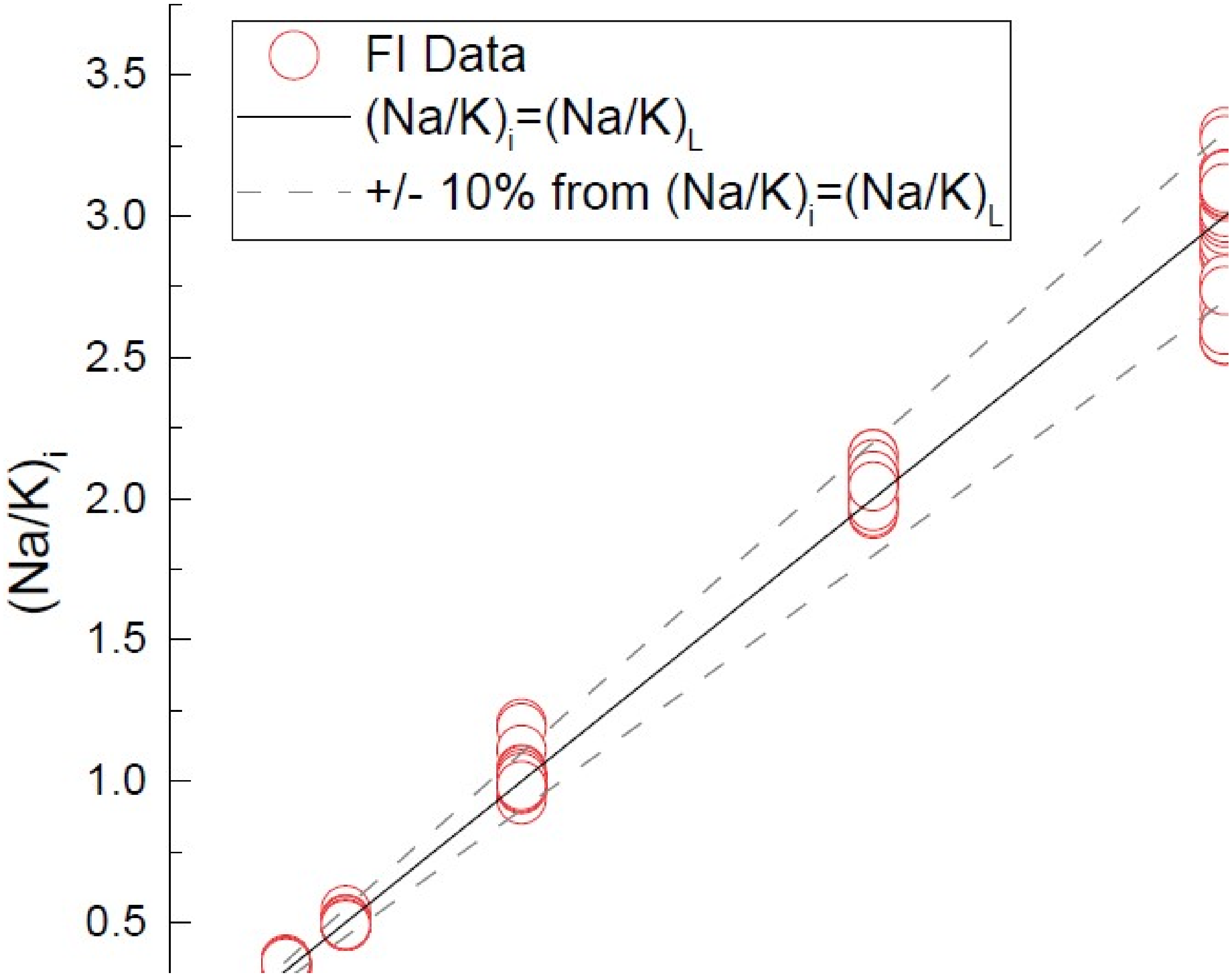

Fig. 9: The Na/K ratio of the bulk fluid versus the Na/K ratio of the liquid phase. Points that plot on the solid line represent liquid compositions that have the same Na/K ratio as the bulk fluid, while points that plot within the area bounded by the two dashed grey lines represent a liquid that has a Na/K ratio that differs from the bulk Na/K ratio by 10% or less. The majority of the Na/K ratios of the liquid phase trapped in the FI fall within the 10% region, indicating that the Na/K ratio of the liquid and vapor phases are similar to that of the bulk fluid, i.e., Na and K are partitioned equally between the liquid and vapor phases.

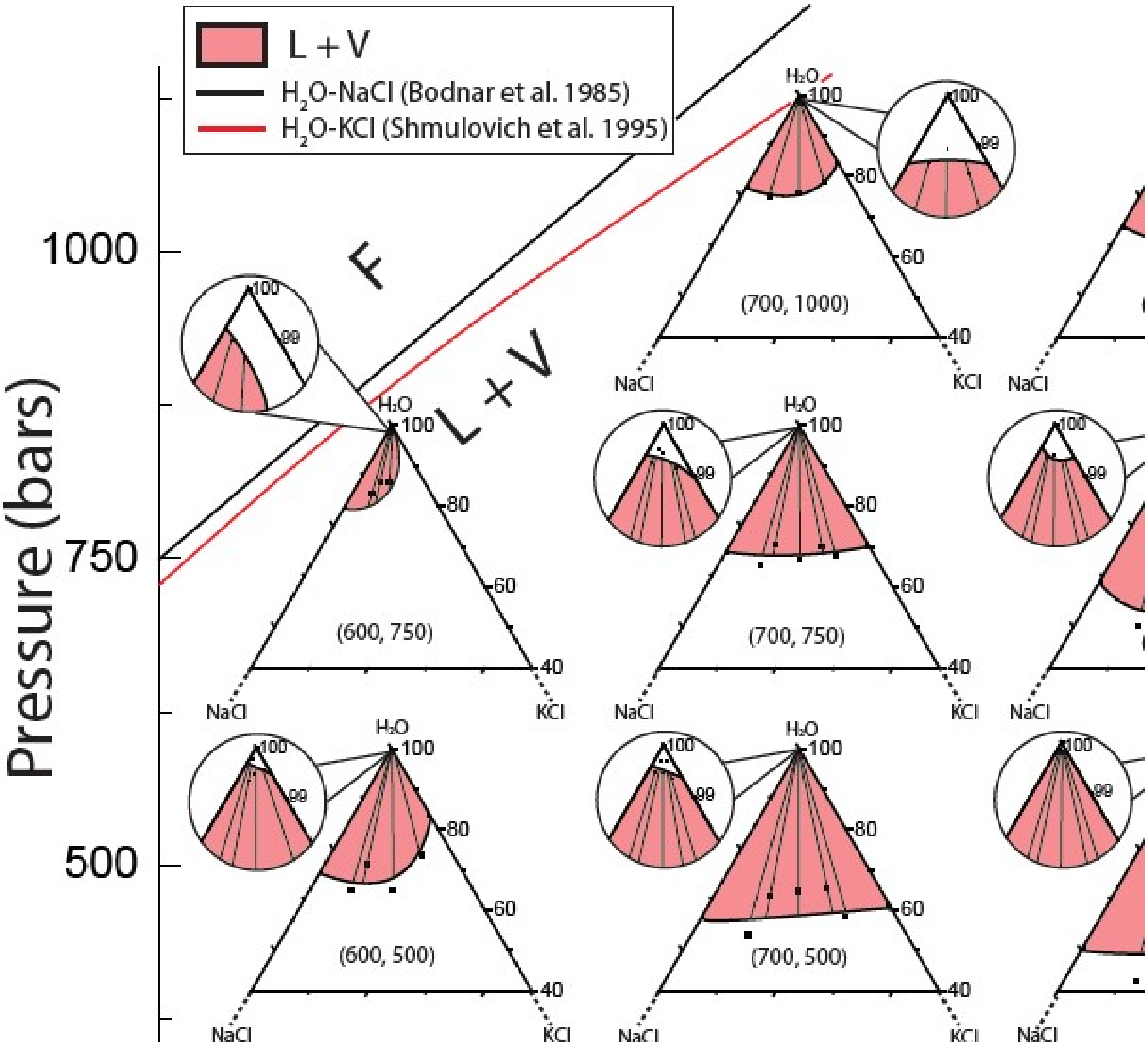

Fig. 10: Ternary diagrams showing the extent of the liquid + vapor immiscibility field at the experimental PT conditions of this study. The solid black and red lines in the upper left of the larger PT diagram represent the locus of critical points for a fluid of 10 wt% NaCl (Bodnar et al. 1985) and 10 wt% KCl (Shmulovich et al. 1995), respectively. The two-phase liquid + vapor region expands as temperature increases and pressure decreases. The numbers shown in the unshaded (white) area of each ternary represent the temperature and pressure, respectively.

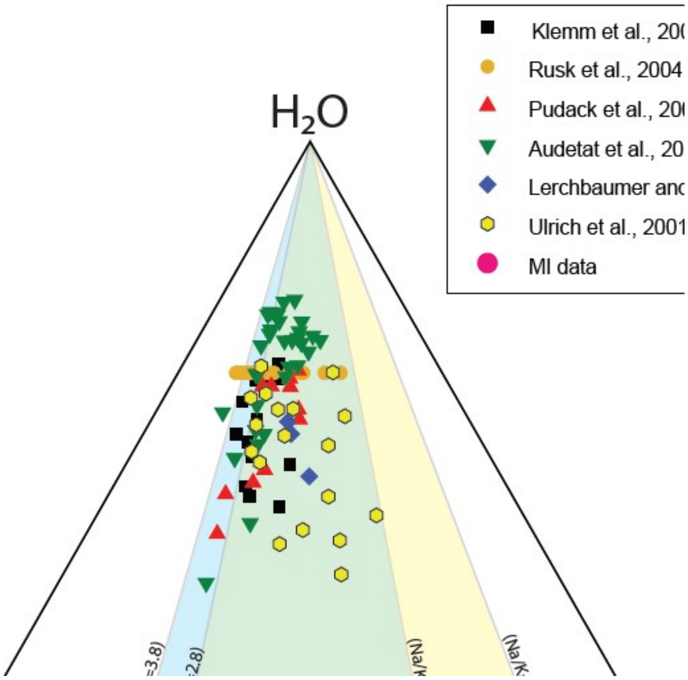

Fig. 11: Comparison of results this study with Na/K compositions of melts, crystals and natural fluid inclusions from the porphyry copper environment. The original Na/K ratio of the natural brines and the measured NaCl equivalent salinity are used to normalize the composition of the brines to the system H_2O-NaCl-KCl. The majority of the data show Na/K ratios between 3.8 and 0.64 (region shaded blue and green). The calculated Na/K ratio of the melt from which the fluids exsolved is between 2.8 and 0.26 (region shaded green and yellow). Na/K ratios from 300 MI data points of various granites are shown by the large pink circles, ~96% of which fall in the predicted region of Na/K ratios of 2.8-0.26. Finally, the light pink and orange squares along the NaCl-KCl binary represent the Na/K ratio of a K-Feldspar from a PCD in Buchim, Macedonia (Serafimovski et al., 2008) and the Na/K ratio of the fluid before reacting to form the Feldspar calculated using crystal-fluid partitioning behavior, respectively. Sources for the MI data are: Webster and Duffield, 1991; Signorelli and Capaccioni, 1999; Thomas et al., 2002; Thomas and Klemm, 1997; Lu et al., 1992; Badanina et al., 2004; Davidsion et al., 2005; Förster et al., 1999; Hansteen and Lustenhouwer, 1990; Haapala and Thomas, 2000; Hildreth, 1981; Reyf et al., 2000; Anderson et al., 1989; Wallace et al., 1999; Dunbar and Hervig, 1992; Bacon et al., 1992; Saito et al., 2001; Schmitt, 2001; Roman et al., 2006; and Thomas et al., 2006.

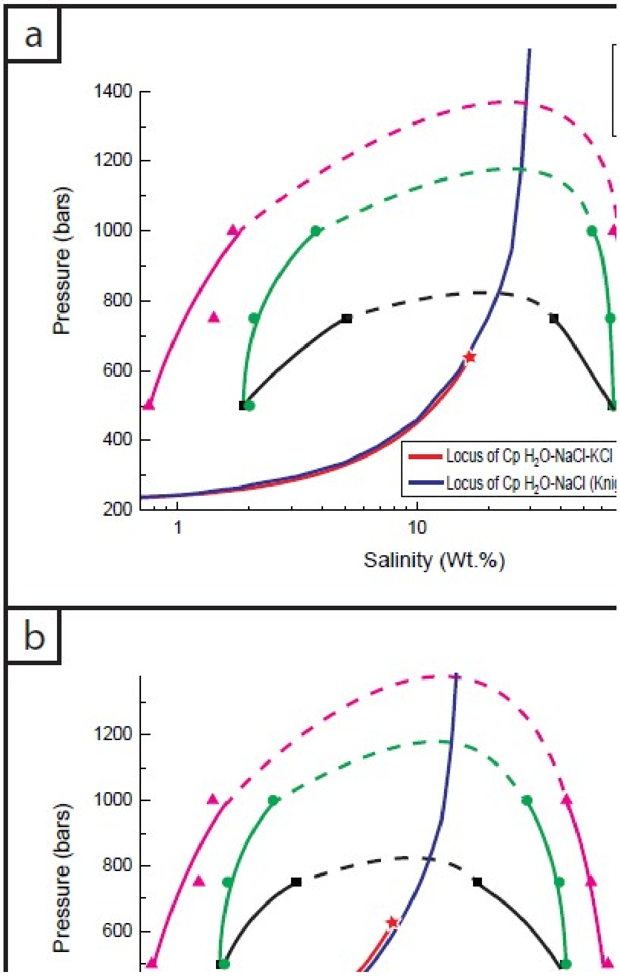

Fig. 12: PX diagrams showing phase relations in the H_2O-NaCl-KCl system for a composition with equi-molar proportions of Na and K, plotted as a function of total salinity in weight percent (a) and molality (b). Also shown is the locus of critical points for the system H_2O-NaCl from Knight and Bodnar (1989) and for the system H_2O-NaCl-KCl from Azbej (2006). The star symbol indicates that maximum salinity for which data are available for the ternary system. The dashed portions of the isotherms show the extrapolations of isotherms to higher pressures. The isotherms for ternary compositions have been extrapolated to be consistent with the shape of the solvus in the H_2O-NaCl system, but the actual positions of the isotherms above the limits of experimental data are unknown. Note that with increasing pressure at any temperature the compositions of the liquid and vapor phases approach each other and become equal at the critical point.

Tables

Table 1: Salinities for liquid (L) and vapor (V) phases in equilibrium at experimental PT conditions in the H_2O-NaCl-KCl system

Sample Number	**T_f (°C)**	**P_f (bars)**	$\left(\frac{\mathrm{Na}}{\mathrm{K}}\right)_i$	**Total Salinity (L) (Wt%)**	**Total Salinity (V) (Wt%)***	**Number of Measurements$^+$**
11	600	500	0.33	58.4	1.32	1
25	600	500	1	66.1-67.0	1.89	7
6	600	500	2	57.4-57.6	1.64	4
24	600	500	3	64.7-65.5	1.42	6
-	600	750	0.33	(-)	(-)	(-)
-	600	750	0.5	(-)	(-)	(-)
1	600	750	1	37.4-37.5	5.09	3
3	600	750	2	36.4-36.7	4.30	4
16	600	750	3	41.1-41.2	3.43	3
12	700	500	0.33	73.5-73.6	2.52	2
-	700	500	0.5	66.7-67.3	1.19	6
7	700	500	1	66.7-66.8	2.00	5
8	700	500	2	66.7-67.4	1.09	9
26	700	500	3	73.9-75.2	1.78	4
23	700	750	0.33	65.2-65.4	3.33	4
5	700	750	0.5	60.4-63.8	2.88	8
2	700	750	1	64.6-64.9	2.09	4
4	700	750	2	58.6-60.5	1.72	5
18	700	750	3	64.9-65.0	2.56	3
29	700	1000	0.33	51.4-51.8	5.70	6
28	700	1000	1	53.2-55.0	3.78	22
27	700	1000	3	52.4-54.0	4.39	13
13	800	500	0.33	81.1	0.81	1
9	800	500	0.5	76.4-76.5	0.60	2
15	800	500	1	77.8	0.76	1
14	800	500	2	73.1-73.7	0.55	3
10	800	500	3	82.1-82.7	0.71	4
30	800	500	3	82.6-83.6	0.71	9
22	800	750	0.33	73.1-76.4	2.74	3
21	800	750	0.5	75.6-75.9	2.65	4
20	800	750	1	73.7-73.9	1.42	2
19	800	750	2	73.2-73.3	2.17	3
17	800	750	3	77.4-77.7	2.23	6
33	800	1000	0.33	65.1-66.8	1.62	6
32	800	1000	1	66.8-67.1	1.70	11
31	800	1000	3	65.7-66.3	2.83	9

Sample number refers to sample numbers shown on Fig. 7;

T_f and P_f correspond to the fluid inclusion formation temperature and pressure, respectively;

$(Na/K)_i$ corresponds to the Na/K molar ratio of the initial fluid loaded into the capsule;

Total salinity (L) and Total salinity (V) correspond to the total salinity of the liquid-rich and vapor-rich inclusions, respectively, determined from microthermometry;

(-) indicates PT conditions at which immiscibility was not observed

[*] The composition of the vapor trapped in the FI with the highest ice melting temperature

[+] The number of liquid-rich FI measured. As noted in the text, only the single FI that had the highest ice melting temperature was used to determine the salinity of the vapor phase.

Table 2: Salinities for liquid (L) and vapor (V) phases in equilibrium at experimental PT conditions in the H_2O-KCl system

T_f (°C)	P_f (bars)	Total Salinity (L) (Wt%)	Total Salinity (V) (Wt%)*	Number of Measurements+
500	300	57.0-57.1	4.31	6
600	500	43.7-44.1	2.17	8
600	750	(-)	(-)	(-)
700	500	72.4-72.5	2.49	4
700	750	63.3-64.2	3.99	4
700	1000	44.3-44.5	4.73	5
800	500	80.1-80.3	0.87	4
800	750	70.0-70.5	1.74	2
800	1000	49.8-54.4	1.95	2

T_f, P_f, Total salinity (L) and Total salinity (V) as described in Table 1;

(-) indicates PT conditions at which immiscibility was not observed

* The composition of the vapor trapped in the FI with the highest ice melting temperature (lowest salinity)

\+ The number of liquid-rich FI measured. As noted in the text, only the single FI that had the highest ice melting temperature was used to determine the salinity of the vapor phase.

Table 3: Distribution constants (D) for sodium, potassium, and chlorine in the H_2O-NaCl-KCl system calculated from the microthermometric data, as well as the average Na/K ratio in the liquid phase after immiscibility.

T_f (°C)	**P_f (bars)**	$\left(\frac{Na}{K}\right)_i$	**Average**$\left(\frac{Na}{K}\right)_L$	$D^{L/V}_{Na}$	$D^{L/V}_{K}$	$D^{L/V}_{Cl}$
600	500	0.33	0.35	100.44	106.41	104.81
600	500	1	0.97	94.56	110.54	81.25
600	500	2	1.98	79.87	84.13	102.04
600	500	3	2.99	124.49	143.09	128.68
600	750	0.33	(-)	(-)	(-)	(-)
600	750	0.5	(-)	(-)	(-)	(-)
600	750	1	1.17	12.27	10.33	11.29
600	750	2	2.02	12.50	13.38	12.78
600	750	3	3.01	19.08	21.47	19.63
700	500	0.33	0.35	97.82	110.67	107.00
700	500	0.5	0.49	153.95	173.77	166.71
700	500	1	1.02	97.70	98.60	98.14
700	500	2	2.04	181.11	188.90	183.60
700	500	3	2.82	159.98	171.95	162.96
700	750	0.33	0.35	52.86	54.85	54.32
700	750	0.5	0.51	54.87	55.30	55.16
700	750	1	0.99	81.66	90.02	85.66
700	750	2	2.09	82.94	86.16	83.96
700	750	3	2.87	67.25	79.44	70.03
700	1000	0.33	0.33	16.76	17.91	17.61
700	1000	1	1.00	29.41	30.74	30.06
700	1000	3	3.12	25.12	24.32	24.93
800	500	0.33	0.35	479.32	538.61	522.03
800	500	0.5	0.51	510.22	553.44	538.07
800	500	1	0.98	419.50	498.65	456.04
800	500	2	2.04	502.38	504.61	503.11
800	500	3	2.69	625.30	738.07	652.34
800	500	3	2.66	652.82	740.52	674.67
800	750	0.33	0.36	107.33	104.50	105.24
800	750	0.5	0.49	96.27	120.42	111.23
800	750	1	1.03	183.62	207.47	194.63
800	750	2	2.01	118.86	130.67	122.54
800	750	3	2.58	147.84	159.49	150.91
800	1000	0.33	0.35	109.20	120.09	117.04
800	1000	1	0.98	106.77	126.47	115.87
800	1000	3	3.10	66.58	67.03	66.69

T_f, and P_f, as described in Table 1;

D corresponds to the distribution constant for the components Na, K, and Cl;

$(Na/K)_i$ corresponds to the Na/K molar ratio of the initial fluid loaded into the capsule;
(-) indicates PT conditions at which immiscibility was not observed

Table 4: Fitting parameters for sodium and potassium in equation 3.

Coefficient	Na	K
A	-2080±190	-2130±200
B	$-1.79\text{x}10^{-3} \pm 1.6\text{x}10^{-4}$	$-1.83\text{x}10^{-3} \pm 1.7\text{x}10^{-4}$
C	6.13±0.30	6.28±0.33

Chapter 2: Shift in the Raman symmetric stretching band of N_2, CO_2, and CH_4 as a function of temperature, pressure, and density

Abstract

The Raman spectra of pure N_2, CO_2, and CH_4 were analyzed over the range 10 to 500 bars and from -160 to 200°C (N_2), 22 to 350°C (CO_2), and -100 to 450°C (CH_4). At constant temperature, Raman peak position, including the more intense CO_2 peak ($\nu+$) decreases (shifts to lower wavenumber) with increasing pressure for all three gases over the entire *PT* range studied. At constant pressure, the peak position for CO_2 and CH_4 increases (shifts to higher wavenumber) with increasing temperature over the entire *PT* range studied. In contrast, N_2 first shows an increase in peak position with increasing temperature at constant pressure, followed by a decrease in peak position with increasing temperature. The inflection temperature at which the trend reverses for N_2 is located between 0 to 50°C at pressures above ~50 bars and is pressure dependent. Below ~50 bars the inflection temperature was observed as low as -120°C. The shifts in Raman peak positions with pressure and temperature are related to relative density changes, which reflect changes in intermolecular attraction and repulsion. A conceptual model relating the Raman spectral properties of N_2, CO_2, and CH_4 to relative density (volume) changes and attractive and repulsive forces is presented here. Additionally, reduced temperature-dependent densimeters and barometers are presented for each pure component over the respective *PT* ranges. The Raman spectral behavior of the pure gases as a function of temperature and pressure is assessed to provide a framework for understanding the behavior of each component in multi-component N_2-CO_2-CH_4 gas systems in a future study.

1. Introduction

Natural fluids in which N_2, CO_2, and CH_4 are major constituents are common in metamorphic environments[1-5], sedimentary basins[6-7], and in some ore forming environments[8-9]. They have also been identified in the atmosphere and at the surface of some celestial bodies such as Titan, an icy moon of Saturn[10-11]. Furthermore, gas mixtures with similar compositions are commonly part of industrial processes, as well as in agricultural and municipal waste management, for example in the production of biofuels that are increasingly used for generating heat and electricity[12-13]. Thus, methods to analyze the physical and chemical properties of these gases and gas mixtures are needed for a variety of applications.

Raman spectroscopy offers a non-destructive method to characterize the properties of a wide variety of natural and synthetic materials. The intensity, width, and wavenumber (hereafter, referred to as "peak position") of a Raman peak provides information on the bonding environment of the molecules in the material of interest[14]. Raman peak positions of fluids have been shown to vary as functions of pressure, temperature, and density[4, 15-37]. Shifts in the Raman peak position of fluids with changing conditions have been related to the attractive and repulsive forces between molecules: attractive forces cause Raman peak position to shift to lower wavenumber, whereas repulsive forces cause Raman peak position to shift to higher wavenumber, and the overall direction of peak shift with changing conditions implies dominance of either attractive or repulsive forces[21, 27, 38-40].

The N_2 molecule has only one fundamental vibrational mode, the symmetric stretching of the N≡N bond, which is Raman active at ca. 2330 cm^{-1} at 1 bar[41]. Several studies have investigated the change in the Raman spectral properties of N_2 over a range of pressures at room temperature[19, 23-24], at low temperatures near or below the critical point[25-27], at elevated temperatures[28-30, 42], and in gas mixtures[13, 15, 19, 31].

The CH_4 molecule exhibits four fundamental vibrational modes that are Raman active, at ca. 3019, 2917, 1534, and 1309 cm^{-1} at 1 bar, but only the 2917 cm^{-1} mode (ν_1), which represents the symmetric stretching of the C-H bond, is commonly observed in Raman spectra[4]. The shift in Raman peak position of the symmetric stretching mode of CH_4 with pressure has been studied at room temperature[16-17, 22, 32-34], at lower temperatures down to -150°C[16-17, 34], at elevated temperatures[34], and in mixtures[13, 15, 19, 31, 35-37].

Due to its linear geometry, CO_2 should show only one fundamental vibrational mode that is Raman active (symmetric stretching of the C=O bond) at ca. 1333 cm^{-1}. However, this mode exhibits nearly the same energy as the first overtone of the infrared-active bending mode[43]. The interaction between these two modes results in a splitting of the 1333 cm^{-1} vibrational band into two bands, nominally located at 1388 and 1285 cm^{-1} at 1 bar, in a process known as Fermi resonance[4, 44]. These two peaks are referred to as the Fermi diad and the distance between the two peaks has been used to estimate the density of CO_2[18-20, 44-47].

In this study, we explore the vibrational properties of pure N_2, CH_4, and CO_2 over broad pressure and temperature (*PT*) ranges to investigate the relationships between Raman spectral features, pressure, and temperature. We interpret the results in terms of relative volumetric (density) changes, attractive and repulsive forces between molecules, and proximity to the critical point. This study thus expands the available Raman peak shift data on N_2, CH_4, and CO_2 to a larger *PT* range and provides a starting point for examining variations in Raman spectral properties of these gases in higher order systems in future studies.

2. Methods

Raman spectra for N_2, CH_4, and CO_2 were collected from 10 to 500 bars over temperature ranges of -160 to 200°C (N_2), -100 to 450°C (CH_4), and 22 to 350°C (CO_2) using a JY Horiba LabRam HR (800 mm spectrometer) Raman microprobe equipped with a high-pressure optical capillary system (similar to that described by Chou et al.[48]) and a Linkam CAP500 capillary heating and cooling stage. The Raman microprobe is equipped with an 1800 grooves/mm grating, a slit width of 150 μm, a confocal aperture of 400 μm, and a 40x microscope objective (N.A. = 0.55). Excitation was provided by a 514 nm Laser Physics 100S-514 Ar^+ laser with an output power at the source of 50 mW. The lower temperature limit at which data were obtained for each gas corresponds to the intersection, of the liquid-vapor (L-V) curve for that gas along the isobar of interest, while the higher temperature limits reflect the decrease in signal strength with increasing temperature that precluded determination of Raman peak positions. The lower pressure limit is defined by the lowest pressure at which peaks with sufficient intensity above background to be quantified could be recorded, and the upper pressure limit was arbitrarily chosen to be 500 bars. Gases were commercially prepared by Airgas, Inc (99.999% pure).

The Linkam CAP500 capillary heating and cooling stage was connected to two manual pressure generators (HiP model 37-6-30) that allow the pressure inside the capillary tube to be controlled and varied. Generally, measurements along an isotherm began at low pressure, with the piston positioned such that it is mostly retracted from the sample cell, thus maximizing the sample volume. Starting at 10 bars, the pressure is increased incrementally, and the Raman peak position for the gas of interest was determined at each pressure along the isotherm until the maximum pressure (500 bars) was reached. Then, the temperature was changed and the process was repeated along that new isotherm. Additional details of the pressure system have been published elsewhere[16-20]. Pressure was monitored using a Precise Instruments pressure transducer (Model 645). The error in the pressure measurements was ±0.1% of the total output pressure reading. Temperature was monitored using the internal thermocouple of the CAP500 stage with an error in the temperature measurements of no more than ±0.4% of the total output temperature reading.

Raman analyses were conducted through a transparent 20 cm long square flexible fused silica capillary tube with an outer diameter of ~363 µm and an inner diameter of ~100 µm, prepared by Polymicro Technologies, LLC. Raman measurements were collected from the center of a 5 cm long portion of the capillary that was heated/cooled within the stage. The thermal gradient along this 5 cm portion is reported by Linkam to be ±0.2% of the total output temperature at the edges relative to the center. Spectra were collected only after the temperature and pressure stabilized and remained constant, with equilibration periods of at least 1 minute after the pressure was changed, and 10 minutes following a change in temperature. Collection times were selected to ensure that the Raman peaks of interest consisted of at least four data points above the background noise, with CO_2 and N_2 requiring the longest collection times (~180 s at 10 bars) and CH_4 requiring the shortest (~40 s at 10 bars). The collection times required to satisfy our threshold of at least four points above background noise decreased with increasing pressure and decreasing temperature. Certain low-pressure, high-temperature conditions were excluded from this study because spectra at these conditions, especially for N_2 and CO_2, did not show at least four data points above background noise. Additionally, the peak intensity-to-full-width at half-maximum (FWHM) ratio for each peak was never less than 500 counts/cm^{-1}, and in most cases was greater than 1000 counts/cm^{-1}. Both selection criteria, the peak intensity-to-FWHM and at least 4 data points above the noise, are applied to all peaks collected in this study, including both the more and less intense peaks that make up the Fermi diad. Three accumulations were collected for each gas, and this was repeated three times at each *PT* condition to produce three data points at each *PT* point and to assess the precision in the measurements. The average variation in the Raman peak positions of N_2, CO_2, and CH_4 was ±0.01, ±0.02, and ±0.01 cm^{-1}, respectively, and the average variation in the Fermi diad measurements was ±0.02 cm^{-1}. The Raman peak positions calculated from each of the three collections were averaged and used in all subsequent data analyses discussed below.

The peaks recorded in this study include: the symmetric stretching modes of N_2 (N≡N) and CH_4 (C-H), nominally located at 2331 and 2917 cm^{-1} at 1 bar, respectively, and the two peaks that comprise the Fermi diad of CO_2, nominally located at 1388 and 1285 cm^{-1} at 1 bar. Ne lines bounding the peaks of interest (N_2: 2253.58 and 2433.93 cm^{-1}; CO_2: 1031.42 and 1458.58 cm^{-1}; CH_4: 2851.49 and 2972.55 cm^{-1}) were collected simultaneously with each gas analysis to correct for spectrometer drift, following the correction method of Lin et al.[17]:

$$\nu^{i}_{corr} = \frac{1}{2}\left\{\left[\nu^{i}_{measured} + \left(\nu^{Ne,-}_{real} - \nu^{Ne,-}_{measured}\right)\right] + \left[\nu^{i}_{measured} + \left(\nu^{Ne,+}_{real} - \nu^{Ne,+}_{measured}\right)\right]\right\} \qquad (1)$$

where *Ne*± are the Ne emission lines that occur at higher (+) and lower (-) wavenumbers compared to the peak for the gas, *real* is the known position of the Ne emission line, and *measured* is the measured position of the Ne emission line. All spectra were fit using Labspec 5 software first using a linear baseline correction and then a Gaussian-Lorentzian peak fitting function.

Several recent studies have shown that, while the absolute peak position at a given *PT* condition shows slight variation from one study to another owing to laboratory and instrument specific factors, all studies show similar parallel trends in the variation in peak position with pressure[20, 35]. As such, to allow comparison between our new data and other published data, our results at 22°C were corrected to be consistent with data from Fall et al.[18] for CO_2 and Lin et al.[16] for CH_4. These studies chosen for inclusion were selected because they were conducted using the same Raman microprobe, and the same data collection and analysis procedure, that was used in this study. That is, if at 22°C and some pressure our measured peak position was, for example, 0.04 cm^{-1} higher than that reported in the studies referred to above for the same gas at the same *PT* condition, we systematically subtracted 0.04 cm^{-1} from our determined peak position to bring the results from the two studies into agreement. We also note, as has been described by others[20, 35], that the magnitude of the difference varied slightly from day to day; as such, the correction factor was determined before each analytical session and applied to the data collected during that session. Because there were no data for N_2 at 22°C in the literature that were collected using the same Raman system and collection protocol as used here, we determined our own calibration curve at this temperature and then used these results to correct the N_2 peak positions in all subsequent analyses. The only Raman spectral feature of interest in this study was peak position; accordingly, the full-width at half-maximum (FWHM), peak areas, and intensities of the peaks are not reported here. However, Fig. S1 in the supplementary material shows the relative change in peak intensity and width under changing *PT* conditions for each gas. All Raman peak positions and Fermi diad splitting measurements collected in this study, as well as the error in the Raman measurements determined, calculated densities, and compressibility factors, are presented in the Appendix.

3. Results

3.1 Isothermal Peak Shift with Changing Pressure

The relationship between pressure and Raman peak position over the temperature range of interest for each species is shown in Fig. 1. The critical point for CH_4 (Fig. 1a) is located at -83°C and 46 bars. For all isotherms that are above the critical temperature (-83°C), the liquid-vapor curve is not intersected as the pressure is increased and there is a smooth and continuous variation in peak position as a function of pressure. However, the L-V curve is intersected at ~23 bars along the -100°C isotherm. That is, during the experiment, as the pressure was increased from 10 bars at -100°C, the liquid-vapor curve for CH_4 is intersected at ~23 bars and liquid begins to condense from the vapor. At this point, the pressure remains constant until all of the vapor phase has condensed into liquid as the sample cell volume is decreased. This phase transition leads to a discontinuity in peak position versus pressure along the -100°C isotherm in Fig. 1a represented by the dashed portion of the isotherm. At this condition, if one were to focus the laser in the vapor phase, a peak position corresponding to the density of the vapor phase on the L-V curve would be obtained; similarly, if the laser were focused on the liquid phase, a peak position corresponding to the density of the liquid phase on the L-V curve would be obtained.

For CH_4, the peak position decreases with increasing pressure at constant temperature over the entire temperature range studied (Fig. 1a), and the CH_4 peak position increases with increasing temperature at constant pressure over the entire pressure range studied. Also shown on Fig. 1a is the critical point and the projection of the critical isochore for CH_4. Note that conditions to the left of the critical isochore correspond to fluids with densities greater than the critical density and are more liquid-like, whereas conditions to the right of the critical isochore correspond to fluids with densities less than the critical density and are more vapor-like.

The critical point of N_2 (Fig. 1b) is located at -147°C and 34 bars, and the -160°C isotherm intersects the L-V curve at ~12 bars, as shown by the discontinuity along the -160°C isotherm represented by the dashed portion of the isotherm. As with CH_4, the peak position of N_2 decreases at constant temperature with increasing pressure over the entire temperature range studied. However, unlike CH_4, there is a reversal in the direction of the peak shift at pressures above 50 bars and temperatures between 0 to 50°C (depending on pressure). At pressures above the transition pressure, the peak position increases with increasing temperature at constant pressure, rather than decreasing with increasing temperature at constant pressure. At temperatures <100°C and a pressure of ~50 bars, the projections of the isotherms in pressure-peak position space intersect. Below ~50 bars the temperature at which the peak position begins to decrease along an isobar is much lower than the temperature at which the peak position begins to decrease for pressures above 50 bars. For example, at 300 bars, the peak position decreases with increasing temperature above 35°C, while at 20 bars the peak position decreases with increasing temperature above -120°C. A possible explanation for this reversal in peak shift is provided below.

The critical point of CO_2 is located at 31°C and 74 bars, and the 22°C isotherm intersects the L-V curve at ~60 bars (Fig. 1c), as evidenced by the discontinuity along this isotherm represented by the dashed portion of the isotherm. Similar to both CH_4 and N_2, the peak position of CO_2 decreases with increasing pressure along an isotherm over the *PT* range studied. Also, similar to CH_4, at a constant pressure the peak position increases with increasing temperature over the pressure range studied.

3.2 Isothermal Peak Shift with Changing Density

The relationship between density and peak position for each gas along select isotherms is shown in Fig. 2. Densities were calculated using the NIST REFPROP version 10.0 program[49] and the Setzman and Wagner[50], Span et al.[51], and Span and Wagner[52] equations of state for CH_4, N_2, and CO_2, respectively. All three gases show a decrease in peak position with increasing density. Both CH_4 (Fig. 2a) and CO_2 (Fig. 2c) show an increase in peak position with increasing temperature at a constant density, with the exception of the temperature range 350-450°C for CH_4 (discussed further below). N_2 (Fig. 2b) shows a decrease in peak position with increasing temperature at constant density over the studied region. The density-peak position relationship for CH_4 shown in Fig. 2a is similar to that reported by Lin et al.[17] and Shang et al.[34]. The density-peak position relationship for CO_2 shown in Fig. 2c is similar to that reported by Wang et al.[47].

3.3 Isobaric Peak Shift with Changing Temperature

Fig. 3 shows the relationship between temperature and peak position (solid lines) and temperature and density (dashed lines) at 40-500 bars for each species. CH_4 (Fig. 3a) and CO_2 (Fig. 3c) both show an initial sharp increase in peak position with increasing temperature at a constant pressure above the critical temperature, followed by a more gradual increase in peak position at higher temperatures. Note that a discontinuity occurs along the 40-bar isobar for CH_4 as the L-V curve is crossed. N_2 (Fig. 3b) also shows an initial sharp increase in peak position with increasing temperature, followed by a more gradual increase at higher temperatures; however, at temperatures above ~0 to 50°C, depending on pressure, the peak position decreases with increasing temperature. The variations in peak position with temperature broadly mirror the changes in density with temperature along the same isobar. For example, at 40 and 100 bars, both the peak position and the density show significant variation as the temperature is increased from the lowest values plotted for all three gases, and a much less pronounced change in both peak position and density at higher temperature.

3.4 Compressibility Factor and Peak Position in *PT* space

Pressure-Volume-Temperature (*PVT*) data for gases may be examined using the unitless compressibility factor, Z, described by the following:

$$Z = \frac{PV_m}{RT} \tag{2}$$

where V_m is molar volume and R is the gas constant. For compressibility factors used in this study, V_m is determined using the calculated densities described above. By definition Z=1 for an ideal gas. A gas with a compressibility factor less than unity has a density greater than the density of an ideal gas at the same *PT* conditions, while a gas with a compressibility factor greater than unity has a density that is less than the density of an ideal gas at the same *PT* conditions. Additionally, values of Z less than unity indicate an environment dominated by attractive interactions between molecules, whereas values of Z greater than unity indicate an environment dominated by repulsive interactions between molecules. The relationship between the compressibility factor and peak position for each species studied here is shown in Fig. 4. At higher temperatures, the range in compressibility factors is smaller and remains close to unity, as is expected because at higher temperatures the fluid is more gas-like (lower density), and lower density fluids behave more ideally. All three species show an increasing range in the compressibility factor with decreasing temperature over the pressure range studied. This reflects the fact that the fluids are becoming less ideal (more liquid-like) at lower temperatures.

The variation in peak position in *PT* space is shown in Fig. 5. The solid black lines on Fig. 5 represent "isofreqs", or lines of constant peak position (constant wavenumber). Isochores (lines of constant density) are also plotted in Fig. 5. The isofreqs for CH_4 (Fig. 5a) and CO_2 (Fig. 5c) are roughly parallel to the isochores, especially for CO_2. For N_2 (Fig. 5b), the isofreqs and isochores remain roughly parallel at lower temperatures, but the isofreqs begin to curve and the slope changes from positive to negative with increasing temperature.

3.5 Densimeters and Barometers

Many studies have examined the relationship between Raman peak position and density or pressure, and have developed algorithms and equations describing the relationship. The goal of many of these studies was to develop densimeters and barometers that can be used to determine the pressures (or densities) of fluids contained in natural fluid inclusions from various geologic environments, based on Raman analysis[16, 18, 20, 34, 45-47]. As such, we have fit our data, shown in Figs. 1 and 2 and included in the Appendix, to develop equations describing the relationship between pressure, temperature and density for the gases studied here. The main goal of the present study was not to develop densimeters or barometers, but rather to understand the relationship between Raman peak positions as a function of pressure, temperature, and density for use in a follow-up study to examine the behavior of these gases in mixtures. Nonetheless, the equations developed and presented below may be used to determine the pressure (or density) of single component fluids trapped in fluid inclusions (and in other applications) as a function of peak position and temperature.

In developing the relationship between peak position, pressure, density and temperature in this study, we employed the reduced temperature (T_R) of each gas:

$$T_R = \frac{T}{T_C} \tag{3}$$

where T is temperature in Kelvin, T_c is the critical temperature of the gas in Kelvins. Using the reduced temperature, T_R, rather than the actual temperature, offers no advantages when evaluating data for the pure gases, but it does offer significant advantages when considering gas mixtures at temperatures at which the gas mixture does not undergo a phase change (i.e., consist of liquid and vapor, or two immiscible fluid phases) while one of the components of the mixture would undergo a phase change at those same *PT* conditions. For example, pure CO_2 undergoes a phase transition at 22°C when the liquid-vapor curve is intersected (see Fig. 1c). However, for a gas mixture containing CO_2, CH_4, and N_2 with a critical point sufficiently less than 22°C such that the maxcondentherm of the dew point curve is at a temperature lower than 22°C,a phase change will not occur as pressure is changed at 22°C. Thus, the peak positions and Fermi diad splitting measured for CO_2 in the gas mixture change continuously as pressure is increased at 22°C while a discontinuity occurs in the peak positions and Fermi diad splitting in pure CO_2 at the same conditions when the L-V curve is crossed. Using the reduced temperature for this example mixture would circumvent the phase transition and the accompanying discontinuity in pressure-peak position space experienced by pure CO_2. As such, the reduced temperature, T_R, is used in the densimeters and barometers presented here to facilitate incorporation of these algorithms into those being developed for gas mixtures.

The densimeter for CH_4 is valid from 10 to 500 bars and -100 to 450°C, and is given by:

$$\rho_{CH_4} = \sum_{i=0}^{2} \sum_{j=2}^{2} A_{i,j} (T_R)^i (\nu - 2917)^j \tag{4}$$

where ρ is density in g/cm^3 and v is the Raman peak position in cm^{-1}. The fitting coefficients and associated errors are given in Table 1. Eq. 4 has an R^2 of 0.998 and a standard error of ± 0.003 g/cm^3. The barometer for CH_4, which is valid from 10 to 500 bars and -80 to 350°C, is given by:

$$P_{CH_4} = \frac{\sum_{i=0}^{2} \sum_{j=0}^{2} A_{i,j} (\nu - 2917)^i (T_R)^j}{1 + \sum_{k=0}^{2} \sum_{l=0}^{2} B_{k,l} (\nu - 2917)^k (T_R)^l} \tag{5}$$

where *P* is in bars. The fitting coefficients and associated errors are given in Table 2. Eq. 5 has an R^2 of 0.997 and a standard error of ± 9.8 bars. Because the data from Lin et al.[17] at 22°C were used to develop the CH_4 barometer and densimeter, Eqs. 4 and 5 agrees with Lin et al.[17] within analytical error.

The densimeter for N_2 is valid from 10 to 500 bars and -160 to 200°C and is given by the following:

$$\rho_{N_2} = \sum_{i=0}^{2} \sum_{j=2}^{2} A_{i,j} (T_R)^i \left[ln \left\{ \left(\frac{\nu \cdot 1000}{2330} \right) - 998 \right\} \right]^j \tag{6}$$

The ν term in Eq. 6 is presented in this manner to accentuate the small changes in the Raman peak position of N_2 with changing pressure over the *PT* range studied. The fitting coefficients and associated errors are given in Table 3. Eq. 6 has an R^2 of 0.999 and a standard error of ± 0.008 g/cm^3. The barometer for N_2 is valid from 10 to 500 bars and -140 to 200°C and is given by the following:

$$P_{N_2} = \frac{\sum_{i=0}^{2} \sum_{j=0}^{2} A_{i,j} \left[ln \left\{ \left(\frac{\nu \cdot 1000}{2330} \right) - 998 \right\} \right]^j (T_R)^j}{1 + \sum_{k=0}^{2} \sum_{l=0}^{2} B_{k,l} \left[ln \left\{ \left(\frac{\nu \cdot 1000}{2330} \right) - 998 \right\} \right]^k (T_R)^l} \tag{7}$$

The fitting coefficients and associated errors are given in Table 4. Eq. 7 has an R^2 of 0.996 and a standard error of ± 12.4 bars.

For CO_2, the splitting of the Fermi diad is more commonly used than a single peak position to correlate Raman spectral features with pressure or density because the distance between the two peaks that make up the Fermi diad remains relatively constant and independent of instrument drift. As such, the densimeter and barometer for CO_2 were developed using the Fermi diad splitting. The densimeter for CO_2 is valid from 10 to 500 bars and 22 to 350°C and is given by the following:

$$\rho_{CO_2} = \sum_{i=0}^{1} \sum_{j=2}^{2} A_{i,j} (T_R)^i (\Delta - 100)^j \tag{8}$$

where *Δ* is the Fermi diad splitting in cm^{-1}. The fitting coefficients and associated errors are given in Table 5. Eq. 8 has an R^2 of 0.999 and a standard error of ± 0.006 g/cm^3. The barometer for CO_2 is valid from 10 to 500 bars and 35 to 350°C and is given by the following:

$$P_{CO_2} = \frac{\sum_{i=0}^{2} \sum_{j=0}^{2} A_{i,j} (\Delta - 100)^i (T_R)^j}{1 + \sum_{k=0}^{2} \sum_{l=0}^{2} B_{k,l} (\Delta - 100)^k (T_R)^l} \tag{9}$$

The fitting coefficients and associated errors are given in Table 6. Eq. 9 has an R^2 of 0.995 and a standard error of ± 6.2 bars. Because the data from Fall et al.[18] at 22°C were used to develop the CO_2 densimeter, Eq. 8 agrees with Fall et al.[18] within analytical error.

4. Discussion

4.1 Peak Position and Criticality

The variation in peak position with pressure and temperature is related to the relative density (volume) changes that occur during a change in *PT* conditions. This is exemplified in Fig. 3, as the isobars in temperature-peak position and temperature-density space show complementary trends. The largest changes in both density and peak position with temperature occur at the lowest temperatures shown, i.e., near the critical point, and the relative change in peak position and density as a function of temperature is muted at higher temperatures. However, as noted above, the isofreqs for N_2 reach a maximum pressure at some temperature and then decrease in pressure as temperature increases further. This reversal in the peak position trend with increasing pressure may be related to changes in the attractive and repulsive forces and is discussed further below. The largest relative density (volume) changes coincide with the largest relative peak position changes for each gas and occur in the vicinity of the critical point for that gas. This is expected because thermodynamic properties of fluids, such as heat capacity, isobaric thermal expansivity, and isothermal compressibility[53], show large (infinite) changes with changing P or T near the critical point[54].

The shape of the isotherms of each gas and magnitude of the peak shift along an isotherm in pressure-peak position space shown in Fig. 1 is systematically related to the proximity of the isotherm to the critical point. Reduced temperature (Eq. 3) serves as a convenient proxy for nearness to the critical temperature, with a reduced temperature of unity (T_r=1) corresponding to a temperature equal to the critical temperature. The low temperature isotherms show a larger shift in peak position with increasing pressure over the *PT* range studied, compared to the higher temperature isotherms, and have a more sigmoidal shape compared to the more linear high temperature isotherms (see Fig. 1). Note that the isotherms in Fig. 1 that are below the critical temperature are discontinuous where the isotherm crosses the L-V curve, and are thus not considered sigmoidal. The degree to which the isotherm is sigmoidal in pressure-peak position space depends on the reduced temperature of the gas, as small changes in pressure in the vicinity of the critical point result in large relative changes in density (volume). This can be seen clearly using the 35°C isotherms (solid black lines in Fig. 1a, b, and c) for CH_4, N_2, and CO_2. At 35°C, the T_R for CO_2, CH_4, and N_2 is 1.1, 1.6, and 2.4, respectively. The 35°C isotherm for CO_2 shows the most pronounced relative peak shift of the three gases at 35°C because it is closest to its critical temperature at 35°C and experiences the largest relative density (volume) change along the 35°C isotherm with increasing pressure. In contrast, N_2 shows the least pronounced relative peak shift of the three gases, partly due to the fact that at 35°C the gas is well above the critical temperature of N_2 (-147°C) and the relative density (volume) change with pressure is smaller than that of CO_2 at 35°C. CH_4 shows a behavior that is intermediate between that shown for CO_2 and N_2, consistent with the fact that the critical temperature of CH_4 (-83°C) is between those for CO_2 (31°C) and N_2 (-147°C).

4.2 Interpretation of Raman Spectra using Intermolecular Attraction and Repulsion

The variation in Raman peak position with pressure and temperature reflects interactions between molecules. As noted above, dominance of attractive forces leads to a shift in the Raman peak position to lower wavenumbers whereas dominance of repulsive forces leads to a shift in the Raman peak position to higher wavenumbers [21, 38-39]. The reason for this is that dominance of repulsive forces contracts the bond length slightly while dominance of attractive forces expands the bond length slightly[55]. Contraction of the bond strengthens the bond, requiring more energy to cause a vibration, while expansion of the bond weakens the bond, requiring less energy to cause a vibration[17]. The strength of the repulsive and attractive forces between molecules is dependent on the distance between molecules, with repulsive forces between molecules being most intense when the molecules are in close proximity to one another and attractive forces being experienced between molecules at longer intermolecular distances[40].

4.2.1 Isothermal Inflection Pressure

Pressure and temperature have opposing effects on the volume of the gas and the distance between molecules: increasing pressure decreases volume while increasing temperature increases volume. Attractive forces between molecules dominate at greater intermolecular distances than repulsive forces, so at low pressures and high temperatures where the molecules are spaced sufficiently far apart such that the repulsive forces between molecules are insignificant, a small decrease in volume is expected to yield an overall negative shift in Raman peak position. This overall negative shift in peak position can be seen in Fig. 1 and 2. As volume decreases further and repulsive forces between molecules increase, attractive and repulsive forces produce competing effects on the wavenumber shift. Additionally, the relative increase in the magnitude of the attractive forces decreases as the molecules are forced closer together, while the magnitude of the repulsive forces increases[40]. This implies that at a constant temperature and sufficiently high pressure (higher than the pressure range studied here for N_2, CO_2, and CH_4), the repulsive forces become dominant, and the peak position increases with increasing pressure along the isotherm. This phenomenon, in which the isothermal pressure dependence of peak position shows an inflection with increasing pressure, has been observed for N_2, CH_4, and H_2[15, 21]. The pressure of this inflection point at 22°C is ~1000 bars for CH_4 and ~1500 bars for N_2[15]. Note that these pressure inflection points are likely temperature dependent.

4.2.2 Isobaric Inflection Temperature

If the peak position increases along an isobar as temperature increases (see Fig. 1 and 3), repulsive forces between molecules are dominant. This behavior is potentially related to the increasing frequency of collisions brought about by increasing the kinetic energy of the molecules. However, increasing temperature at constant pressure will also increase the volume and thus intermolecular distance, which will weaken the effect of the repulsive forces while the attractive forces, which are experienced between molecules at larger intermolecular distance than repulsive forces, will not change much until the intermolecular distances are sufficiently large that the molecules do not interact at all and behave like an ideal gas. This implies that at a constant pressure and relatively high temperature, the repulsive forces would be sufficiently weakened such that attractive forces dominate and the peak position will shift to lower wavenumbers. Thus, in a manner similar to the isothermal pressure dependence of peak position, the isobaric temperature dependence of peak position also shows an inflection and change in trend with increasing temperature. This can be seen for N_2 in Figs. 1b and 3b, where the inflection occurs between 0 to 50°C (depending on the pressure) above ~50 bars and at much lower temperatures below ~50 bars. A potential explanation for the inflection occurring at much lower temperatures at pressures less than ~50 bars is that the molecules are spaced sufficiently far apart that only a small temperature increase is needed to reduce the repulsive interactions beyond the inflection point, resulting in the much lower inflection temperatures found for N_2 at pressures less than ~50 bars. While the inflection temperature was not reached for CH_4 and CO_2, the decreasing difference in peak position between isotherms separated by the same temperature increment in Fig 1a, c indicates that the inflection temperature is being approached, with CH_4

appearing to be closer to the inflection temperature than CO_2 at 350°C. This relative order of inflection temperatures in pressure-wavenumber space is further supported by the 450°C isotherm shown in Fig 2a (black line) for CH_4. The peak positions of CH_4 at densities above ~0.06 g/cm^3 at 450°C are at lower wavenumbers than the peak position of CH_4 at densities above ~0.06 g/cm^3 at 350°C. As can be seen from Fig. 2b relative to Fig. 1b, the inflection temperature for N_2 is located at a lower temperature in density-wavenumber space (isochoric inflection temperature) than pressure-wavenumber space (isobaric inflection temperature). Since CH_4 has reached the isochoric inflection temperature over the *PT* range studied while CO_2 has not, it is likely that CH_4 will also reach the isobaric inflection temperature before CO_2. The order in which the species reach this inflection temperature can be related to the Boyle temperature of the molecules, which is the temperature at which the attractive and repulsive forces are equivalent and of opposite sign such that they cancel out. The Boyle temperature defined at 0 pressure for N_2, CH_4, and CO_2 is ~50°C, ~240°C, and ~450°C, respectively[56]. The inflection temperatures do not occur exactly at the Boyle temperatures, however from the Boyle temperatures it would be expected that N_2, which has the lowest Boyle temperature, would have an inflection temperature lower than that of CH_4, which, in turn, would be located at a lower temperature than CO_2. The results shown in Fig. 1 are in good agreement with this interpretation.

4.3 Relationship between Isochores and Isofreqs for N_2, CH_4, and CO_2

Initially, starting from low pressures and temperatures, the effect of increasing pressure and temperature on the shift in peak position reflects competing effects of intermolecular interactions, similar to the manner in which increasing temperature and pressure have competing effects on the density. However, depending on the *PT* conditions at which the inflection points are reached, the effects of increasing temperature and pressure may no longer act against each other with regard to the shift in the peak position, but instead may act in the same direction, leading to the curvature of the isofreqs in Fig. 5. Note that the isofreqs in Fig. 5c are nearly linear due to the fact that CO_2 is well below both the isobaric inflection temperature and the isothermal inflection pressure in the *PT* range studied. Using the 0.35 g/cm^3 isochore in Fig. 5b (N_2) as an example, as temperature is increased along the isochore, the pressure must also increase to maintain a constant volume (density) because of the opposing effects of compressibility and thermal expansivity. The isochore by definition represents the locus of *P* and *T* along which these opposing effects are equal and thus cancel out to maintain constant density. The same *PT* relationship can be invoked for the 2328.2 cm^{-1} isofreq in Fig. 5b over the *PT* range up to ~-80°C and ~180 bars, where the isofreq remains roughly parallel to the 0.35 g/cm^3 isochore. As temperature is increased along the isofreq, pressure must also increase to maintain a constant peak position (wavenumber) because increasing temperature alone at conditions below the isobaric temperature inflection point results in an increase in the peak position (Fig. 3). Below the isothermal pressure inflection point, increasing pressure leads to a decrease in the peak position (Fig. 1b). Thus, similar to the case of density along the isochore, along the isofreq (below the inflection point of one of the variables), increasing *P* and *T* have equal and opposite effects on the peak position and cancel each other. However, unlike the isochores, the isofreqs must curve as the inflection point of one variable, either *P* or *T*, is reached such that the two effects become *complementary* instead of opposing. This results in the change in slope of the 2328.2 cm^{-1} isofreq in Fig. 5b from positive to negative at ~22°C, at which point the isofreq reaches the *T* inflection. Thus, to maintain the constant peak position as *T* increases above ~22°C, pressure must now *decrease* instead of increase.

5. Summary

Raman spectra were collected for the symmetric stretching peak of N_2, CO_2, and CH_4 from 10 to 500 bars and from temperatures slightly below the L-V curve to elevated temperatures. Volumetric changes and the resulting changes in intermolecular forces affect the magnitude and direction of Raman peak shifts of N_2, CH_4, and CO_2 over the *PT* range studied. The competing effects of attraction and repulsion between molecules are revealed through changes in peak position. Moreover, the volumetric changes and intermolecular interactions associated with these volumetric changes are correlated to proximity of the analytical conditions to the critical temperature which in turn gives rise to a systematic relationship between Raman peak positions of these fluids and criticality. The information gathered on the pure gases can be expanded in future work to gas mixtures containing N_2, CO_2, and CH_4.

Acknowledgements

The authors thank Charles Farley for assistance in the laboratory and Yury Klyukin and Lowell Moore for many helpful conversations on intermolecular forces and Kyle Ashley for helpful discussions of pressure and temperature dependence of Raman peaks and drift during Raman measurements. This material is based in part on work supported by the National Science

Foundation under grant numbers EAR-1624589 and OCE-1459433 to RJB. HML was supported by the PFF fellowship at the University of Missouri. MS-M was supported by a Discovery Grant from NSERC. RCB was supported by the Energy Resources Program of the U.S. Geological Survey. Use of trade, product, or firm names is for descriptive purposes only and does not imply endorsement by the U.S. Government.

References

[1] H. E. C. Swanenberg, *Geologica Ultraiectina* **1980**; *25*, 1.

[2] J. Touret, in *Short Course in Fluid Inclusions: Application to Petrology*, (Eds. L. S. Hollister, M. L. Crawford), Mineral association of Canada, Markham, **1981**, pp. 182-208.

[3] R. Kreulen, R. D. Schuiling, *Geochim. Cosmochim, Acta* **1982**; *46*, 193.

[4] A. M. Van den Kerkhof A. M., *Ph. D. thesis*, Univ. Amsterdam, **1988**.

[5] C. J. S. DeAlvarenga, M. Cathelineau, J. Dubessy, *Mineral. Mag.* **1990**; *54*, 245.

[6] P. D. Jenden, I. R. Kaplan, R. Poreda, H. Craig, *Geochim. Cosmochim. Acta* **1988**; *52*, 851.

[7] L. Palcsu, I. Vető, I. Futó, G. Vodila, L. Papp, Z. Major, *Marine Petrol. Geol.* **2014**; *54*, 216.

[8] E. L. Klein, C. Harris, C. Renac, A. Giret, C. A. V. Moura, K. Fuzikawa, *Miner. Depositia* **2006**; *41*, 160.

[9] E. Chicharro, M. Boiron, J. A. López-García, D. N. Bardfod, C. Villaseca, *Ore Geol. Rev.* **2016**; *72*, 896.

[10] H. B. Niemann, S. K. Atreya, S. J. Bauer, G. R. Carignan, J. E. Demick, R. L. Frost, D. Gautier, J. A. Haberman, D. N. Harpold, D. M. Hunten, G. Israel, J. I. Lunine, W. T. Kasprzak, T. C. Owen, M. Paulkovich, F. Raulin, E. Raaen, S. H. Way, *Nature* **2005**; *438*, 779.

[11] H. B. Niemann, S. K. Atreya, J. E. Demick, D. Gautier, J. A. Haberman, D. N. Harpold, W. T. Kasprzak, J. I. Lunine, T. C. Owen, F. Raulin, *J. Geophys. Res. E Planets* **2010**; *115*, 1.

[12] X. Zang, D. Liang, *J. Chem. Eng. Data* **2018**; *63*, 197.

[13] D. V. Petrov, *Spectrochim. Acta* **2018**; *191*, 576.

[14] D.A. Long, *The Raman Effect: A Unified Treatment of the Theory of Raman Scattering by Molecules,* John Wiley & Sons, Chichester, **2002**.

[15] D. Fabre, B. Oksengorn, *Appl. Spectrosc.* **1992**; *46*, 468.

[16] F. Lin, R. J. Bodnar, S. P. Becker, *Geochim. Cosmochim. Acta* **2007**; *71*, 3746.

[17] F. Lin, A. K. Sum, R. J. Bodnar, *J. Raman Spectrosc.* **2007**; *38*, 1510.

[18] A. Fall, B. Tattitch, R. J. Bodnar, *Geochim. Cosmochim. Acta* **2011**; *75*, 951.

[19] H. M. Lamadrid, M. Steele-MacInnis, R. J. Bodnar, *J. Raman. Spectrosc.* **2018**; *49*, 581.

[20] H. M. Lamadrid, L. R. Moore, D. Moncada, J. D. Rimstidt, R. C. Burruss, R. J. Bodnar, *Chem. Geol.* **2017**; *450*, 210.

[21] A. D. May, V. Degen, J. C. Stryland, H. L. Welsh, *Can. J. Phys.* **1961**; *39*, 1769.

[22] D. Fabre, R. Couty, *Comptes Rendus L Acad Des Sci Ser II* **1986**; *303*, 1305.

[23] R. Kroon, M. Baggen, A. Lagendijk, *J. Chem. Phys.* **1989**; *97*, 74.

[24] B. Lavorel, B. Oksengorn, D. Fabre, R. Saint-Loup, H. Berger, *Mol. Phys.* **1992**; *75*, 397.

[25] M. J. Clouter, H. Kiefte, *J. Chem. Phys.* **1977**; *66*, 1736.

[26] M. J. Clouter, H. Kiefte R. K. Jain, *J. Chem. Phys.* **1980**; *73*, 673.

[27] B. Oksengorn, D. Fabre, B. Lavorel, R. Saint-Loup, H. Berger, *J. Chem. Phys.* **1991**; *94*, 1774.

[28] R. D. Etters, J. Belak, R. LeSar, *Phys. Rev. B* **1986**; *34,* 4221.

[29] T. Dreier, G. Schiff, A. A. Suvernev, *J. Chem. Phys.* **1994**; *100*, 6275.

[30] G. S. Devendorf, D. Ben-Amotz, *J. Phys. Chem.* **1993**; *97*, 2307.

[31] J. C. Seitz, J. D. Pasteris, I-M. Chou, *Amer. J. Sci.* **1993**; *293*, 297.

[32] I-M. Chou, J. D. Pasteris, J. C. Seitz, *Geochim. Cosmochim. Acta* **1990**; *54*, 535.

[33] V. Thieu, S. Subramanian, S. O. Colgate, E. D. Sloan Jr, *Ann N Y Acad Sci* **2000**; *912*, 983.

[34] L. Shang, I-M. Chou, R. C. Burruss, R. Hu, X. Bi, *J. Raman Spectrosc.* **2014**; *45*, 696.

[35] W. Lu, I-M. Chou, R. C. Burruss, Y. Song, *Geochim. Cosmochim. Acta* **2007**; *71*, 3969.

[36] J. C. Seitz, J. D. Pasteris, I-M. Chou, *Amer. J. Sci.* **1996**; *296*, 577.

[37] S. Brunsgaard Hansen, R. W. Berg, E. H. Stenby, *Appl. Spectrosc.* **2001**; *55*, 745.

[38] W. Schindler, J. Jonas, *J. Chem. Phys.* **1980**; *73*, 3547.

[39] W. Schindler, P. T. Sharko, J. Jonas, *J. Chem. Phys.* **1982**; *76*, 3493.

[40] K. S. Schweizer, D. Chandler, *J. Chem. Phys.* **1982**; *76*, 2296.

[41] B. Lavorel, R. Chaux, R. Saint-Loup, H. Berger, *Opt. Commun.* **1987**; *62*, 25.

[42] S. C. Schmidt, D. S. Moore, M. S. Shaw, *Phys. Rev. B* **1987**; *35*, 493.

[43] E. Fermi, *Z. Phys.* **1931**; *71*, 250.

[44] K. M. Rosso, R. J. Bodnar, *Geochim. Cosmochim. Acta* **1995**; *59*, 3961.

[45] Y. Kawakami, J. Yamamoto, H. Kagi, *Appl. Spectrosc.* **2003**; *57*, 1333.

[46] J. Yamamoto, H. Kagi, *Chem. Lett.* **2006**; *35*, 610.

[47] X. Wang, I-M. Chou, W. Hu, R. C. Burruss, Q. Sun, Y. Song, *Geochim. Cosmochim. Acta* **2011**; *75*, 4080.

[48] I-M. Chou, R. C. Burruss, W. Lu, *Adv. High-Pressure Technol. Geophys. Appl.* **2005**; 475-485.

[49] E.W. Lemmon, I. H. Bell, M.L. Huber, M.O. McLinden, *NIST Standard Reference Database 23: Reference Fluid Thermodynamic and Transport Properties-REFPROP, Version 10.0*, National Institute of Standards and Technology, Standard Reference Data Program, Gaithersburg, **2018**.

[50] U. Setzmann, W. Wagner, *J. Phys. Chem.* **1991**; *20*, 1061.

[51] R. Span, E. W. Lemmon, R. T. Jacobsen, W. Wagner, A. Yokozeki, *J. Phys. Chem.* **2000**; *29*, 1361.

[52] R. Span, W. Wagner, *J. Phys. Chem. Ref. Data* **1996**; *25*, 1509.

[53] J. V. Sengers, J. M. H. Levelt Sengers, *Ann. Rev. Phys. Chem.* **1986**; *37*, 189.

[54] J. W. Johnson, D. Norton, *Am. J. Sci.* **1991**; *291*, 541.

[55] M. R. Zakin, D. R. Herschbach, *J. Chem. Phys.* **1986**; *85*, 2376.

[56] R. Estrada-Torres, G. A. Iglesias-Silva, M. Ramos-Estrada, K. R. Hall, *Fluid Phase Equilibria* **2007**; *258*, 148.

Figures

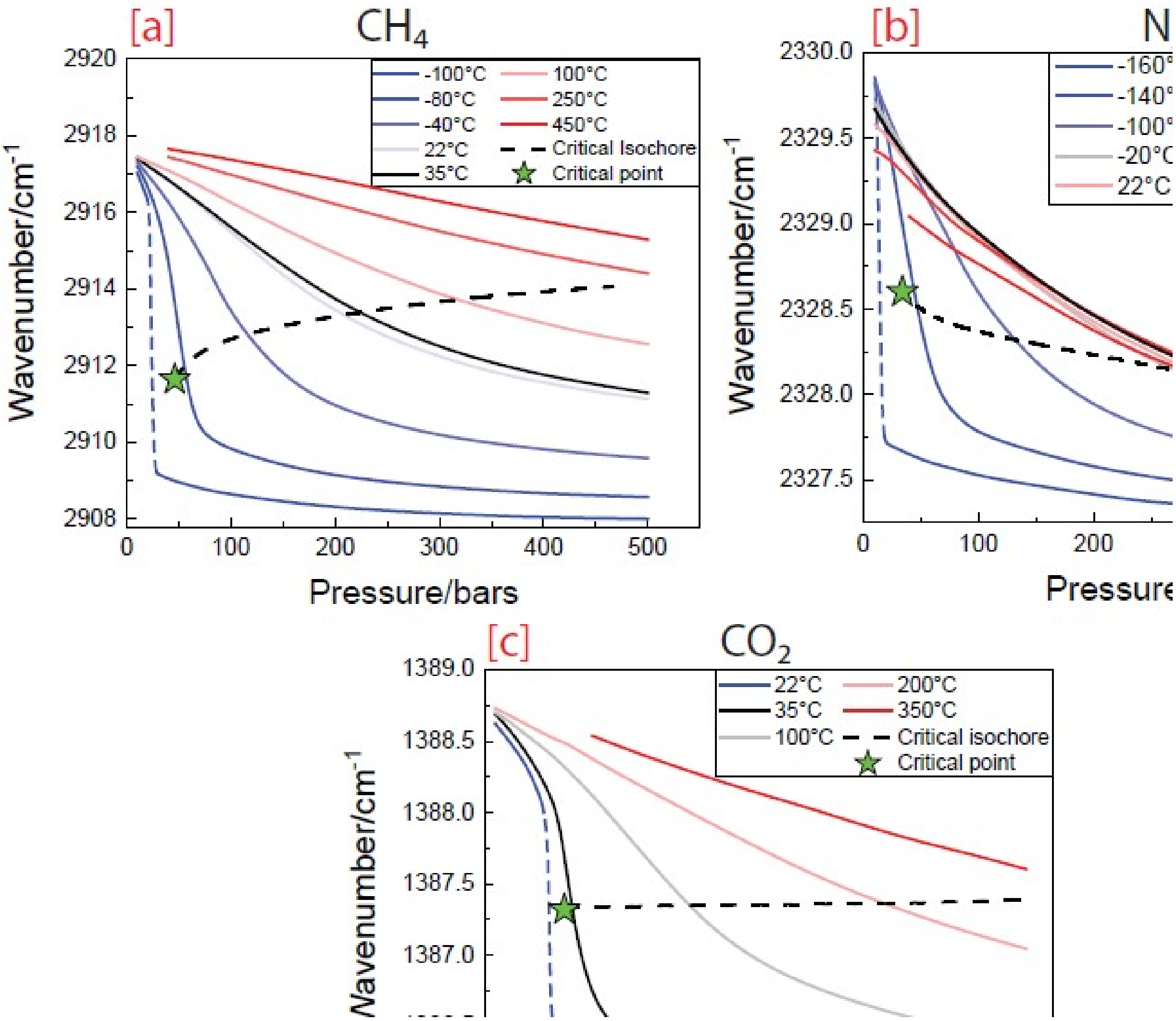

Fig. 1. Plots of the peak position of CH_4 (a), N_2 (b), and CO_2 (c) versus pressure over the temperature ranges studied. The green star represents the critical point for each species, while the black dashed line represents the critical isochore. The dashed portion of the lowest temperature isotherm for each species represents the discontinuity in peak position as the L-V curve is intersected by the isotherm.

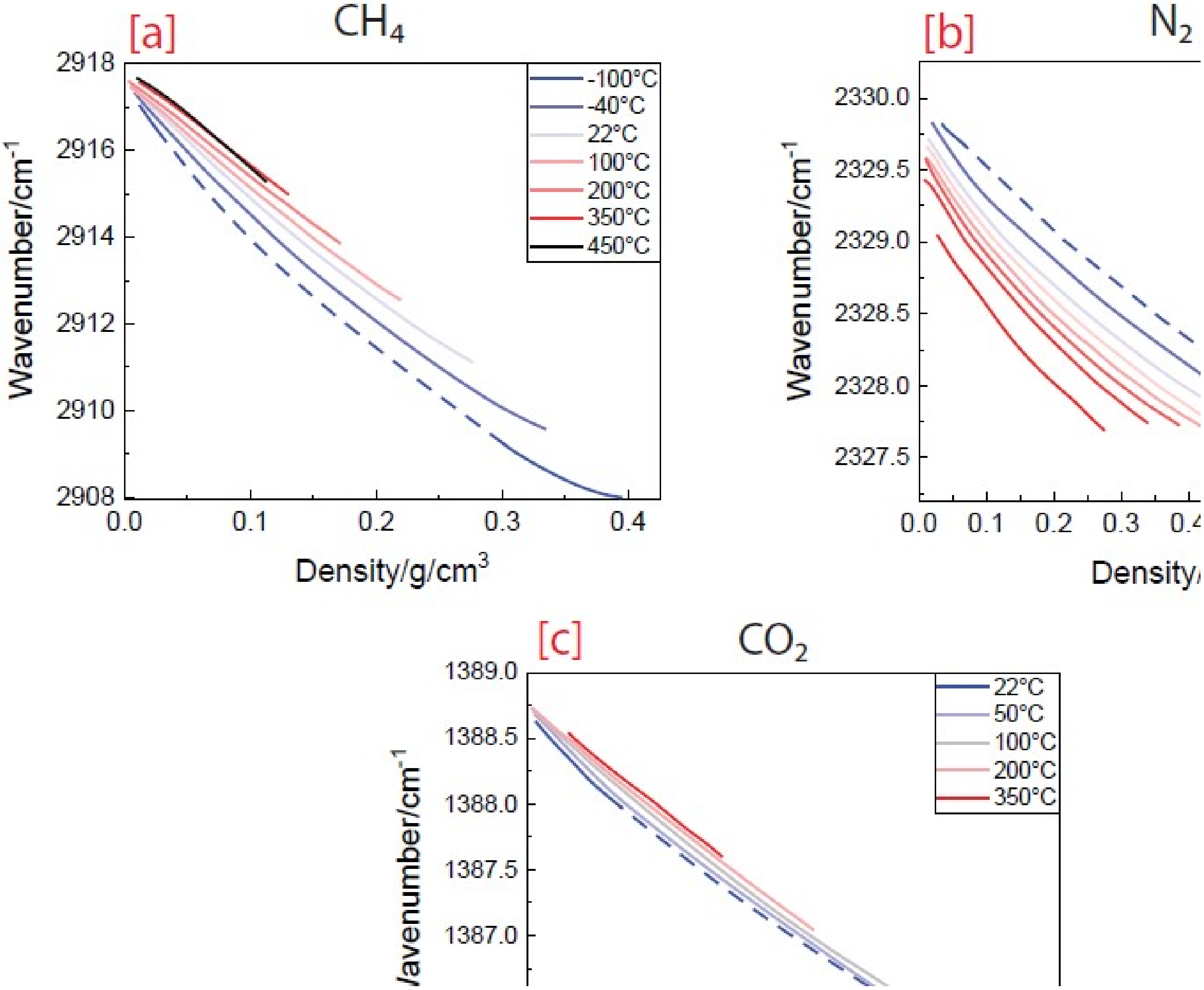

Fig. 2. Plots of the peak position of CH_4 (a), N_2 (b), and CO_2 (c) versus density over the temperature ranges studied. Densities were calculated using the NIST REFPROP version 10.0 program[49] and the Setzman and Wagner[50], Span et al.[51], and Span and Wagner[52] equations of state for CH_4, N_2, and CO_2, respectively. The dashed portion of the lowest temperature isotherm for each species represents the discontinuity in peak position as the L-V curve is intersected by the isotherm.

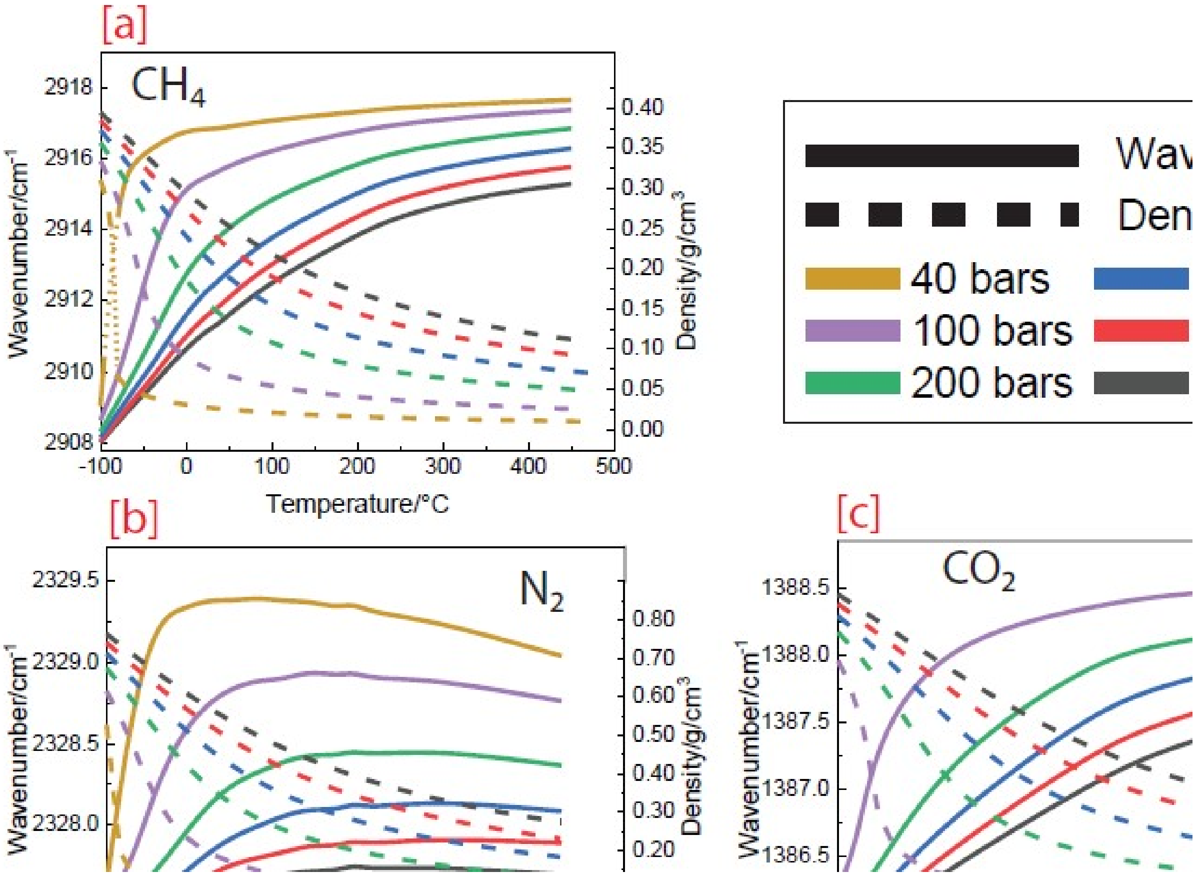

Fig. 3. Plot of the peak position (solid lines) and the density (dashed lines) of CH_4 (a), N_2 (b), and CO_2 (c) versus temperature for several isobars. The dotted portion of the 40 bar isobars in (a) indicate the discontinuity in peak position and density as the L-V curve was intersected by the isobars between -100°C and -80°C. Densities were calculated using the NIST REFPROP version 10.0 program[49] and the Setzman and Wagner[50], Span et al.[51], and Span and Wagner[52] equations of state for CH_4, N_2, and CO_2, respectively.

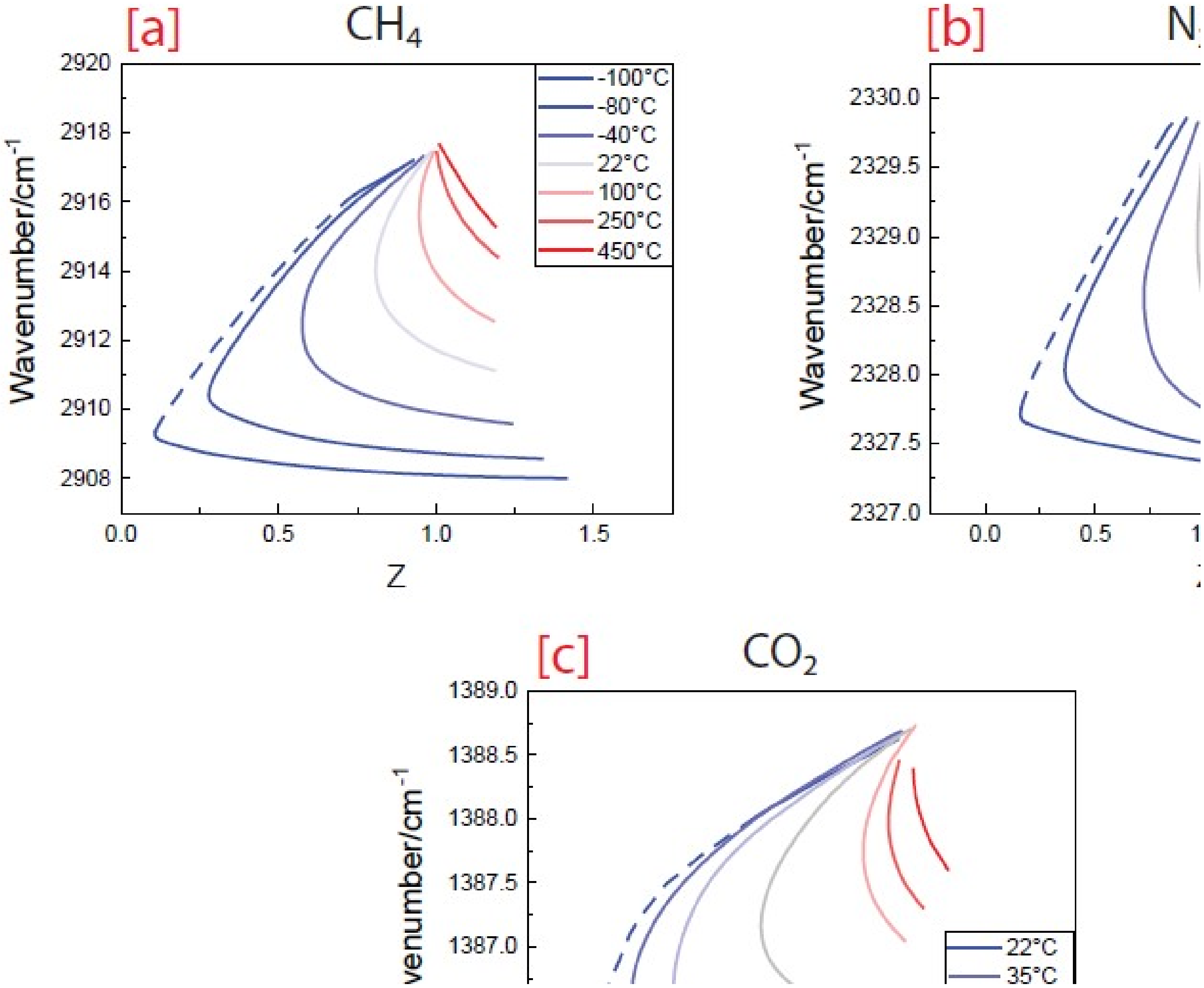

Fig. 4. Plots of the peak position of CH_4 (a), N_2 (b), and CO_2 (c) versus compressibility factor (Z) over the temperature ranges studied. The dashed portion of the lowest temperature isotherm for each species represents the discontinuity in peak position as the L-V curve is intersected by the isotherm.

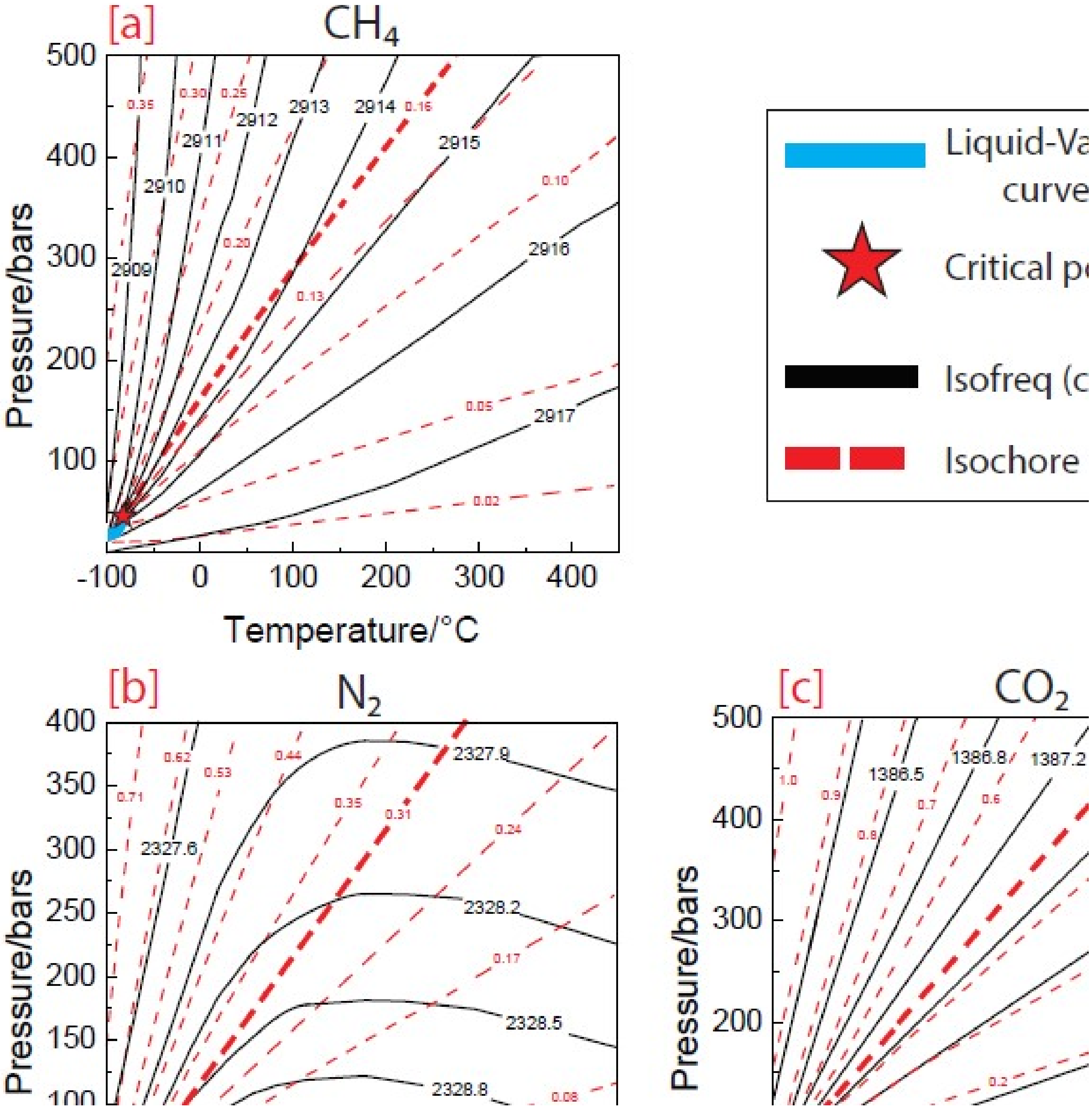

Fig. 5. Plot of pressure versus temperature for CH_4 (a), N_2 (b), and CO_2 (c). Solid black lines are lines of constant peak position (isofreqs). Red dashed lines are lines of constant density (isochores). The bolded red dashed line in each figure represents the critical isochore. The star symbol represents the critical point of each system and the solid blue line represents the L-V curve.

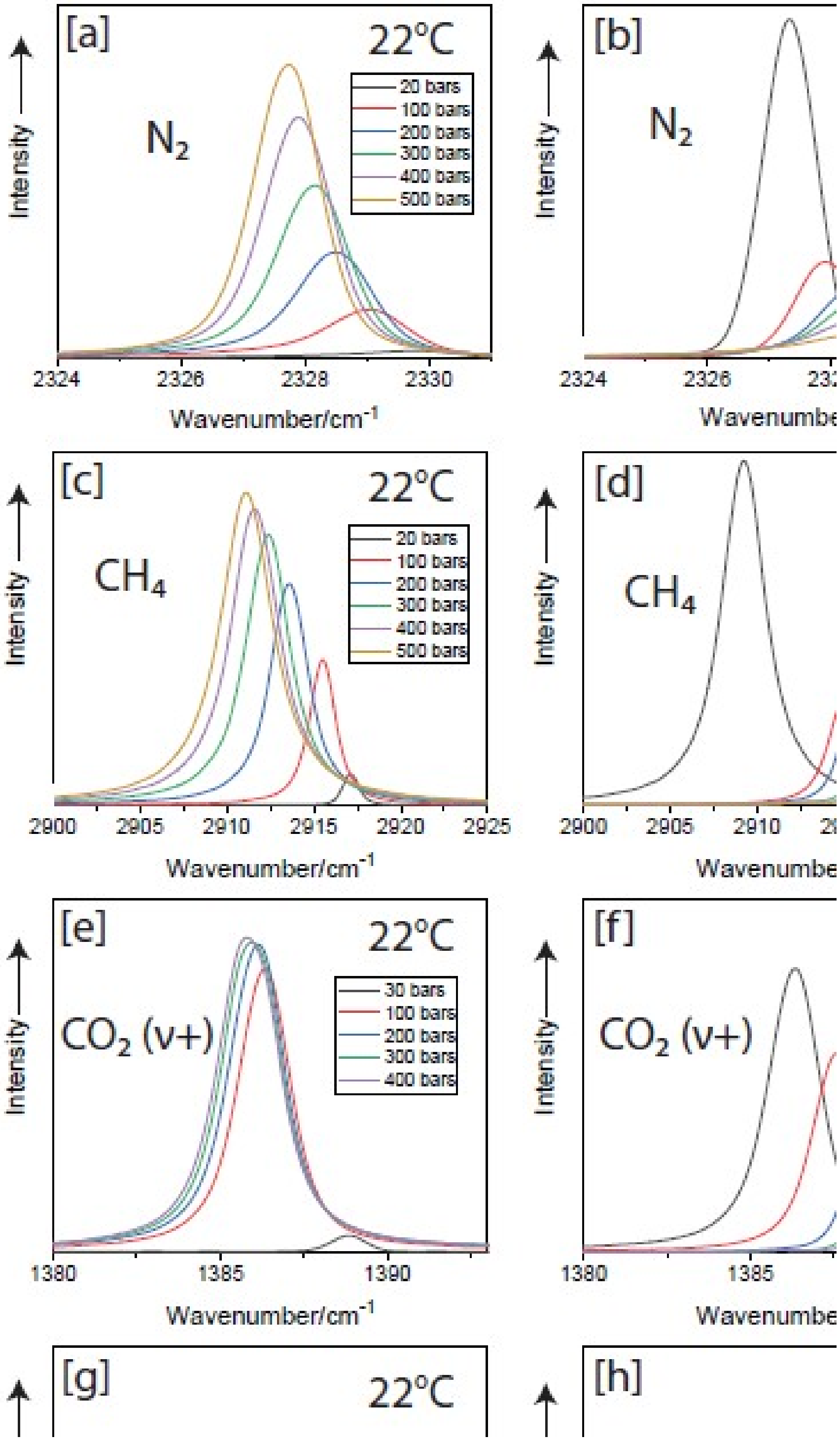

Fig. S1. Plots of relative intensity versus peak position for N_2 (a,b), CH_4 (c,d), and CO_2 (e-h). (a), (c), (e), and (g) are at constant temperature and changing pressure and (b), (d), (f), and (h) are at constant pressure and changing temperature.

Tables

Table 1: Fitting coefficients for the CH_4 densimeter (Eq. 4).

$A_{i,j}$	Value	Error (±)
0,0	-0.01317	0.00435
1,0	0.03021	0.00389
2,0	-0.0046	7.78×10^{-4}
0,1	-0.01897	0.00140
0,2	0.00161	1.03×10^{-4}
1,1	-0.00867	5.60×10^{-4}

Table 2: Fitting coefficients for the CH_4 barometer (Eq. 5).

$A_{i,j}$	Value	Error (±)
0,0	41.24	9.04
1,0	77.11	2.29
0,1	-47.09	9.04
0,2	25.00	1.96
1,1	-82.47	2.19
$B_{k,l}$	**Value**	**Error (±)**
1,0	-0.31255	0.00539
2,0	-0.03746	7.04×10^{-4}
0,1	-0.1796	0.0272
0,2	0.07054	0.00607
1,1	0.08383	0.00265

Table 3: Fitting coefficients for the N_2 densimeter (Eq. 6).

$A_{i,j}$	Value	Error (±)
0,0	2.0719	0.0136
1,0	-0.25827	0.00494
2,0	0.00638	8.39×10^{-4}
0,1	-1.6203	0.0221
0,2	0.30296	0.00779
1,1	0.10800	0.00254

Table 4: Fitting coefficients for the N_2 barometer (Eq. 7).

$A_{i,j}$	Value	Error (±)
0,0	-5.930	0.404
1,0	6.042	0.871
0,1	8.749	0.406
0,2	-0.9672	0.0769
1,1	-8.429	0.760
$B_{k,l}$	**Value**	**Error (±)**
1,0	6.037	0.106
2,0	3.989	0.363
0,2	0.1307	0.0198
1,1	-1.5546	0.0380

Table 5: Fitting coefficients for the CO_2 densimeter (Eq. 8).

$A_{i,j}$	Value	Error (±)
0,0	-1.1429	0.0940
1,0	-0.3144	0.0436
0,1	0.4461	0.0425
0,2	-0.02296	0.00392
1,1	0.1529	0.0144

Table 6: Fitting coefficients for the CO_2 barometer (Eq. 9).

$A_{i,j}$	Value	Error (±)
0,0	3090	1250
1,0	-1019	420
0,1	-3420	1380
0,2	161.7	70.3
1,1	1108	456
$B_{k,l}$	**Value**	**Error (±)**
1,0	2.685	0.941
2,0	-0.430	0.144
0,1	-3.683	0.882
0,2	0.909	0.217

Chapter 3: Raman spectral behavior of N_2, CO_2, and CH_4 in N_2-CO_2-CH_4 gas mixtures from 22-200°C and 10-500 bars

Abstract

The Raman spectral behavior of N_2, CO_2, and CH_4 in ternary N_2-CO_2-CH_4 mixtures was studied from 22-200°C and 10-500 bars. The peak position of N_2 in all mixtures is located at lower wavenumbers compared to pure N_2 at the same *PT* conditions. The Fermi diad splitting in CO_2 was larger in the pure system than in the mixtures, and the Fermi diad splitting became larger in the mixtures as CO_2 concentration increased at constant *PT*. The peak position of CH_4 in the mixtures is shifted to higher wavenumbers compared to pure CH_4 at the same *PT* conditions. However, the relationship between peak position and CH_4 mole fraction is more complicated, compared to the trends observed with N_2 and CO_2. The relative order of the peak position isotherms of CH_4 and N_2 in the mixtures in pressure-peak position space mimics trends in the molar volume of the mixtures in pressure-molar volume space. Relationships between the direction of peak shift of components in the mixtures, the relative molar volumes of the mixtures, and attraction and repulsion experienced between molecules are developed. In the region in which the peak shift is dominated by attractive interactions between molecules, the peak position of a component in the mixture with the larger molar volume occurs at higher wavenumbers relative to the peak position of that component in mixtures having smaller molar volumes. In the region in which the peak shift is dominated by repulsive interactions between molecules, the peak position of a component in the mixture with the larger molar volume occurs at lower wavenumbers relative to that component in mixtures with smaller molar volumes. Based on these observations, a gas mixture barometer was developed that requires only measurement of the N_2 peak position in the mixture.

1. Introduction

Gas mixtures containing significant amounts of N_2, CO_2, and/or CH_4 occur naturally in many geologic environments[1-14]. Fluid inclusions formed in these environments trap and preserve samples of the fluids, and these may be analyzed to determine compositions and *PVT* properties of the fluids present at elevated *PT* conditions. Raman spectroscopy is an important technique often employed to characterize the *in situ* pressure-volume-temperature-composition (*PVTX*) properties of these natural fluids, and as such, many studies have been conducted on the Raman spectral properties of both the pure systems of N_2, CO_2, and CH_4, as well as mixtures of these gases to aid in the quantification of the spectral data obtained from natural samples[4, 15-42]. The vibrational modes typically of interest in the N_2-CO_2-CH_4 system are the vibrational modes that represent the symmetric stretching ("breathing") of the molecules. At 1 bar, the symmetric stretching vibrational mode of N_2 and CH_4 are nominally located at 2331 and 2917 cm^{-1}, respectively[4, 36]. For CO_2, the two peaks nominally located at 1285 and 1388 cm^{-1} at 1 bar that comprise the Fermi diad are of interest[4, 38]. The nominal peak positions for N_2 and CH_4 in pure systems shift to lower wavenumbers with increasing pressure or fluid density[17-20, 22, 33]. For pure CO_2, both peaks of the Fermi diad shift to lower wavenumbers with increasing pressure as well, however the individual peaks do not shift by the same amount as pressure increases and, therefore, the distance between the two peaks increases with increasing pressure or fluid density [19, 21-22, 34]. In gas mixtures consisting of N_2-CH_4, N_2-CO_2, and N_2-CO_2-CH_4 at temperatures near 22°C, the N_2 peak position was found to occur at lower wavenumbers at a given pressure relative to the N_2 peak position at the same pressure for the pure N_2 system[16, 20, 29-31]. Conversely, in gas mixtures consisting of N_2-CH_4, CH_4-H_2, CH_4-Ar, CH_4-CO_2, and N_2-CO_2-CH_4 at ~22°C, the CH_4 peak position was found to occur at higher wavenumbers at a given pressure relative to the CH_4 peak position at the same pressure for the pure CH4 system[16, 20, 29-30]. In a N_2-CO_2-CH_4 gas mixture at 22°C, the Fermi diad splitting was found to be larger in the pure system relative to the mixture at the same pressure[20].

Changes in the Raman spectral behavior of a gas may be related to the changes in the nature of interactions between molecules[18, 20, 43-48]. The molecular vibrational frequency of a given molecule is affected by the intermolecular forces of attraction and repulsion experienced by the molecule, and the change in molecular vibrational frequency associated with changing intermolecular interactions over a given *PT* range is reflected in the change in the Raman peak positions through a shift to higher or lower wavenumbers depending on which intermolecular force is dominant over a change in *PT* conditions[43-48]. If attraction between molecules dominates over repulsion over some range of *PT* conditions, the Raman peak position shifts to lower wavenumbers as *PT* conditions change[18, 43, 45-46]. If repulsion (collisions) between molecules dominates, the Raman peak position shifts to higher wavenumbers as *PT* conditions change[18, 43, 45-46].

Lamadrid et al.[20] recently demonstrated that the peak positions of N_2, CO_2, and CH_4 in a 70/15/15 mol% N_2/CO_2/CH_4 gas mixture differed significantly from the peak positions of pure N_2, CO_2, and CH_4 at the same *PT* conditions. The authors related the differences between the spectral behavior of the components in the pure systems and the mixture to the nonideal behavior (fugacity) of the gas mixture. Here, we further explore the relationship of peak position of N_2, CO_2, and CH_4 in gas mixtures with pressure, temperature, molar volume, and fugacity. These relationships are extended to gas mixtures outside the ternary N_2-CO_2-CH_4 system to determine if relationships between Raman peak position and pressure, temperature, molar volume, and fugacity are composition specific or if the behavior is consistent among multiple gas mixtures and compositions. Finally, we present a barometer for the N_2-CO_2-CH_4 system that is based on the Raman peak position of N_2 and propose that the barometer may be applicable to other systems in which N_2 behaves in a manner that is similar to that in ternary N_2-CO_2-CH_4 gas mixtures.

2. Methods

Raman peak positions for ternary gas mixtures containing 70/15/15 mol%, 25/25/50 mol%, 15/60/25 mol%, and 34/33/33 mol% N_2/CO_2/CH_4 (i.e. N_2-rich, CH_4-rich, CO_2-rich, and an equimolar gas mixture) were collected over the range 22-200°C and 10-500 bars using the methods described in detail by Sublett et al.[22] and outlined here. The compositions were chosen to monitor the behavior of the components in gas mixtures in which the concentrations of each of the three components varied from being the most abundant to the least abundant component in the mixture. Gas mixtures were commercially prepared by Airgas. Raman spectra were collected using a JY Horiba LabRam HR (800 mm spectrometer) Raman microprobe using a slit width of 150 μm, a confocal aperture of 400 μm, an 1800 grooves/mm grating, a 40x microscope objective (N.A. = 0.55), and excitation provided by a 514 nm (green) Laser Physics 100S-514 Ar^+ laser. Temperature and pressure were controlled using a Linkam CAP500 capillary heating and cooling stage connected to a high-pressure optical capillary system[42]. Two manual screw-type pressure generators (HiP model 37-6-30) were used to generate and control the pressure in the capillary system. The gas mixtures were analyzed through a transparent 20 cm long square cross-section (flat-sided) flexible fused silica capillary tube with an outer diameter of ~363 μm and an inner diameter of ~100 μm. A Precise Instruments pressure transducer (Model 645) was used to monitor pressure with an error of ±0.1% of the total output pressure. The system was allowed to equilibrate for one minute after a change in pressure. Temperature was monitored using an internal thermocouple within the Linkam CAP500 stage. The error in the temperature measurement was ±0.4% of the total output temperature. The system was allowed to equilibrate for 10 minutes after a change in temperature such that the temperature remained constant. The thermal gradient along the 5 cm portion of the transparent fused silica capillary tube that was located within the Linkam CAP500 stage was reported by Linkam to be no more than ±0.2% of the total output temperature. Raman measurements were made in the center of this 5 cm portion of heated capillary.

The symmetric stretching modes of N_2 and CH_4, along with the Fermi diad for CO_2 were recorded in this study. Peak positions for each gas component in each mixture were collected in separate collection windows using collections times that varied based on the temperature, pressure, and the component being measured. As such, collection times for individual gas components varied, with CO_2 requiring the longest collection times (~300s at 10 bars and 22°C in the 70/15/15 mol% $N_2/CO_2/CH_4$ mixture), CH_4 requiring the shortest (~40s at 10 bars and 22°C in the 70/15/15 mol% mixture), and all collection times decreasing with increasing pressure, decreasing temperature, and increasing abundance of a particular component. The collection times were chosen to conform to a standard that the peak of interest had to be represented by (1) at least four data points above background noise and (2) a peak intensity-to-full-width at half-maximum (FWHM) ratio for each peak of at least 500 counts/cm^{-1}, though in most cases this ratio was greater than 1200 counts/cm^{-1}. Due to the collection criteria used here, some *PTX* combinations were excluded from the data set as they did not meet the collection criteria. These *PTX* conditions included low pressure-high temperature *PT* combinations for the least concentrated component in mixtures. For example, N_2 peak positions collected at 10 bars and 200°C in the 15/60/25 mol% $N_2/CO_2/CH_4$ mixture are excluded as the spectral data did not meet either collection criterion.

Three accumulations were collected for each component in each gas mixture at each *PT* condition, and the analysis was repeated three times to produce three data points at each *PT* point, the average of which are given in the Appendix and are used in all subsequent discussions below. The average variation in the Raman peak positions of N_2 and CH_4, and the average variation in the Fermi diad of CO_2 in each gas mixture was ±0.03, ±0.03, and ±0.04 cm^{-1}, respectively, for the 70/15/15 mol% gas mixture, ±0.01, ±0.01, and ±0.01 cm^{-1}, respectively, for the 10/60/25 mol% gas mixture, ±0.02, ±0.02, and ±0.02 cm^{-1}, respectively, for the 25/25/50 mol% gas mixture, and ±0.02, ±0.02, and ±0.02 cm^{-1}, respectively, for the 34/33/33 mol% gas mixture. Peak positions were corrected using bounding Ne lines (N_2: 2253.58 and 2433.93cm^{-1}; CO_2: 1031.42 and 1458.58 cm^{-1}; CH_4: 2851.49 and 2972.55 cm^{-1}) following the method of Lin et al.[17] that were collected simultaneously with each gas analysis. It has been shown that the measured peak position of a gas varies between instruments and analytical sessions[21, 34]. To maintain internal consistency within the data set collected in this study, a standard peak position measurement at 120 bars (N_2 and CH_4) or 40 bars (CO_2) at 22°C was collected for each pure gas at the beginning and end of each data collection session and compared to the pure gas calibration curves for N_2[22], CH_4[17], and CO_2[19] at the pressures at which the standards were analyzed. The difference between the measured peak position of the standard and the calibration curves of each pure gas was used to correct the Ne-corrected peak positions measured for each component in each gas mixture during the analytical session.

3. Results

Isothermal pressure traverses for all gas mixtures at all *PT* conditions examined remained a single-phase fluid and, as a result, peak position varied in a continuous manner along the pressure traverse. If Raman analyses are conducted on a pure gas at temperatures below the critical temperature for the pure gas, a discontinuity exists in the peak position versus pressure trend in the vicinity of the phase boundary[19, 21-22, 34]. Thus, using a Raman peak position barometer developed for a pure gas at *PT* conditions that cross a phase boundary to estimate the pressure of a mixture that does not cross a phase boundary along the same *PT* traverse results in a constant value for pressure for measured peak positions that are within the two phase field of the pure gas, even though the pressure of the mixture is continuously changing. The pure gas barometers presented by Sublett et al.[22] take into account the critical temperature (T_C) of the gas which, in turn, can be used to account for the fact that the maximum temperature at which immiscibility can occur varies with fluid composition. When this barometer is used for a mixture that does not cross a phase boundary, the pressure will vary continuously as the peak position varies continuously because the mixture is above its critical temperature and this is accounted for in the barometer (Fig. 1). For the example shown in Fig. 1, some measured Fermi diad splittings recorded for CO_2 in the 15/60/25 mol% $N_2/CO_2/CH_4$ mixture at 22°C fall between the values for CO_2 vapor (103.2 cm^{-1})[19] and CO_2 liquid (104.5 cm^{-1})[19] for pure CO_2 at 22°C. Using a pure CO_2 barometer, such as that of Fall et al.[19], that does not take into account the critical temperature of the gas predicts the same pressure (~60.1 bars) for all Fermi diad splitting values between 103.2 and 104.5 cm^{-1} (to the right of the dashed line in Fig. 1), while using the pure CO_2 barometer that takes into account the critical temperature of the gas provides a continuous change in pressure for the gas mixture. The barometer developed by Sublett et al.[22] for CO_2 was used in this study because some of the Fermi diad splitting values of CO_2 in the gas mixtures at 22°C, including the example given in Fig. 1, fall within the range between 103.2 and 104.5 cm^{-1} that results in the discontinuity described above. To maintain internal consistency, the barometers for N_2 and CH_4 given by Sublett et al.[22] were also used. Note that for the 70/15/15 mol% $N_2/CO_2/CH_4$ gas mixture, the critical temperature is not known and was estimated using a model titration experiment with the NIST REFPROP version 10.0 program[49] and the GERG2008 EOS[50] adding N_2 to a gas mixture with a constant 1:1 ratio of CH_4:CO_2 and then extrapolating the nearly linear critical temperatures to 70 mol% N_2. Only the changes in Raman peak position are discussed below, however the change in the shape and intensity of the Raman peaks for N_2, CH_4, and both the more and less intense peaks of the Fermi diad for CO_2 from 100-500 bars at 22°C and 22-200°C at 300 bars is shown in the supplementary Figs. S1, S2, S3, and S4 for the 70/15/15 mol%, 34/33/33 mol%, 25/25/50 mol%, and 15/60/25 mol% $N_2/CO_2/CH_4$ mixtures, respectively.

3.1 N_2

Fig. 2a-c show the change in Raman peak position of N_2 in the pure system[22], and in the 70/15/15 mol% (22°C data from Lamadrid et al.[20]), 25/25/50 mol%, 15/60/25 mol%, and 34/33/33 mol% $N_2/CO_2/CH_4$ gas mixtures as a function of pressure at 22°C (a), 100°C (b), and 200°C (c). The Raman peak position of N_2 decreases with increasing pressure at constant temperature over the *PT* range studied for each composition. For most *PTX* conditions examined, the peak position of N_2 in the gas mixture is located at lower wavenumbers relative to the peak position of N_2 in the pure system at the same *PT* condition. At 22°C (Fig. 2a), the Raman peak position of N_2 decreases at constant pressure and decreasing total concentration of N_2, though the peak positions of N_2 in the 25/25/50 mol% and 34/33/33 mol% N_2/CO_2/CH_4 gas mixtures are similar. This general trend continues at higher temperatures, however the peak position of N_2 in the 15/60/25 mol% N_2/CO_2/CH_4 gas mixture at 200°C is located at higher wavenumbers compared to the peak position of N_2 in the 25/25/50 and 34/33/33 mol% N_2/CO_2/CH_4 gas mixtures at the same pressure over most of the pressure range examined. This behavior may reflect the fact that the critical temperature of this gas mixture (-11°C calculated using the NIST REFPROP version 10.0 program[49] and the GERG2008 EOS[50]) is closest (compared to the other mixtures) to the analytical temperature over the temperature range studied. Sublett et al.[22] showed that the pure gases experienced the largest increase in peak position with increasing temperature at temperatures near the critical temperature. The 25/25/50 and 34/33/33 mol% N_2/CO_2/CH_4 gas mixtures have similar critical temperatures (-66.7°C[49-50] and -66.9°C[49-50], respectively) and, because the 15/60/25 mol% N_2/CO_2/CH_4 mixture is ~50°C closer to its critical temperature, peak positions of the components in this mixture should migrate to higher wavenumbers at a faster rate with increasing temperature relative to the other mixtures and potentially occur at higher wavenumbers than the peak positions of the components in the 25/25/50 and 34/33/33 mol% N_2/CO_2/CH_4 gas mixtures at higher temperatures, based on the behavior observed for the pure gases. The peak position of N_2 in the N_2 poor mixtures (25/25/50 mol% and 15/60/25 mol% N_2/CO_2/CH_4), and in the equimolar mixture (34/33/33 mol% N_2/CO_2/CH_4) generally increases as temperature is increased at constant pressure. However, for the N_2-rich mixture (70/15/15 mol% N_2/CO_2/CH_4), the peak position of N_2 increases only slightly as temperature increases from 22°C to 100°C, and then remains roughly the same or decreases slightly as temperature increases from 100°C to 200°C at constant pressure. This behavior is also observed in the pure N_2 system and has been attributed to N_2 reaching an isobaric inflection temperature in which the trend of increasing peak position with increasing temperature at constant pressure reverses[22]. As the 70/15/15 mol% N_2/CO_2/CH_4 composition is dominated by N_2, it is expected to behave in a manner similar to that of pure N_2, relative to the other mixtures, and is likely the gas mixture whose composition results in an isobaric inflection temperature that is close to, or within the analytical temperature range over the pressure range studied.

Fig. 3a-c show the partial pressure of N_2 in the gas mixture versus the pure gas equivalent Raman pressure of N_2 ($P_{N_2}^{PGER}$), determined using the barometer developed by Sublett et al.[22] for pure N_2 and the peak position of N_2 in the mixtures at 22°C (a), 100°C (b), and 200°C (c). The partial pressure of a gas in a mixture is given by:

$$P_i = X_i * P \tag{1}$$

where P_i is the partial pressure of component i, P is the total pressure of the system, and X_i is the mole fraction of component i. The solid lines in Fig. 3a-c represent the points along the 22°C, 100°C and 200°C isotherms, respectively, at which the partial pressure of N_2 determined from Eq. 1 using the measured total pressure of the system and the known composition of the gas mixture, and the pressure determined from the measured peak position and interpreted using the equation for the pure gas ($P_{N_2}^{PGER}$) from Sublett et al.[22], are equivalent.

At all *PTX* conditions, $P_{N_2}^{PGER}$ is greater than the partial pressure of N_2 calculated by Eq. 1. This has been observed in other studies of gas mixtures as well[16, 20, 29-30]. As can be seen in Fig. 3a-c, the $P_{N_2}^{PGER}$ of the most N_2-rich mixture (70/15/15 mol% $N_2/CO_2/CH_4$) most closely equals the partial pressure of N_2 in the mixture, with the difference between the partial pressure of N_2 and $P_{N_2}^{PGER}$ increasing as the proportion of N_2 in the mixture decreases for all temperatures measured in this study. The difference between the partial pressure and $P_{N_2}^{PGER}$ for a given composition decreases as temperature increases.

3.2 CO_2

Fig. 2d-f show the change in the splitting of the Fermi diad of CO_2 in the pure system[19,22], the 70/15/15 mol% (22°C data from Lamadrid et al.[21]), 25/25/50 mol%, 15/60/25 mol%, and 34/33/33 mol% $N_2/CO_2/CH_4$ gas mixtures as a function of pressure at 22°C (d), 100°C (e), and 200°C (f). At all *PTX* conditions, the Fermi diad splitting of CO_2 is greater in the pure system than in the gas mixtures. It should be noted that, as discussed above, at 22°C the liquid-vapor (L-V) curve of pure CO_2 is intersected at 60.1 bars, resulting in a discontinuity in the Fermi diad splitting at 60.1 bars and 22°C observed in Fig. 2d. The Fermi diad splitting of CO_2 increases with increasing pressure at constant temperature over the *PT* range studied for each composition. At all temperatures, the Fermi diad splitting of CO_2 decreases at constant pressure with decreasing concentration of CO_2 in the mixture. Additionally, the Fermi diad splitting of CO_2

decreases with increasing temperature at constant pressure and composition over the entire *PTX* range studied.

Fig. 3d-f show the partial pressure of CO_2 in a given gas mixture (Eq. 1) versus $P_{CO_2}^{PGER}$ determined using measured Fermi diad splitting of CO_2 in the mixtures at 22°C (d), 100°C (e), and 200°C (f), interpreted using the barometer of Sublett et al.[22] for pure CO_2. The solid lines in Fig. 3d-f represent the points along the 22°C, 100°C and 200°C isotherms, respectively, at which the partial pressure of CO_2 determined from Eq. 1 using the measured total pressure of the system and the known composition of the gas mixture, and the pressure determined from the measured peak position and interpreted using the equation for the pure gas $(P_{CO_2}^{PGER})$ from Sublett et al.[22], are equivalent. At all *PTX* conditions except for the 15/60/25 mol% $N_2/CO_2/CH_4$ mixture at 22°C and pressures above ~250 bars total pressure (partial pressure ≥ ~150 bars), $P_{CO_2}^{PGER}$ is greater than the partial pressure of CO_2. The $P_{CO_2}^{PGER}$ shows the best agreement with the partial pressure of CO_2 in the most CO_2-rich mixture (15/60/25 mol% $N_2/CO_2/CH_4$), with the difference between the partial pressure and $P_{CO_2}^{PGER}$ increasing as the concentration of CO_2 in the mixture decreases. However, unlike the trends observed in N_2, increasing temperature do not bring $P_{CO_2}^{PGER}$ and the partial pressure of CO_2 into closer agreement.

3.3 CH_4

Fig. 2g-i show the change in Raman peak position of CH_4 in the pure system[17, 22], and in the 70/15/15 mol% (22°C data from Lamadrid et al.[22]), 25/25/50 mol%, 15/60/25 mol%, and 34/33/33 mol% $N_2/CO_2/CH_4$ gas mixtures as a function of pressure at 22°C (g), 100°C (h), and 200°C (i). The Raman peak position of CH_4 decreases with increasing pressure at constant temperature over the *PT* range studied for each composition. For most *PTX* conditions studied, the peak position of CH_4 in the gas mixtures is at higher wavenumbers compared to the peak position of CH_4 in the pure system. The peak position of CH_4 increases at constant pressure and decreasing total concentration of CH_4, with the exception of the 15/60/25 $N_2/CO_2/CH_4$ mixture in which the peak position of CH_4 is generally located at higher wavenumbers compared to pure CH_4 but lower wavenumbers compared to the 25/25/50 mol% $N_2/CO_2/CH_4$ mixture at the same *PT* conditions over most of the range of *PT* conditions studied. The peak position of CH_4 decreases at constant pressure and decreasing total concentration of N_2. The reason for the relationship between the peak position of CH_4 and the concentration of N_2 is unclear and is discussed further in the next section. The peak position of CH_4 increases with increasing temperature at constant pressure and composition over the *PTX* range studied.

Fig. 3g-i show the partial pressure of CH_4 in a given gas mixture (Eq. 1) versus $P_{CH_4}^{PGER}$ determined from the peak position of CH_4 in the mixtures at 22°C (g), 100°C (h), and 200°C (i) using the pure CH_4 barometer of Sublett et al.[22]. The solid lines in Fig. 3g-i represent the points along the 22°C, 100°C and 200°C isotherms, respectively, at which the partial pressure of CH_4 determined from Eq. 1 using the measured total pressure of the system and the known composition of the gas mixture, and the pressure determined from the measured peak position and interpreted using the equation for the pure gas ($P_{CH_4}^{PGER}$) from Sublett et al.[22], are equivalent. The majority of the $P_{CH_4}^{PGER}$ values are greater than the partial pressure of CH_4, especially at 100°C and 200°C. Similar to CO_2, increasing temperature appears to increase the difference in $P_{CH_4}^{PGER}$ and the partial pressure of CH_4.

4. Discussion

4.1 Raman spectral behavior of N_2, CO_2, and CH_4 in mixtures

All three components in the mixtures (except in the range of ~120-160 bars for CH_4 at 22°C in the 15/60/25 mol% $N_2/CO_2/CH_4$ mixture) show a peak shift direction (i.e., to higher or lower wavenumbers) for N_2 and CH_4, and change in magnitude of Fermi diad splitting of the CO_2 component in the same direction (relative to the component in the pure system), regardless of the composition (Fig. 2). The peak position of N_2 occurs at lower wavenumbers in the mixtures relative to the pure system at the same *PT* conditions. The Fermi diad splitting of CO_2 is smaller in the mixtures relative to the pure system at the same *PT* conditions. The peak position of CH_4 is located at higher wavenumbers in the mixtures relative to the pure system at the same *PT* conditions. Differences in the peak position/Fermi diad splitting of a component in the mixture relative to the pure system must reflect intermolecular forces (attraction and repulsion) that are different from the intermolecular forces experienced by the molecule in the pure system[20]. One potential related factor is volumetric differences between the mixture and the pure gas, as the magnitude of both attraction and repulsion forces is influenced by the proximity of the molecules with each other[47] and the intermolecular distances vary in response to changes in density or volumetric properties. Interactions between different molecular species that may result in changes in the bonding environment of the molecule also likely contribute to differences in spectral behavior of a component between the pure and mixed systems. Neither factor is mutually exclusive, but each shall be addressed separately below.

4.1.1 Influence of molar volume on the direction of Raman peak shift in mixtures and pure systems

The relative strength of attraction and repulsion between molecules is dependent upon the distance between the molecules, and thus is dependent on the molar volume of the gas at a given *PTX* condition[47]. Here, we limit our discussion to CH_4 and N_2, as the Fermi resonance that causes the symmetric stretching peak of CO_2 to split into two peaks complicates the relationship between peak position and intermolecular attraction and repulsion. However, as evidenced by the behavior of pure CO_2, the change in position of the most intense peak in the Fermi diad is similar to the change in the symmetric stretching peak of N_2 and CH_4 as pressure and temperature are varied[19, 21-22, 33]. The molar volumes of the gas mixtures discussed below are calculated using the NIST REFPROP version 10.0 program[49] and the GERG2008 EOS[50], and the molar volumes of pure CH_4 and pure N_2 were calculated using the Setzmann and Wagner[51] and Span et al.[52] EOS, respectively. At constant temperature, as pressure increases in the range studied here, attraction is the dominant intermolecular force contributing to the peak shift, as evidenced by the negative shift in peak position as pressure is increased at constant temperature for all three components in all mixtures studied here[43-48]. If we assume that only the proximity of the molecules to one another (i.e. the molar volume of the mixture) controls the differences in the degree and direction of peak shift between gas mixtures, then it would be expected that the relative differences in the molar volume at constant *PT* would be similar to the relative differences in peak position at constant *PT* for a given component in mixtures with different compositions. Fig. 4a-b show the same pressure-peak position data from Fig. 2 for N_2 (a) and CH_4 (b) at 22°C, along with the pressure versus total molar volume for each gas mixture and the pure gases at 22°C (c). At a given pressure over the pressure range studied, the molar volume of pure N_2 is greater than the molar volume of any of the gas mixtures. A smaller molar volume corresponds to stronger attractive forces between molecules as the molecules are closer together[40]. Stronger attractive forces cause the peak position of a given component to decrease by a greater amount relative to weaker attractive forces[43-48]. Based on the relationship between molar volume and pressure shown in Fig. 4c, it would be expected that the peak position of pure N_2 would be located at higher wavenumbers relative to its position in the gas mixtures at 22°C and over the pressure range studied, since the molar volume of N_2 is larger than the molar volume of the gas mixtures. This expected behavior is exactly what is shown in Fig. 4a. Additionally, the magnitude of the peak shift to lower wavenumbers at a given pressure of N_2 in the mixtures roughly mirrors the molar volume differences between the mixtures. For example, the 70/15/15 mol% $N_2/CO_2/CH_4$ mixture has the largest molar volume of the gas mixtures in the pressure range studied at 22°C, and it also has the highest peak position at a given pressure relative to the other mixtures. The 25/25/50 mol% and 34/33/33 mol% $N_2/CO_2/CH_4$ mixtures have similar molar volumes and peak positions of N_2 at a given pressure, though the order is reversed in pressure-peak position space relative to pressure-molar volume space. Finally, the 15/60/25 mol% $N_2/CO_2/CH_4$ mixture has the smallest molar volume at a given pressure and shows the lowest peak position of N_2 at a given pressure in the mixtures. The same relative order is observed for the variation in peak positions of CH_4 in the gas mixtures and the peak positions of N_2 and molar volumes of the mixtures (Fig. 4b). This observed molar volume effect may explain why peak positions of CH_4 in the mixtures change as a function of N_2 concentration rather than CH_4 concentration, as the molar volume of the mixture at a given pressure decreases with decreasing N_2 content but does not decrease with decreasing CH_4 content. Based on molar volume – pressure relationships shown in Fig. 4c, it would be expected that the peak positions of CH_4 in the mixtures would be located at lower wavenumbers (with the exception of the 70/15/15 mol% $N_2/CO_2/CH_4$ mixture) compared to the pure system at the same pressure because the molar volume of pure CH_4 is larger than the molar volume of any of these mixtures. However, this behavior is not observed in Fig. 4b. As discussed in the next section, in a CO_2-bearing mixture containing CH_4, the molar volume differences alone do not entirely account for the direction and magnitude of the CH_4 peak shift in the mixtures, compared to the pure system.

The relationship between the peak shift of a component in a gas mixture (relative to the peak shift of that same component in other mixtures and the pure system) and the relative molar volumes of the mixture and pure systems described above may be extended to other compositions and components as well. Fabre and Oksengorn[16] studied the Raman spectral behavior of pure N_2 and pure CH_4, along with a 45/55 mol% N_2/CH_4 mixture at room temperature over a pressure range of 0-2.5 kbars. Fig. 5a-b show the change in the total molar volume of pure N_2, pure CH_4, and the 45/55 mol% N_2/CH_4 mixture at 22°C, and Fig. 5c-d show the Raman peak position data of Fabre and Oksengorn[16] for pure N_2, pure CH_4, and the peak positions of N_2 and CH_4 in the mixture. At pressures below ~1300 bars (Fig. 5a), the molar volume of pure N_2 is greater than the molar volume of the mixture, and the molar volume of pure CH_4 is less than the molar volume of the mixture. Given the observations and interpretations applied to the ternary gas mixtures above, as long as attraction is the dominant force contributing to the direction of peak shift along the isotherm (i.e. the peak position of a component decreases with increasing pressure at constant temperature), it would be expected that the gas with the higher molar volume would have the highest peak position relative to the other gas. Because pure N_2 has a higher molar volume than the mixture, it would be expected based on the above observations that the peak position of N_2 in the pure gas would be located at higher wavenumbers relative to the peak position of N_2 in the mixture, which is the case. Also, because the molar volume of the mixture is greater than the molar volume of CH_4 at a given pressure (and CO_2 is not included in the mixture) it would be expected that the peak position of CH_4 in the mixture would be located at higher wavenumbers compared to the peak position of CH_4 in the pure gas, which is also the case. Between 1300 and 1500 bars, isotherms in Fig. 5b cross such that the molar volume of CH_4 becomes greater than the molar volumes of both N_2 and the mixture, and the molar volume of N_2 becomes less than the molar volume of the mixture. Incidentally, this intersection point roughly corresponds to the point in Fig. 5c-d where the peak positions of CH_4 and N_2 no longer decrease with increasing pressure but rather show a slight increase with increasing pressure at constant temperature. This inflection point where the trend in peak position with pressure at constant temperature reverses is referred to as the isothermal inflection pressure and represents the point in *PTX* space where the decrease in peak position as a result of attraction is balanced by the contribution of repulsion that serves to increase the peak position. At pressures above this inflection pressure, repulsion is the dominant intermolecular force contributing to the peak shift[22]. In the region where repulsion is the dominant contributor to peak shift, larger molar volumes correspond to weaker repulsive forces because repulsive forces decrease as the distance between molecules increases[40]. In the region where repulsion is the dominant contributor to peak shift, the component of the gas with the larger molar volume should (based on the observations made in the attraction dominated region) have lower peak positions at a given pressure relative to the component in a gas with a smaller molar volume at the same *PT* conditions because stronger repulsive forces correspond to larger positive peak shifts[43-48]. As can be seen from Fig. 5b-d, pure CH_4 has the largest molar volume in the repulsion dominated region, which corresponds to CH_4 peak positions in the pure gas located at lower wavenumbers at the same pressure relative to the peak positions of CH_4 in the mixture, which has a smaller molar volume than pure CH_4. The molar volume of pure N_2 is smaller than the molar volume of the mixture in the repulsion dominated region, and corresponds to peak positions of N_2 in the pure system that are located at higher wavenumbers compared to the peak positions of N_2 in the mixture, which has a larger molar volume.

Seitz et al.[29] studied the Raman spectral behavior of binary CH_4-bearing gas mixtures containing 50 mol% CH_4 with H_2, N_2, Ar, or CO_2 as the other component. Fig. 6a-b show their data for the peak position of CH_4 in the pure system and in the mixtures (a), and the molar volumes of each mixture and pure CH_4 (b), both as a function of pressure and at 22°C. The pressure region studied by Seitz et al.[29] is within the region where the contribution of attractive interactions dominates the peak shift, as evidenced by the shift in the position of the CH_4 peak to lower wavenumbers with increasing pressure in the pure system and in the 50/50 mol% N_2/CH_4, H_2/CH_4, and Ar/CH_4 mixtures (except perhaps in the Ar/CH_4 mixture above ~450 bars where the isothermal inflection pressure may have been reached or is neared based on the shallow slope of the pressure-peak position trend and the intersection of the isotherms in pressure-molar volume space). As can be seen in Fig. 6, the molar volumes of the 50/50 mol% N_2/CH_4, H_2/CH_4, and Ar/CH_4 mixtures are all greater than the molar volume of pure CH_4 (except the Ar/CH_4 mixture above ~450 bars) and the peak position of CH_4 in the mixtures at a given pressure is located at higher wavenumbers than the peak position of CH_4 in the pure system, agreeing with the above observations. Additionally, the relative order of curves showing the variation in molar volume as a function of pressure for pure CH_4 and for the 50/50 mol% N_2/CH_4, H_2/CH_4, and Ar/CH_4 mixtures is the same as the relative order of increasing peak position at a given pressure. When the fluid mixture contains CO_2, as in the 50/50 mol% CO_2/CH_4 mixture, the molar volume relationship described above does not hold and cannot be applied to predict the relative direction of peak shift of CH_4 in the mixture relative to the pure system. As such, based on the relative molar volumes of the 50/50 mol% CO_2/CH_4 mixture and pure CH_4, we would expect that the peak positions of CH_4 in the 50/50 mol% CO_2/CH_4 mixture would be located at lower wavenumbers relative to the pure system at the same pressure, which is not observed in Fig. 6a, except in the range 150-300 bars. It should be noted, however, that as with the ternary mixtures (Fig. 4), while the relative molar volumes cannot be used to predict the relative shift of the CH_4

peak in the CO_2-bearing mixture compared to the pure system, the relative molar volumes can still be used to predict the relative shift of the CH_4 peak in the CO_2-bearing mixture compared to the other mixtures in Fig. 6.

Predicting the direction of peak shift based on the relative molar volume of a gas mixture compared to that of a pure gas also appears to be valid for other gas systems. May et al.[43] conducted Raman analyses of pure H_2 and ~25/75 mol% H_2/Ar and H_2/He mixtures at room temperature. Fig. 7 shows their data on the peak position of the strongest vibrational line of H_2 (nominally located at 4155.2 cm^{-1} at 1 bar)[43] in the mixtures and in the pure system at 22°C at various pressures (a) and the molar volumes of the mixtures and pure H_2 (b). The molar volume of pure H_2 was calculated using the Leachman et al. EOS[53]. The peak position of H_2 in both the pure H_2 system and in the ~25/75 mol% H_2/He mixture appears to increase with increasing pressure and suggests that contribution of repulsion to peak shift dominates over attraction at these conditions. Based on the observations made above, in a repulsion dominated region, it would be expected that peak positions for the gas with the larger molar volume would occur at lower wavenumbers relative to a gas with a lower molar volume because repulsion shifts the peak position to higher wavenumbers and a larger molar volume corresponds with a greater distance between molecules, which weakens repulsive forces experienced between molecules[40].

From Fig. 7b, it can be seen that pure H_2 has a larger molar volume than the ~25/75 mol% H_2/He mixture and the strongest vibrational line of H_2 in the pure system occurs at lower wavenumbers than that of H_2 in the ~25/75 mol% H_2/He mixture. The ~25/75 mol% H_2/Ar mixture provides another example of a gas that passes through its isothermal inflection pressure over the range of pressures studied. For this mixture, the peak position of H_2 in the mixture moves to lower wavenumbers with increasing pressure at pressures below ~700 bars. Above ~700 bars, the peak position of H_2 in the mixture shifts to higher wavenumbers with increasing pressure. Just as with the N_2-CH_4 system, the isothermal inflection pressure roughly corresponds with the pressure at which the molar volumes of the ~25/75 mol% H_2/Ar mixture and the pure gas become equal. Below this pressure, the ~25/75 mol% H_2/Ar mixture is in the attraction dominated region and has both the lowest molar volume and the lowest H_2 peak positions relative to the pure system and the ~25/75 mol% H_2/He mixture (Fig. 7). Above this pressure, the ~25/75 mol% H_2/Ar mixture is in the repulsion dominated region and has the highest molar volume and the lowest H_2 peak positions relative to the pure system and the ~25/75 mol% H_2/He mixture (Fig. 7).

While the relationship between molar volume and peak position does not hold for all compositions, especially for pure CH_4 relative to the CH_4 component in CO_2-bearing mixtures, the relative differences in molar volume between mixtures and pure gases can be related to the direction of peak shift of a component in a given mixture relative to that same component in other mixtures or the pure system. Fig. 8 is a schematic representation of the observed relationship between the direction of peak shift and relative molar volumes for two example gases. In the region in which the attractive contribution to the peak shift exceeds the repulsive contribution to the peak shift (left side of Fig. 8), the peak position shifts to lower wavenumber with increasing pressure. In this region, a larger molar volume corresponds to weaker attractive interactions between molecules because the molecules are further apart relative to the gas with the smaller molar volume. This, in turn, corresponds to weaker attractive forces and a smaller shift in peak position of the component. In the attraction dominated region, larger molar volumes correspond to larger peak position shifts relative to the gas with the smaller molar volume at the same *PT* conditions. In the region in which the repulsive contribution to the peak shift exceeds the attractive contribution to the peak shift (right side of Fig. 8), the peak position shifts to higher wavenumbers with increasing pressure. In this region, a larger molar volume corresponds to weaker repulsive interactions between molecules because the molecules are further apart relative to the gas with the smaller molar volume. This, in turn, corresponds to a smaller shift in the peak position of the component to higher wavenumbers because repulsion is weaker, indicating that in the repulsion dominated region, larger molar volumes correspond to peak positions shifted to lower wavenumbers relative to the gas with the smaller molar volume at the same *PT* conditions. At the isothermal inflection pressure (dashed line in Fig. 8), the attractive and repulsive contributions to peak shift are equal and the peak position of the component in the mixture is the same as that of the pure gas. This point also roughly corresponds to the point in molar volume-pressure space where the isotherms of the two gases cross.

4.1.2 Influence of non-ideality and CO_2 concentration on the Raman peak position of CH_4 and N_2 in gas mixtures

The trends in molar volume and peak position described above do not apply to pure CH_4 relative to CH_4 in the CO_2-bearing mixtures studied here (except for the 70/15/15 mol%

$N_2/CO_2/CH_4$ mixture). To assess the effect of CO_2 on the shift in peak position of CH_4 in the gas mixtures, we examined the effect of CO_2 on the departure from ideality of CH_4 in the gas mixtures because non-ideal behavior reflects molecular interactions that also influence the direction and magnitude of the Raman peak shift with changing *PT*. One way to assess the departure from ideal behavior is through the fugacity of the components in the gas, which takes into account interactions between molecules and thus serves as a measure of the non-ideality of a gas or gas mixture. The fugacity of a component in a mixture is given by the following equation:

$$f_i = \phi_i * P * X_i \tag{2}$$

Where f_i is the fugacity of component *i* and ϕ_i is the fugacity coefficient of component *i*. The fugacity coefficient relates the pressure (or partial pressure in the case of mixtures) of a component to the fugacity to account for the non-ideal behavior observed. If like molecules interact with one another or with molecules of another component, the partial pressure measured for the component will not equal the partial pressure predicted by Eq. 1. Instead, the pressure recorded will either be greater or less than the partial pressure. The fugacity coefficient corrects the partial pressure to the recorded pressure and thus the fugacity coefficient serves as an indicator of the non-ideal behavior of the component in the mixture. If the component in a mixture behaves ideally, the partial pressure and fugacity are equivalent, and the fugacity coefficient is equal to unity. If the component in the mixture behaves non-ideally, the partial pressure and fugacity are not equal and the fugacity coefficient is either greater or less than one, depending on the types of interactions in the gas.

Fugacity coefficients of N_2 and CH_4 in the pure systems and in the mixtures at 22°C and 10-500 bars were calculated using the NIST REFPROP version 10.0 program[49] and the GERG2008 EOS[50] for the mixtures, Setzmann and Wagner[51] EOS for pure CH_4, and Span et al.[52] EOS for pure N_2 (Fig. 9). As shown in Fig. 9a, the fugacity coefficient of N_2 generally increases with decreasing N_2 mole fraction in the mixtures. The 34/33/33 and 25/25/50 mol % $N_2/CO_2/CH_4$ mixtures are inverted in this order, but both mixtures have similar molar volumes[49-50] (see Fig. 4) and critical points[49-50] and the pressure-peak position behavior of N_2 in these two mixtures is similar at 22°C (Fig. 2a). The variation in fugacity coefficient with N_2 mole fraction at a constant pressure in the mixtures and pure system is similar to the variation in N_2 peak position at 22°C with N_2 mole fraction at constant pressure (Figs. 2a, 4a) and is also similar to the variation in molar volume relative to N_2 mole fraction at constant pressure (Fig. 4c). In all cases, peak position, fugacity coefficient, and molar volume all show systematic variations (with the 34/33/33 and 25/25/50 mol % $N_2/CO_2/CH_4$ mixtures being similar for each variable) as a function of mole fraction N_2.

Unlike N_2, peak position, fugacity coefficient, or molar volume of the mixtures do not all change in the same direction with changing CH_4 mole fraction. As such, the isotherm for the 15/60/25 mol % $N_2/CO_2/CH_4$ mixture is located at much higher fugacity coefficient values than is observed in any of the other mixtures (Fig. 9b). If this mixture were excluded from the plots, the fugacity coefficient for CH_4 at a given pressure would show a continuous and systematic increase with decreasing mole fraction CH_4. Similarly, the peak position of CH_4 in the mixtures and pure system (Figs. 2g, 4b) at a given pressure increases continuously with decreasing mole fraction of CH_4 if the 22°C isotherm for the 15/60/25 mol % $N_2/CO_2/CH_4$ mixture is excluded. All of the fugacity coefficients for CH_4 in the pressure range shown in Fig. 9b are less than unity, implying that attraction is the dominant force experienced by the CH_4 molecules in the gas mixtures. This may not indicate the dominant intermolecular force on the contribution to peak shift. For example, based on the fugacity coefficients of pure N_2 and N_2 in the mixtures, the N_2 molecules are dominated by repulsive interactions in the gas mixtures as the fugacity coefficients are greater than one. However, the dominant intermolecular force on the peak shift of N_2 in the same pressure range is attraction based on the direction of peak shift in Fig. 2a with increasing pressure. While the dominant intermolecular force experienced by the molecules in the mixture may not correspond to the force that is dominant on the peak shift, it does provide a potential factor in the peak position of CH_4 being lower than the mixtures even though the molar volume of CH_4 is higher than most of the mixtures. These observations indicate that peak positions of CH_4 are also affected by the non-ideality of the gas mixtures, in addition to the molar volume differences.

To assess whether the anomalous behavior shown by the 15/60/25 mol % $N_2/CO_2/CH_4$ mixture is due to the high CO_2 concentration, the 22°C isotherm for a mixture with the same 25 mol% CH_4 but inverted concentrations of N_2 and CO_2 (i.e., 60/15/25 mol % $N_2/CO_2/CH_4$) is plotted in Fig. 9b as the dashed purple line. As shown by Fig. 9b, the trend for the mixture in which CO_2 is no longer the most abundant component falls between the 50 mol% CH_4 and the 33 mol% CH_4 mixture, and the relative fugacity coefficient values are similar to those for the other mixtures. This indicates that the significant difference in fugacity coefficient observed between the 15/60/25 mol % $N_2/CO_2/CH_4$ mixture and the other mixtures is related to the fact that CO_2 is the dominant component in this mixture.

Compared to N_2 (~-147°C) and CH_4 (~-83°C), the critical temperature of CO_2 is higher (~31°C). Mixtures of N_2, CO_2, and CH_4 with significant molar proportions of CO_2 may have critical temperatures that are close to the analytical temperature of 22°C. Proximity to the critical point affects the relative strengths of the intermolecular forces experienced by molecules, which in turn affects both the fugacity coefficient and the peak position of the components in the mixture. For example, in the pure N_2, CO_2, and CH_4systems, the contribution of attraction to the peak shift becomes stronger as temperature approaches the critical temperature[22]. The 15/60/25 mol% $N_2/CO_2/CH_4$ gas mixture has the highest critical temperature of the mixtures in this study (~-11°C)[49-50] and proximity to the critical temperature likely contributes to the fact that peak positions of CH_4 and N_2 in this mixture are located at lower wavenumbers at a constant pressure, relative to the other mixtures at 22°C.

When CO_2 is the most abundant component in the mixture, as for the 15/60/25 mol% $N_2/CO_2/CH_4$ gas mixture, the fugacity coefficient of N_2 also shows unexpected behavior when compared to the fugacity coefficients of the other mixtures and pure system (Fig. 9a). Similar to CH_4, a gas mixture with the same mole fraction of N_2 as the 15/60/25 mol% $N_2/CO_2/CH_4$ gas mixture but with the concentrations of CO_2 and CH_4 reversed (i.e., 15/25/60 mol% $N_2/CO_2/CH_4$) is plotted in Fig. 9a as the dashed purple line. When CO_2 is not the most abundant component, the trend in fugacity coefficients of the 15 mol% N_2 mixture is more similar to that of the other mixtures. However, because this mixture had the lowest N_2 concentration, there is no noticeable difference in the peak position values for N_2 in the 15/60/25 mol% $N_2/CO_2/CH_4$ gas mixture relative to the other mixtures and the pure system (Fig. 2a). The fugacity coefficients for this mixture are still higher than the fugacity coefficients of the other mixtures at the same pressures and, given the molar volume/fugacity coefficient related behavior observed for N_2, it is likely that the shifts in peak positions of N_2 for this mixture would be similar to that of N_2 in the other mixtures. To assess whether increased concentrations of CO_2 could cause the fugacity coefficient isotherms in Fig. 9a to appear "out of order", such that increasing N_2 concentration would not lead to a continuous increase in the fugacity coefficient at constant pressure, the fugacity coefficients for a 25/50/25 mol% $N_2/CO_2/CH_4$ gas mixture (same N_2 concentration as the 25/25/50 mol% $N_2/CO_2/CH_4$ mixture with the concentrations of CO_2 and CH_4 reversed) are also plotted on Fig. 9a as the dashed green line. As can be seen in Fig. 9a, fugacity coefficients for the 25/50/25 mol% $N_2/CO_2/CH_4$ gas mixture (green dashed line) are greater than those for the 15/25/60 mol% $N_2/CO_2/CH_4$ gas mixture (purple dashed line), and appear to be "out of order" with respect to the systematic relationship between fugacity coefficient and mole fraction N_2 in the CO_2-poor mixtures, and is similar to the "out of order" isotherms for CH_4 from this study (Fig. 9b). While the effect of the CO_2 concentration on the peak positions of N_2 in the 25/50/25 mol% $N_2/CO_2/CH_4$ gas mixture cannot be assessed without Raman spectral data on the mixture, the observations from CH_4 and the proximity of the analytical temperature for this mixture to its critical temperature implies that the peak positions of N_2 in this mixture should be located at lower wavenumbers relative to the 25/25/50 mol% $N_2/CO_2/CH_4$ mixture. Further study is required to assess the differences in the Raman spectral behavior of N_2 and CH_4 in CO_2-rich and CO_2-poor gas mixtures.

4.2 Relationship between pressure derived from Raman data and fugacity

Recently, Lamadrid et al.[20] demonstrated that interactions between N_2, CO_2, and CH_4 molecules in a ternary gas mixture are recorded in the Raman spectral properties of the mixture. The authors give the following relationship between the pressure determined for a given component *i* using the pure gas barometers (here referred to as P_i^{PGER}) and the fugacity of that component in the mixture[20]:

$$f_i = \frac{f_{v,i}}{P_i^{PGER}} * P * X_i \tag{3}$$

where $f_{v,i}$ is the fugacity of the pure component *i* at a pressure estimated from Raman peak positions using the pure gas barometers, (P_i^{PGER}). Lamadrid et al.[20] used the Redlich-Kwong equation of state (RKEOS)[55] and the pure gas barometer for N_2 developed in their study[20], as well as barometers developed by Fall et al.[19] for CO_2 and by Lin et al.[17] for CH_4. In this study we used the GERG2008 EOS[50] to calculate molar volumes and fugacity coefficients, however because the model of Lamadrid et al. (2018) is developed from fundamental relationships of fugacity and pressure without a specific equation of state, f_i and $f_{v,i}$ determined using the GERG2008 EOS instead of the RKEOS should be similar. The barometers of Sublett et al.[22] are used here to calculate P_i^{PGER} in Eq. 3 for the reasons discussed in section 3.1. Fig. 10 shows the fugacity calculated at the known *PTX* conditions (f_{EOS}) using the GERG2008 EOS[50] versus the fugacity calculated by Eq. 3 (f_i) for N_2 (a-c), CO_2 (d-f), and CH_4 (g-i) in each mixture at 22°, 100° and 200°C. The solid black lines in Fig. 10 show 1:1 correlation between f_{EOS} and f_i. The fugacity model developed by Lamadrid et al.[22] reproduces the fugacities of CH_4 and CO_2 in all of the mixtures and N_2 in the 70/15/15 mol% N_2/CO_2/CH_4 mixture well. The major differences between f_{EOS} and f_i are observed at high-pressures for N_2 in the 15/60/25, 25/25/50, and 34/33/33 mol% N_2/CO_2/CH_4 mixtures. This discrepancy may likely be attributed to the peak positions of N_2 in these mixtures being located at lower wavenumbers at higher pressures, relative to the peak position of pure N_2 at the same *PT* conditions. The unrealistically high pressures obtained by applying the pure gas barometer to these peak positions results because the barometer is being used at peak positions that are outside of the range of those used to develop the barometer. The rate at which the peak for pure N_2 migrates to lower wavenumbers with increasing pressure decreases as pressure increases above ~200 bars[22]. Above ~200 bars, small changes in peak position correspond to large changes in pressure. Thus, extrapolation of the barometer to the peak positions for N_2 obtained from the 15/60/25, 25/25/50, and 34/33/33 mol% N_2/CO_2/CH_4 gas mixtures predicts pressures as high as 2000 bars. These unrealistically high pressures are likely the cause of the poor correlation between pressure predicted by Eq. 3 for N_2 in the gas mixtures at total pressures above ~100 bars. The f_i of N_2 and CO_2 approach f_{EOS} for all mixtures with increasing temperature, and f_i and f_{EOS} for CH_4 show good agreement at all temperatures.

4.3 Barometer for the N_2-CO_2-CH_4 ternary system based on N_2 peak position

The total pressure of any of the four gas mixtures analyzed in this study can be predicted reasonably well between 22-200°C using only the peak position of N_2. As such, the following Raman peak position barometer for the N_2-CO_2-CH_4 ternary system was developed:

$$P = \sum_{i=0}^{4} \sum_{j=0}^{4} \sum_{k=0}^{4} A_{i,j,k} \left[ln \left\{ \left(\frac{v \cdot 1000}{2330} \right) - 998 \right\} \right]^i X_{N_2}^j \left(\frac{T}{100} \right)^k \tag{4}$$

where v is the peak position of N_2 in the mixture and T is the temperature in degrees Celsius. The fitting coefficients for Eq. 4 are given in table 1. The convention used to adjust the peak position of N_2 in Eq. 4 is taken from Sublett et al.[22] and serves to highlight the small changes in the N_2 peak position with changing pressure. Eq. 4 was developed using 293 data points collected from 22-200°C from pure N_2[22], 70/15/15 mol% (22°C data from Lamadrid et al.[20]), 34/33/33 mol%, 25/25/50 mol%, and 15/60/25 mol% N_2/CO_2/CH_4 mixtures. Eq. 4 has an R^2 of 0.996, a root mean square (*RMS*) of 0.091177, and an average error of ±6.5% of the total pressure. CO_2 and CH_4 do not behave as systematically as N_2 and the fits for CO_2 and CH_4 have average errors of

±12.2% and ±19.8%, respectively, and are not provided here. Fig. 11a shows the application of Eq. 4 to the four gas mixtures and pure N_2 at various temperatures ranging from 22-200°C. All of the data plotted in Fig. 11, including the temperature corresponding to each data point, are included in the supplementary information. Because Eq. 4 does not depend on the concentration of the other components in the mixture, the model was tested at 22°C on several N_2/CH_4 binary mixtures[16, 29], including a 25/75 mol% N_2/CH_4 mixture measured in this study, a 80/5/5/5/5 mol% $N_2/CH_4/C_3H_8/C_4H_{10}/C_2H_6$ measured in this study, and an H_2O-N_2-CO_2-CH_4 bearing synthetic fluid inclusion (SFI) containing a vapor bubble with 24/69/7 mol% $N_2/CO_2/CH_4$ (composition determined from the Raman peak area ratios) measured in this study. The results are plotted in Fig. 11b. These gases (with the exception of the SFI) were chosen as the molar volumes and fugacity coefficients of N_2 in these mixtures behave in a manner that is similar to the ternary mixtures as described in the previous sections, and were likely to exhibit Raman spectral behavior similar to the examples given in section 4.1.1. The SFI was selected to test the model against a CO_2-rich, N_2-CO_2-CH_4 mixture composition. At room temperature the SFI contains an H_2O-rich liquid phase and a N_2-CO_2-CH_4 rich vapor phase, and the amount of H_2O dissolved in the vapor bubble at room temperature is negligible. As can be seen from Fig. 11b, Eq. 4 predicts the known total pressures of the gases reasonably well. Some of the scatter in Fig. 11b may be due to the studies using older instruments with lower quality resolution and that the literature data from Fabre and Oksengorn[16], Seitz et al.[29], and Seitz et al.[30] for Raman peak positions of N_2 used in Fig. 11b had to be taken directly from graphs. Eq. 4 should not be used for pressures below 60-80 bars as it does not reproduce the pressures in the ternary mixtures used in the fit well, which is why Fig. 11b only shows data for pressures above 60 bars. Also, more work needs to be done on CO_2-rich ternary mixtures, and as such it is not recommended that Eq. 4 be used on mixtures with an N_2:CO_2 ratio greater than 1:4. Eq. 4 is not valid for pressures greater than ~500 bars, temperatures below 22°C or above 200°C, or for mixtures containing less than 15 mol% N_2.

4.4 Applications to natural fluid inclusions

Eq. 4 can be applied to determine the pressure of N_2-CO_2-CH_4 fluid inclusions (FI) using N_2 peak positions derived from Raman spectroscopy. In many FI studies, it is necessary to define an isochore (line of constant density) along which the trapped fluid evolved during cooling and depressurization from trapping conditions. The isochore may be combined with information on the trapping temperature to determine trapping pressure, and consequently trapping depth, of the fluid inclusions and its host mineral. For the system N_2-CO_2-CH_4, the density of the fluid can be determined based on extensive petrographic and microthermometric data[56]. For example, Xu et al.[57] were able to determine the density of N_2-CO_2-CH_4 FIs by measuring the temperature at which solid CO_2 melted ($T_{m,CO2}$) and the temperature at which two CO_2 fluid phases, one of which was nucleated upon cooling, homogenized into a single phase ($T_{h,CO2}$). With this information, along with *V-X* phase diagrams provided by Thiery et al.[56], the authors defined the composition and molar volume of the fluid. However, it would also be possible to determine the molar volume, and thus the density, of the fluid if the pressure inside the FI were known, using an EOS. It is common for Raman spectroscopy to be used to confirm the presence of gas species in FI, and data needed to use the barometer presented here is easily obtained during Raman analysis. Obtaining the necessary data via Raman analysis could eliminate uncertainties associated with metastable phase behavior that has been observed during microthermometric analysis of FI that contain ternary mixtures of N_2, CO_2, and CH_4 and makes it difficult to obtain reliable T_m and T_h data[4]. The two methods may be used in combination as well. The pressure in the SFI reported in Fig. 11b was determined from both Raman analysis to determine the N_2 peak position and microthermometry, and both methods provided a similar internal pressure at 22°C.

5. Summary

The Raman spectral behavior of N_2, CO_2, and CH_4 in ternary mixtures differs significantly from the pure systems. Peak positions of N_2 are always greater in the pure system relative to the mixtures at the *PT* conditions studied, while peak positions of CH_4 are always greater in the mixtures relative to the pure system at the *PT* conditions studied. The differences in relative peak position of a component in the mixtures with other mixtures and the pure systems correspond with differences in the molar volume and fugacity coefficients (non-ideal behavior) of the mixtures relative to one another and the pure systems. Relative molar volume differences reflect the relative peak position differences for several components, mixtures, and pure systems at a given pressure. The one exception found in this study is pure CH_4 relative to CH_4 in CO_2-bearing mixtures. Relative differences in the fugacity coefficient, and thus relative differences in non-ideality, of N_2 and CH_4 in the ternary mixtures and pure systems also correspond to relative differences in the peak position of N_2 and CH_4 in the mixtures relative to each other and the pure systems. The Raman spectral behavior of various components in several gas mixtures behave similarly relative to other mixtures and pure systems, and with extensive characterization of these similarities, fundamental fluid properties may be obtained from Raman spectroscopy.

Acknowledgements

The authors thank Charles Farley for a great deal of assistance with the calibration and use of the Raman spectrometer and Yury Klyukin and Lowell Moore for many helpful conversations on the topic of molecular interactions and Raman spectral behavior. The authors would also like to thank Bob Burruss for providing the capillary stage and sage wisdom on thermodynamics. This material is based in part on work supported by the National Science Foundation under grant numbers EAR-1624589 and OCE-1459433 to RJB. HML was supported by the PFF fellowship at the University of Missouri. MS-M was supported by a Discovery Grant from NSERC.

References

[1] H. E. C. Swanenberg, *Geologica Ultraiectina* **1980**; *25*, 1.

[2] J. Touret, in *Short Course in Fluid Inclusions: Application to Petrology*, (Eds. L. S. Hollister, M. L. Crawford), Mineral association of Canada, Markham, **1981**, pp. 182-208.

[3] R. Kreulen, R. D. Schuiling, *Geochim. Cosmochim, Acta* **1982**; *46*, 193.

[4] A. M. Van den Kerkhof A. M., *Ph. D. thesis*, Univ. Amsterdam, **1988**.

[5] C. J. S. DeAlvarenga, M. Cathelineau, J. Dubessy, *Mineral. Mag.* **1990**; *54*, 245.

[6] V. Lüders, B. Plessen, *Mar. Petrol. Geol.* **2015**; *63*, 68-81.

[7] M. Z. Stout, M. L. Crawford., E. D. Ghent, *Contrib. Mineral. Petrol.* **1986**; *92*, 236-247.

[8] J. Touret, P. Dietvorst, *Geol. Soc. London*. **1983**; *140*, 635-649.

[9] B. W. D. Yardley, T. J. Shepherd, J. P. Barber, in *Migmatites, Melting and Metamorphism,* (Eds. M. P. Atherton, C. D. Gribble), Shiva Publ. Co., Nantwich, **1983**, pp. 110-126.

[10] M. L. Crawford, L. S. Hollister, in *Fluid-Rock Interactions during Metamorphism*, (Eds. J. V. Walther, B. J. Wood), Springer-Verlag, New York, **1986**, pp. 1-35.

[11] P. D. Jenden, I. R. Kaplan, R. Poreda, H. Craig, *Geochim. Cosmochim. Acta* **1988**; *52*, 851.

[12] L. Palcsu, I. Vető, I. Futó, G. Vodila, L. Papp, Z. Major, *Marine Petrol. Geol.* **2014**; *54*, 216.

[13] E. L. Klein, C. Harris, C. Renac, A. Giret, C. A. V. Moura, K. Fuzikawa, *Miner. Depositia* **2006**; *41*, 160.

[14] E. Chicharro, M. Boiron, J. A. López-García, D. N. Bardfod, C. Villaseca, *Ore Geol. Rev.* **2016**; *72*, 896.

[15] D. V. Petrov, *Spectrochim. Acta* **2018**; *191*, 576.

[16] D. Fabre, B. Oksengorn, *Appl. Spectrosc.* **1992**; *46*, 468.

[17] F. Lin, R. J. Bodnar, S. P. Becker, *Geochim. Cosmochim. Acta* **2007**; *71*, 3746.

[18] F. Lin, A. K. Sum, R. J. Bodnar, *J. Raman Spectrosc.* **2007**; *38*, 1510.

[19] A. Fall, B. Tattitch, R. J. Bodnar, *Geochim. Cosmochim. Acta* **2011**; *75*, 951.

[20] H. M. Lamadrid, M. Steele-MacInnis, R. J. Bodnar, *J. Raman. Spectrosc.* **2018**; *49*, 581.

[21] H. M. Lamadrid, L. R. Moore, D. Moncada, J. D. Rimstidt, R. C. Burruss, R. J. Bodnar, *Chem. Geol.* **2017**; *450*, 210.

[22] D. M. Sublett, E. Sendula, H. M. Lamadrid, M. Steele-MacInnis, G. Spiekermann, R. C. Burruss, R. J. Bodnar, *J. Raman. Spectrosc.* **In press**

[23] D. Fabre, R. Couty, *Comptes Rendus L Acad Des Sci Ser II* **1986**; *303*, 1305.

[24] R. Kroon, M. Baggen, A. Lagendijk, *J. Chem. Phys.* **1989**; *97*, 74.

[25] B. Lavorel, B. Oksengorn, D. Fabre, R. Saint-Loup, H. Berger, *Mol. Phys.* **1992**; *75*, 397.

[26] R. D. Etters, J. Belak, R. LeSar, *Phys. Rev. B* **1986**; *34,* 4221.

[27] T. Dreier, G. Schiff, A. A. Suvernev, *J. Chem. Phys.* **1994**; *100*, 6275.

[28] G. S. Devendorf, D. Ben-Amotz, *J. Phys. Chem.* **1993**; *97*, 2307.

[29] J. C. Seitz, J. D. Pasteris, I-M. Chou, *Amer. J. Sci.* **1993**; *293*, 297.

[30] J. C. Seitz, J. D. Pasteris, I-M. Chou, *Amer. J. Sci.* **1996**; *296*, 577.

[31] I-M. Chou, J. D. Pasteris, J. C. Seitz, *Geochim. Cosmochim. Acta* **1990**; *54*, 535.

[32] V. Thieu, S. Subramanian, S. O. Colgate, E. D. Sloan Jr, *Ann N Y Acad Sci* **2000**; *912*, 983.

[33] L. Shang, I-M. Chou, R. C. Burruss, R. Hu, X. Bi, *J. Raman Spectrosc.* **2014**; *45*, 696.

[34] W. Lu, I-M. Chou, R. C. Burruss, Y. Song, *Geochim. Cosmochim. Acta* **2007**; *71*, 3969.

[35] S. Brunsgaard Hansen, R. W. Berg, E. H. Stenby, *Appl. Spectrosc.* **2001**; *55*, 745.

[36] B. Lavorel, R. Chaux, R. Saint-Loup, H. Berger, *Opt. Commun.* **1987**; *62*, 25.

[37] S. C. Schmidt, D. S. Moore, M. S. Shaw, *Phys. Rev. B* **1987**; *35*, 493.

[38] K. M. Rosso, R. J. Bodnar, *Geochim. Cosmochim. Acta* **1995**; *59*, 3961.

[39] Y. Kawakami, J. Yamamoto, H. Kagi, *Appl. Spectrosc.* **2003**; *57*, 1333.

[40] J. Yamamoto, H. Kagi, *Chem. Lett.* **2006**; *35*, 610.

[41] X. Wang, I-M. Chou, W. Hu, R. C. Burruss, Q. Sun, Y. Song, *Geochim. Cosmochim. Acta* **2011**; *75*, 4080.

[42] I-M. Chou, R. C. Burruss, W. Lu, *Adv. High-Pressure Technol. Geophys. Appl.* **2005**; 475-485.

[43] A. D. May, V. Degen, J. C. Stryland, H. L. Welsh, *Can. J. Phys.* **1961**; *39*, 1769.

[44] B. Oksengorn, D. Fabre, B. Lavorel, R. Saint-Loup, H. Berger, *J. Chem. Phys.* **1991**; *94*, 1774.

[45] W. Schindler, J. Jonas, *J. Chem. Phys.* **1980**; *73*, 3547.

[46] W. Schindler, P. T. Sharko, J. Jonas, *J. Chem. Phys.* **1982**; *76*, 3493.

[47] K. S. Schweizer, D. Chandler, *J. Chem. Phys.* **1982**; *76*, 2296.

[48] M. R. Zakin, D. R. Herschbach, *J. Chem. Phys.* **1986**; *85*, 2376.

[49] E.W. Lemmon, I. H. Bell, M.L. Huber, M.O. McLinden, *NIST Standard Reference Database 23: Reference Fluid Thermodynamic and Transport Properties-REFPROP, Version 10.0*, National Institute of Standards and Technology, Standard Reference Data Program, Gaithersburg, **2018**.

[50] O. Kunz, W. Wagner, *J. Chem. Eng. Data.* **2012**; *57*, 3032.

[51] U. Setzmann, W. Wagner, *J. Phys. Chem.* **1991**; *20*, 1061.

[52] R. Span, E. W. Lemmon, R. T. Jacobsen, W. Wagner, A. Yokozeki, *J. Phys. Chem.* **2000**; *29*, 1361.

[53] J. W. Leachman, R. T. Jacobsen, S. G. Penoncello, E. W. Lemmon, *J. Phys. Chem. Ref. Data*. **2009**; *38,* 721.

[54] J. R. Holloway, *In Thermodynamics in geology* (ed. D. G. Fraser) D. Reidel Publishing Company, Boston, **1977**; pp. 161.

[55] O. Redlich, J. N. S. Kwong *Chem. Rev.* **1949**; *44*, 233.

[56] R. Thiery, J. Vidal, J Dubessy, *Geochim. Cosmochim. Acta* **1994**; *58*, 1073.

[57] J. Xu, C. J. R. Hart, L. Wang, H. Chu, L. Lin, X. Wei, *China. Econ. Geol.* **2011**; *106*, 145.

Figures

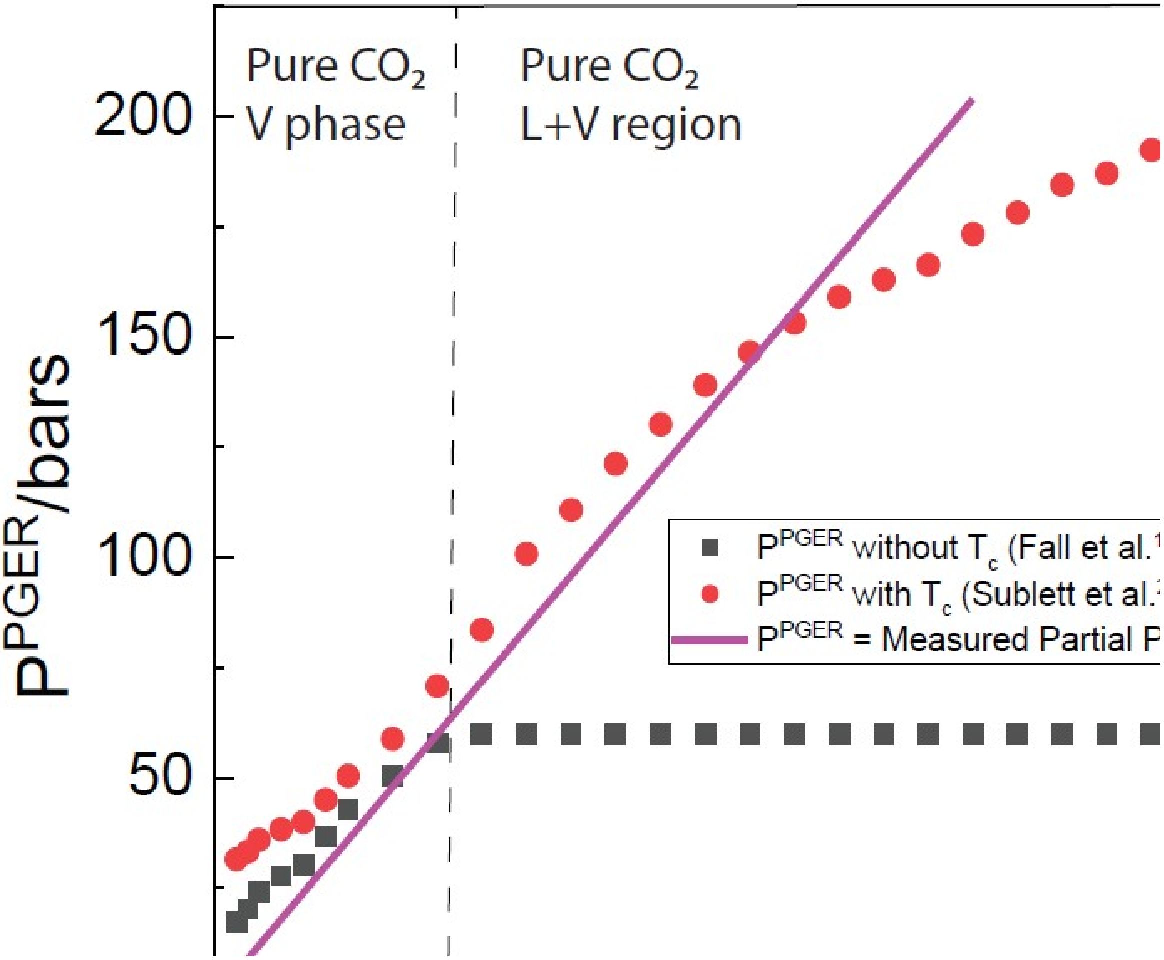

Fig. 1. Plot of the partial pressure of CO_2 vs the pure gas equivalent Raman pressure of CO_2 ($P_{CO_2}^{PGER}$) calculated using the barometer of Fall et al.[19] that does not take into account the critical temperature (T_C) of the gas (black squares) and calculated using the barometer of Sublett et al.[22] that does take into account the critical temperature of the gas (red circles). The solid black lines represent where the partial pressure of CO_2 and $P_{CO_2}^{PGER}$ are equivalent.

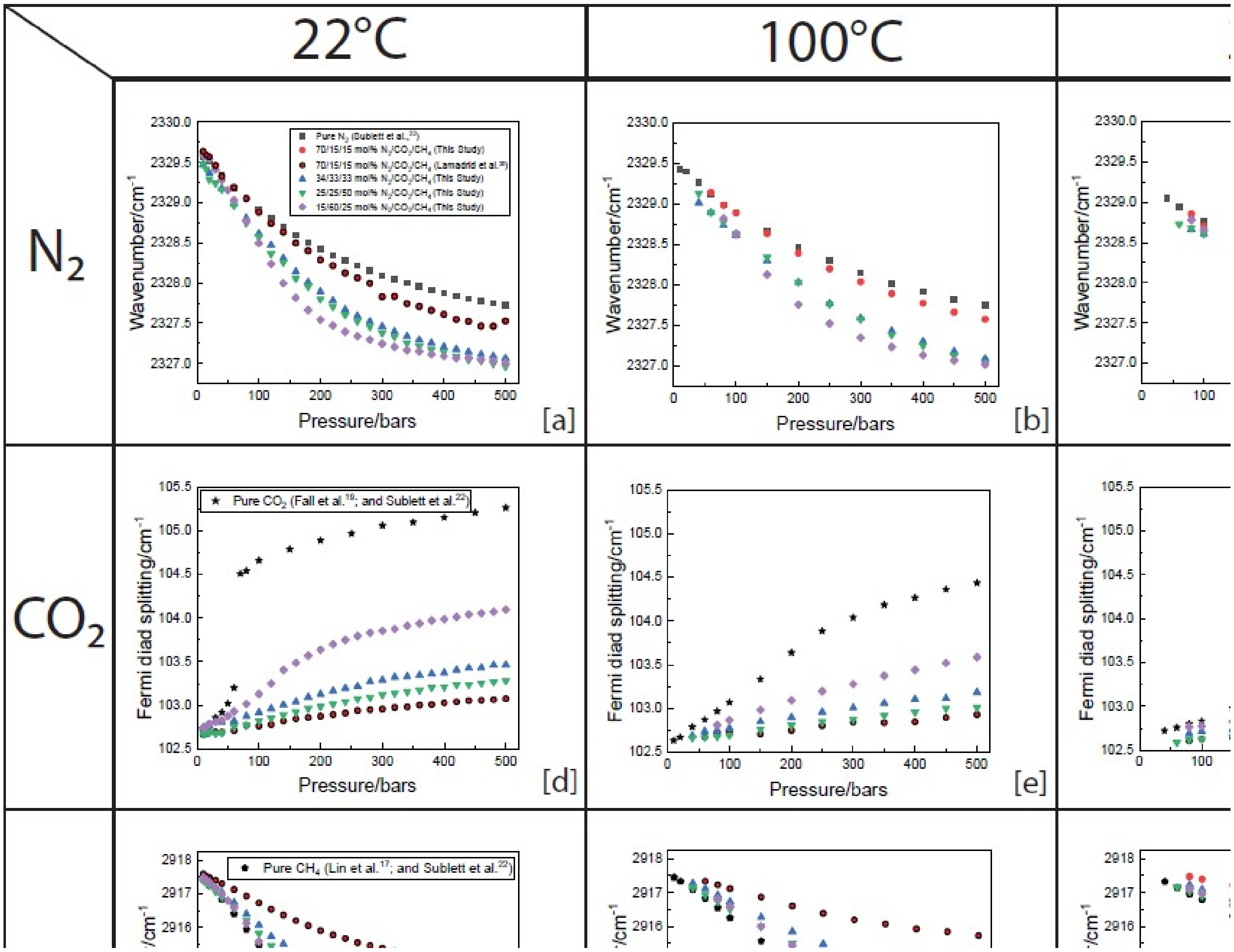

Fig. 2. Plots of pressure vs peak position/Fermi diad splitting for N_2 (a-c), CO_2 (d-f), and CH_4 (g-i) at 22°C, 100°C, and 200°C for the pure systems and ternary gas mixtures containing 70/15/15 mol%, 25/25/50 mol%, 15/60/25 mol%, and 34/33/33 mol% $N_2/CO_2/CH_4$. Peak position data for pure N_2 is from Sublett et al.[22], for pure CH_4 is from Lin et al.[17] and Sublett et al.[22], for pure CO_2 is from Fall et al.[19] and Sublett et al.[22], and for the 70/15/15 mol% $N_2/CO_2/CH_4$ gas mixture at 22°C is from Lamadrid et al.[20].

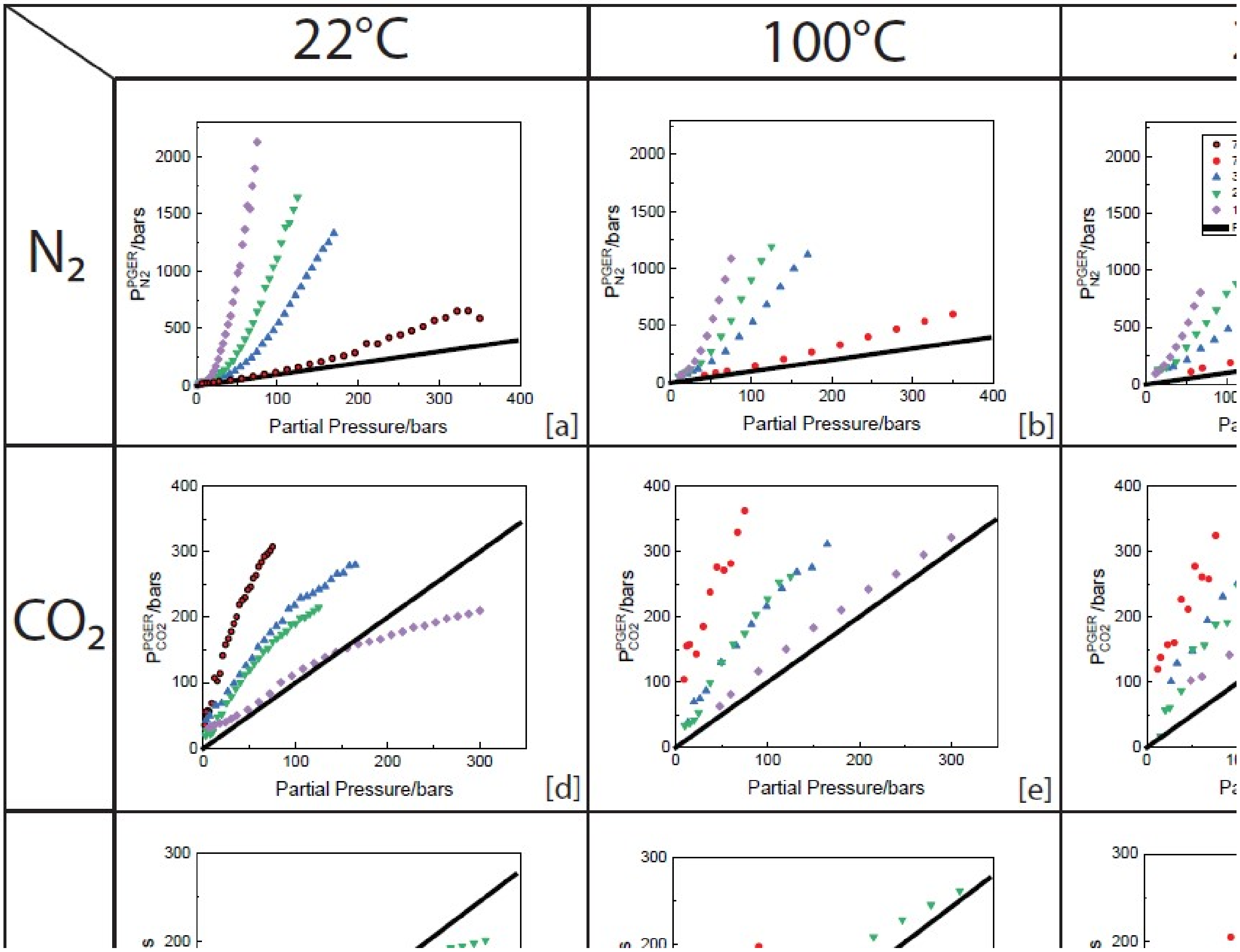

Fig. 3. Plots of partial pressure determined from Eq. 1 vs the pure gas equivalent Raman pressure (P_i^{PGER}) for N$_2$ (a-c), CO$_2$ (d-f), and CH$_4$ (g-i) at 22°C, 100°C, and 200°C for the pure systems and ternary gas mixtures containing 70/15/15 mol%, 25/25/50 mol%, 15/60/25 mol%, and 34/33/33 mol% N$_2$/CO$_2$/CH$_4$. P_i^{PGER} was calculated using the barometers of Sublett et al.^{22}. Peak position data used to calculate P_i^{PGER} for the 70/15/15 mol% N$_2$/CO$_2$/CH$_4$ gas mixture at 22°C is from Lamadrid et al.^{20}. The solid black lines represent where the partial pressure of a given component and P_i^{PGER} are equivalent.

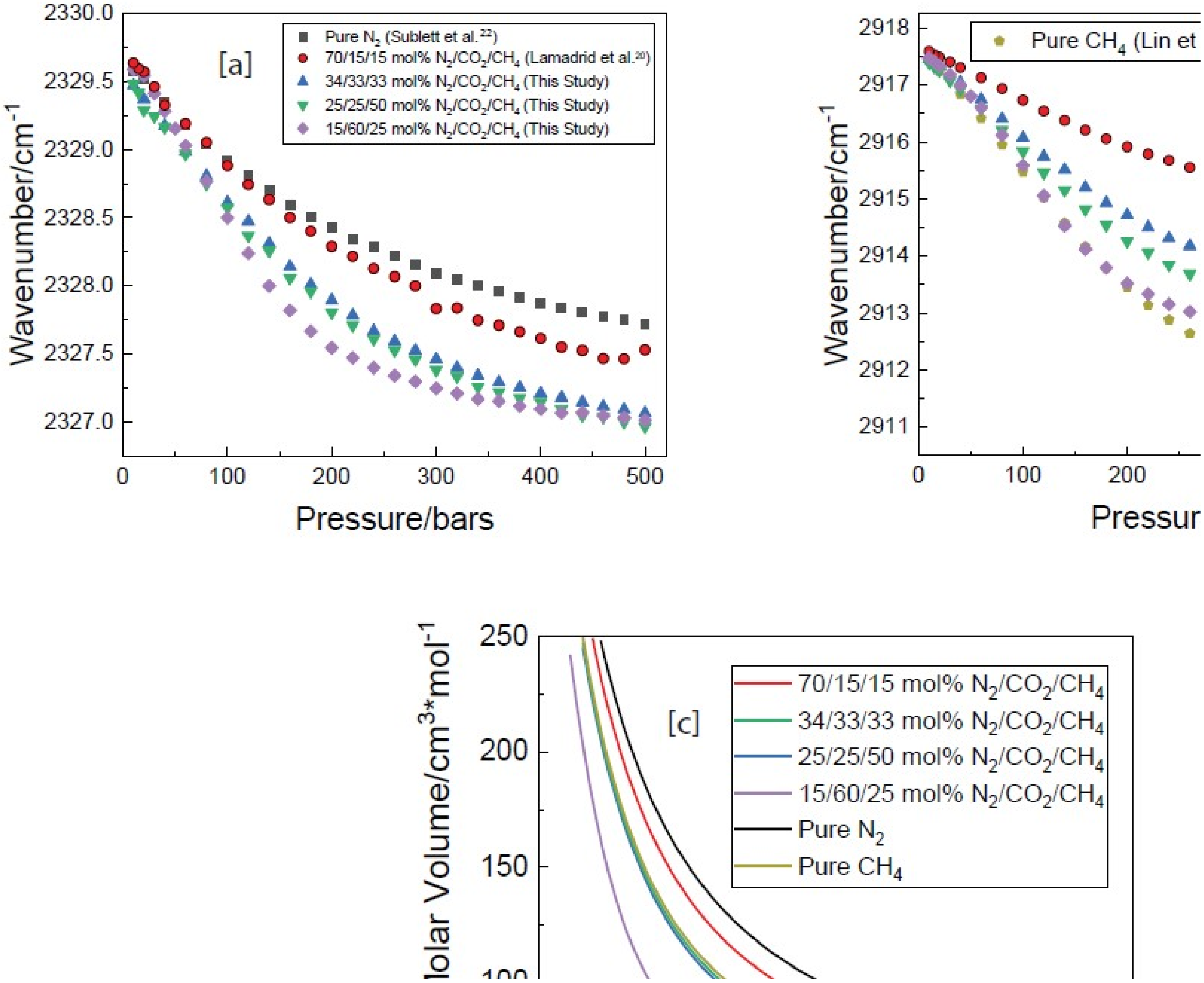

Fig. 4. Pressure-peak position plots at 22°C from Fig.1a and 1g for N_2 (a) and CH_4 (b), respectively, and a plot of pressure vs the total molar volume at 22°C of pure N_2, pure CH_4, and the gas mixtures measured in this study (c). The molar volumes of the gas mixtures are calculated using the NIST REFPROP version 10.0 program[49] and the GERG2008 EOS[50], and the molar volumes of pure CH_4 and pure N_2 are calculated using the Setzmann and Wagner[51] and Span et al.[52] EOS, respectively.

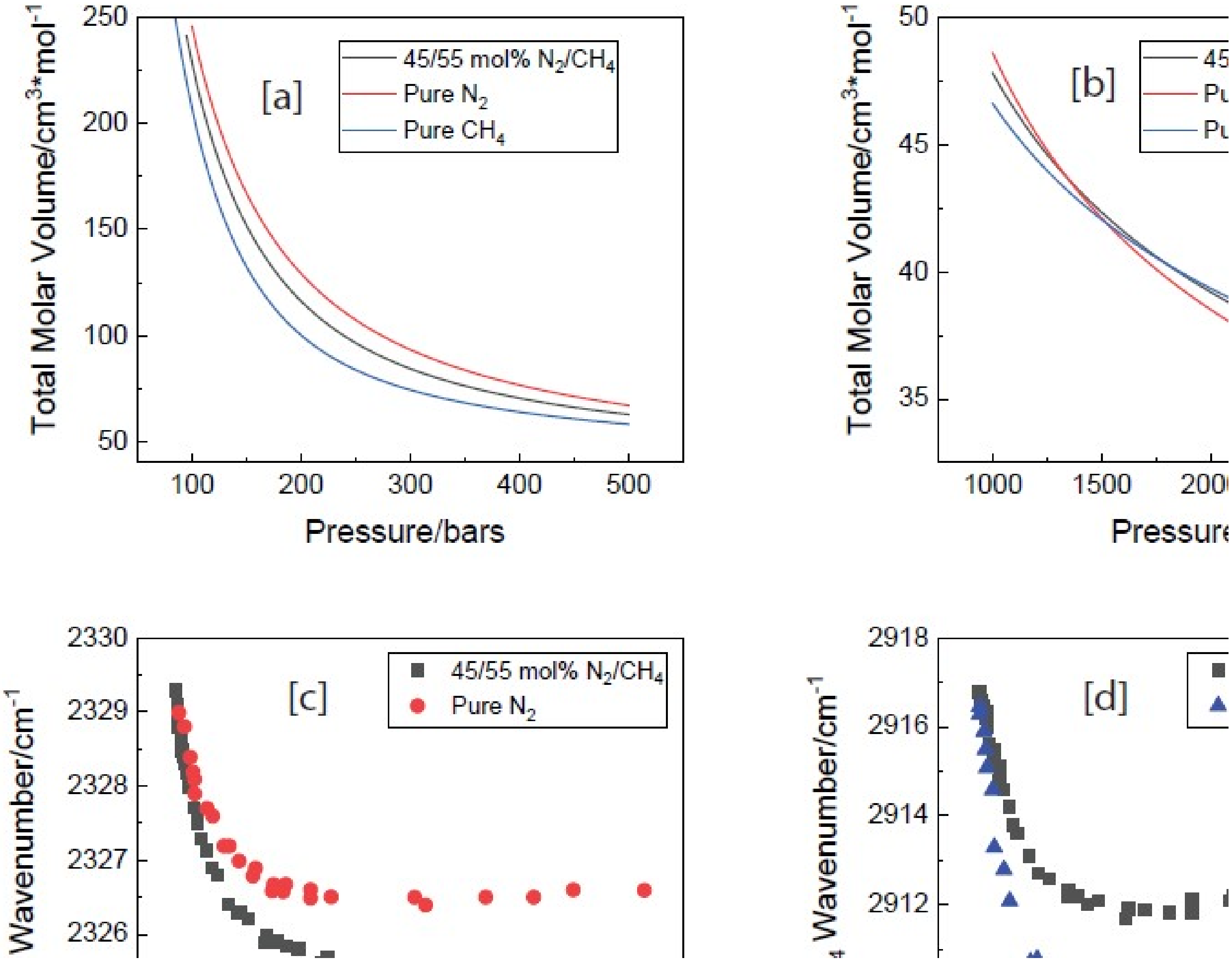

Fig. 5: Plots of pressure vs the molar volumes at 22°C of pure N_2[49, 52], pure CH_4[49, 51], and a 45/55 mol% N_2/CH_4 mixture[49-50] from 100-500 bars (a) and 1000-3000 bars (b), along with the peak position data from Fabre and Oksengorn[16] for the peak positions of N_2 (c) in the pure system and the 45/55 mol% N_2/CH_4 mixture and the peak positions of CH_4 (d) in the pure system and the 45/55 mol% N_2/CH_4 mixture at 22°C. Note that the pressures in which the peak positions of N_2 and CH_4 stop decreasing with increasing pressure (isothermal inflection pressure) roughly corresponds with the pressure in which the pure component molar volume isotherms cross the mixture molar volume isotherm.

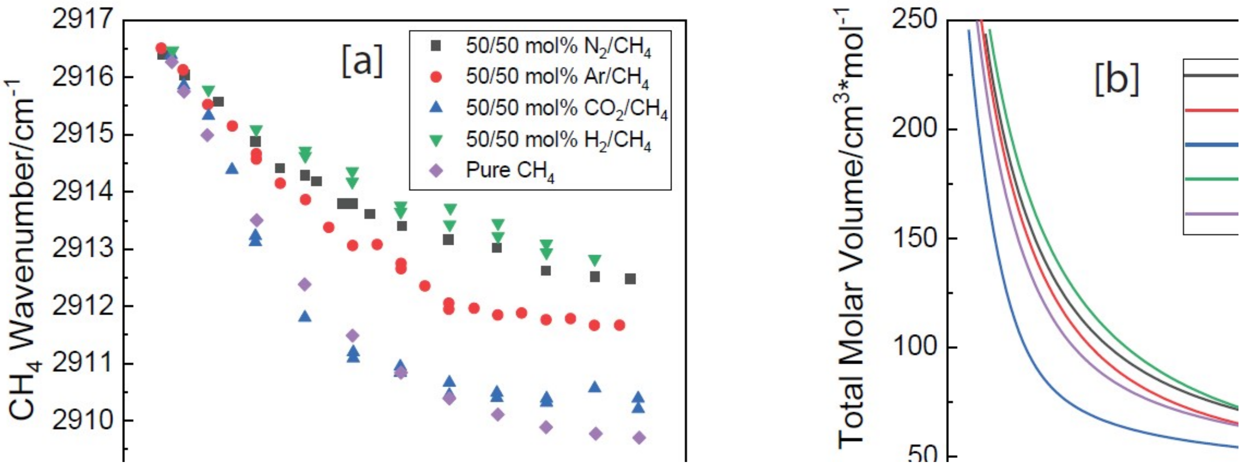

Fig. 6: Plots of the pressure vs CH_4 peak position (a) and pressure vs total molar volume (b) of pure CH_4[49, 51] and 50/50 mol% N_2/CH_4, Ar/CH_4, CO_2/CH_4, and H_2/CH_4 mixtures[49-50] at 22°C. Peak positions for CH_4 in the pure system and mixtures are from Seitz et al.[29].

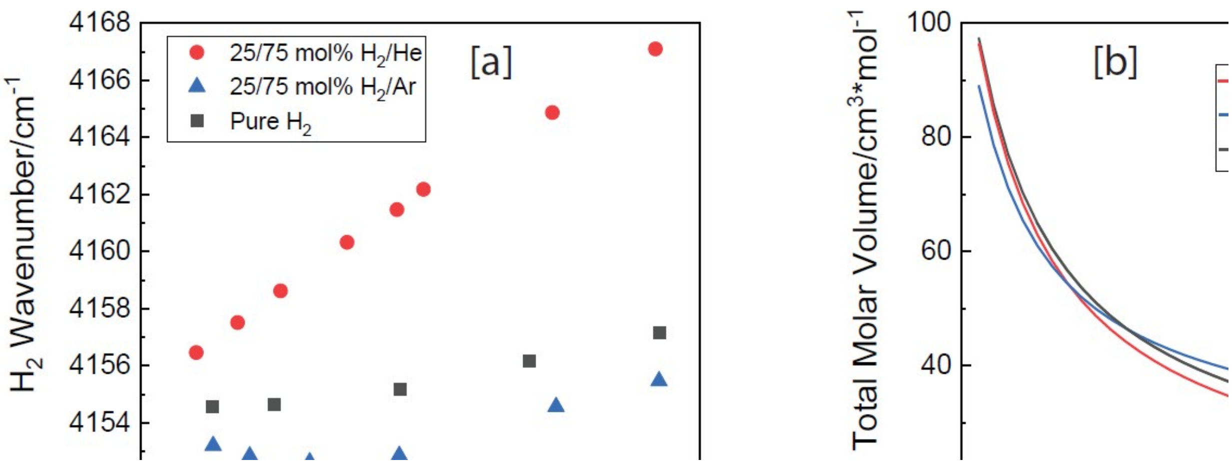

Fig. 7: Plots of the pressure vs H_2 peak position (a) and pressure vs total molar volume (b) of pure H_2[49, 53] and ~25/75 mol% H_2/Ar and H_2/He mixtures[49-50] at 22°C. Peak positions for H_2 in the pure system and mixtures are from May et al.[43].

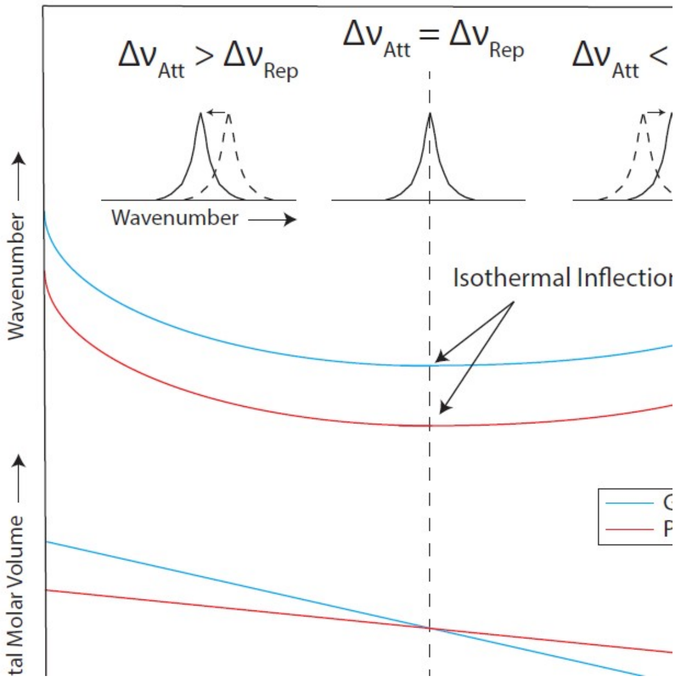

Fig. 8: Schematic isothermal plot of pressure vs peak position and total molar volume of an example gas mixture (blue line) and pure gas (red line) to serve as a summary of the observations made in section 4.1.1. The dashed line represents the point at which the contributions to peak shift by attraction ($\Delta\nu_{Att}$) and repulsion ($\Delta\nu_{Rep}$) are equivalent (isothermal inflection pressure). The isothermal inflection pressure roughly corresponds with the pressure at which the molar volume isotherms cross. At pressures less than this pressure, peak position decreases with increasing pressure, and at pressures greater than this pressure, peak position increases with increasing pressure. This is exemplified by the solid and dashed example Raman peaks provided at the top of the diagram. The dashed peak represents where the peak started at some pressure and the solid peak represents where the peak is located after an increase in pressure. In the region where the attractive contribution to peak shift is greater than the repulsive contribution to peak shift (left of the dashed line), larger molar volumes correspond with higher peak position values at a given pressure relative to lower molar volumes. In the region where the repulsive contribution to peak shift is greater than the attractive contribution to peak shift (right of the dashed line), larger molar volumes correspond with lower peak position values at a given pressure relative to lower molar volumes.

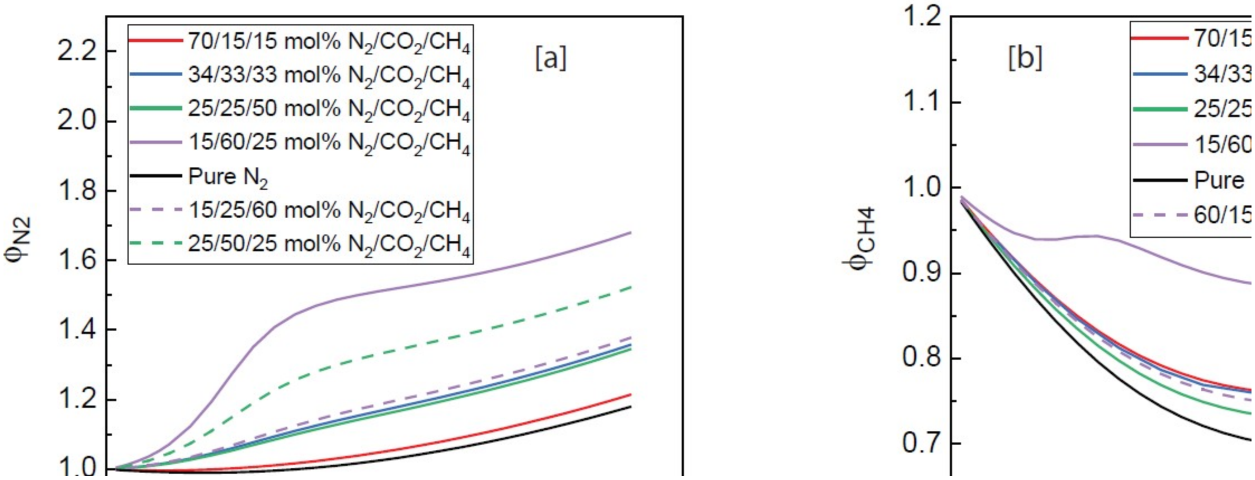

Fig. 9: Plots of pressure vs the fugacity coefficients of N_2 (a) and CH_4 (b) at 22°C for the pure systems and mixtures in this study. Fugacity coefficients of N_2 and CH_4 in the gas mixtures are calculated using the NIST REFPROP version 10.0 program[49] and the GERG2008 EOS[50], and the fugacity coefficients of pure CH_4 and pure N_2 are calculated using the Setzmann and Wagner[51] and Span et al.[52] EOS, respectively.

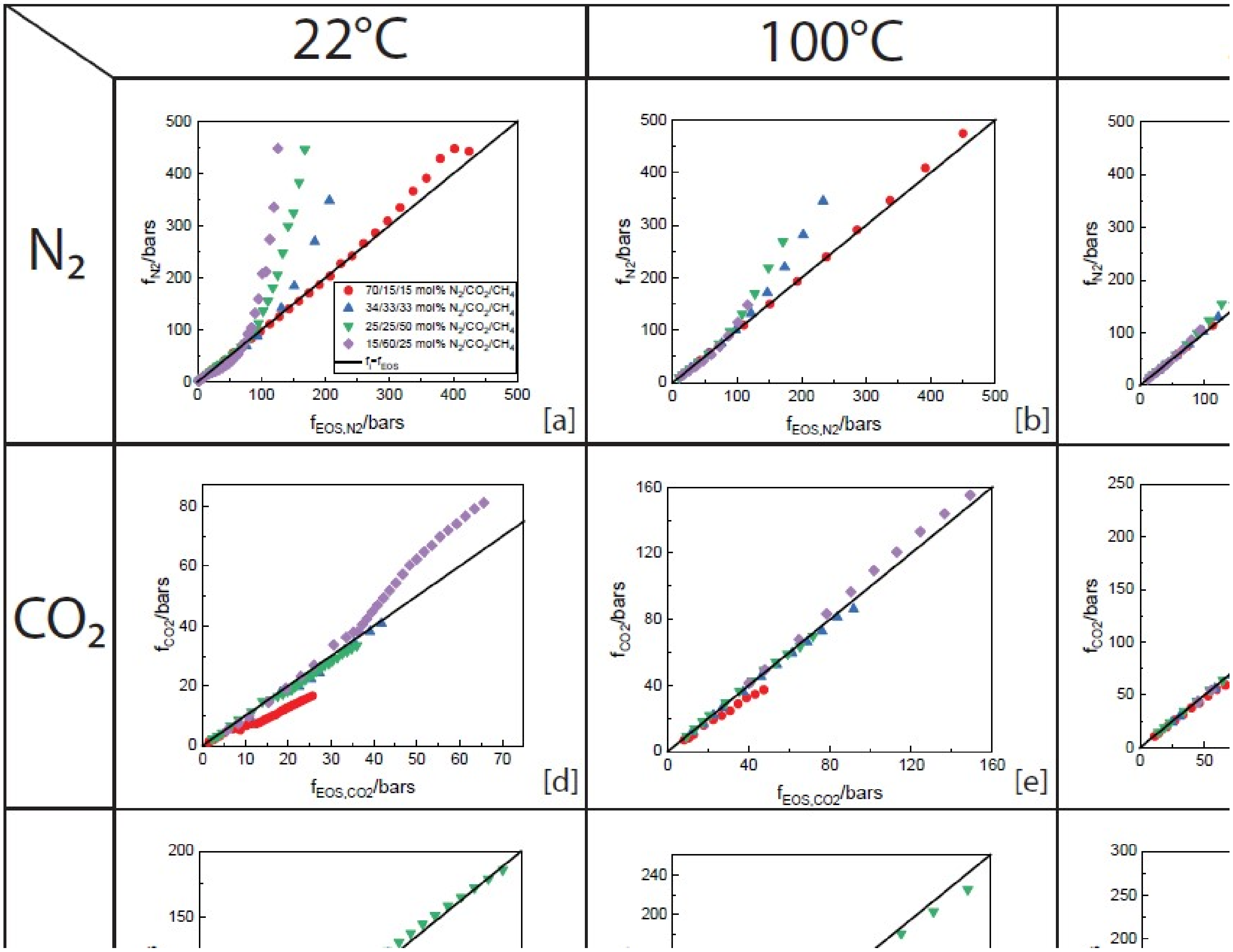

Fig. 10: Plots of fugacity determined from the GERG2008 EOS[50] (f_{EOS}) vs the fugacity determined by the relationship developed by Lamadrid et al.[20] (f_i, Eq. 1) for N_2 (a-c), CO_2 (d-f), and CH_4 (g-i) at 22°C, 100°C, and 200°C for the gas mixtures in this study. The solid black lines indicate where f_{EOS} and f_i are equivalent.

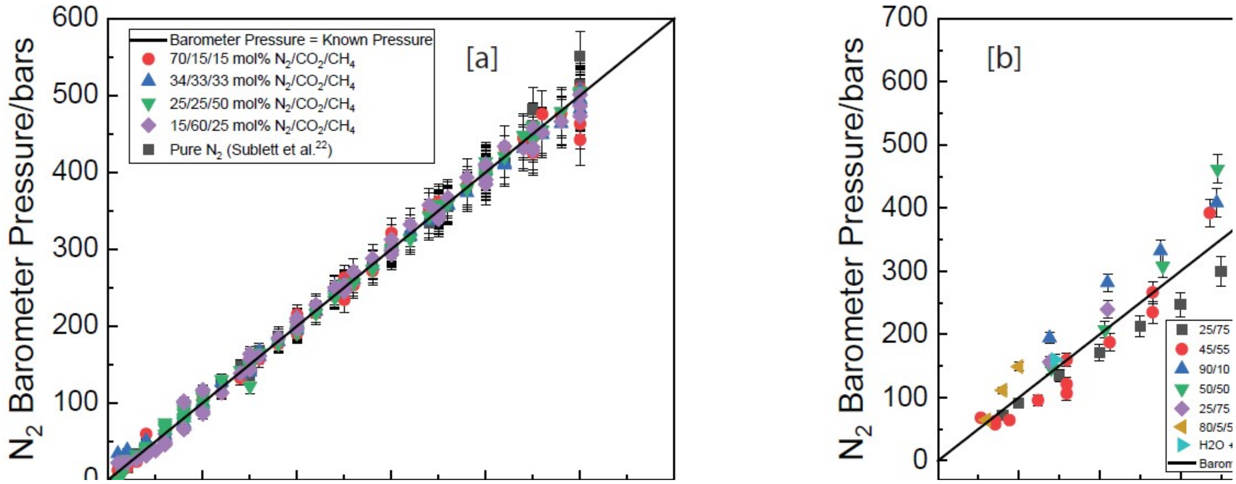

Fig. 11: (a) Plot of the known total pressure of the gas mixtures and pure N_2 vs the pressure of the gas mixture and pure N_2 calculated using the peak position of N_2 (Eq. 4). This is provided to demonstrate the quality of the fit as all of these data points were used in developing the fit. (b) Plot of the known total pressure of gas mixtures of 25/75 mol% N_2/CH_4 (measured in this study), 45/55 mol% N_2/CH_4 (Fabre and Oksengorn[16]), 90/10 and 25/75 mol% N_2/CH_4 (Seitz et al.[30]), 50/50 mol% N_2/CH_4 (Seitz et al.[29]), 80/5/5/5/5 mol% $N_2/CH_4/C_3H_8/C_4H_{10}/C_2H_6$ (measured in this study), and an SFI containing an H_2O rich liquid phase and a 24/69/7 mol% $N_2/CO_2/CH_4$ vapor bubble at room temperature (measured in this study) vs the pressure of the gas mixtures calculated using the peak position of N_2 in the mixtures (Eq. 4).

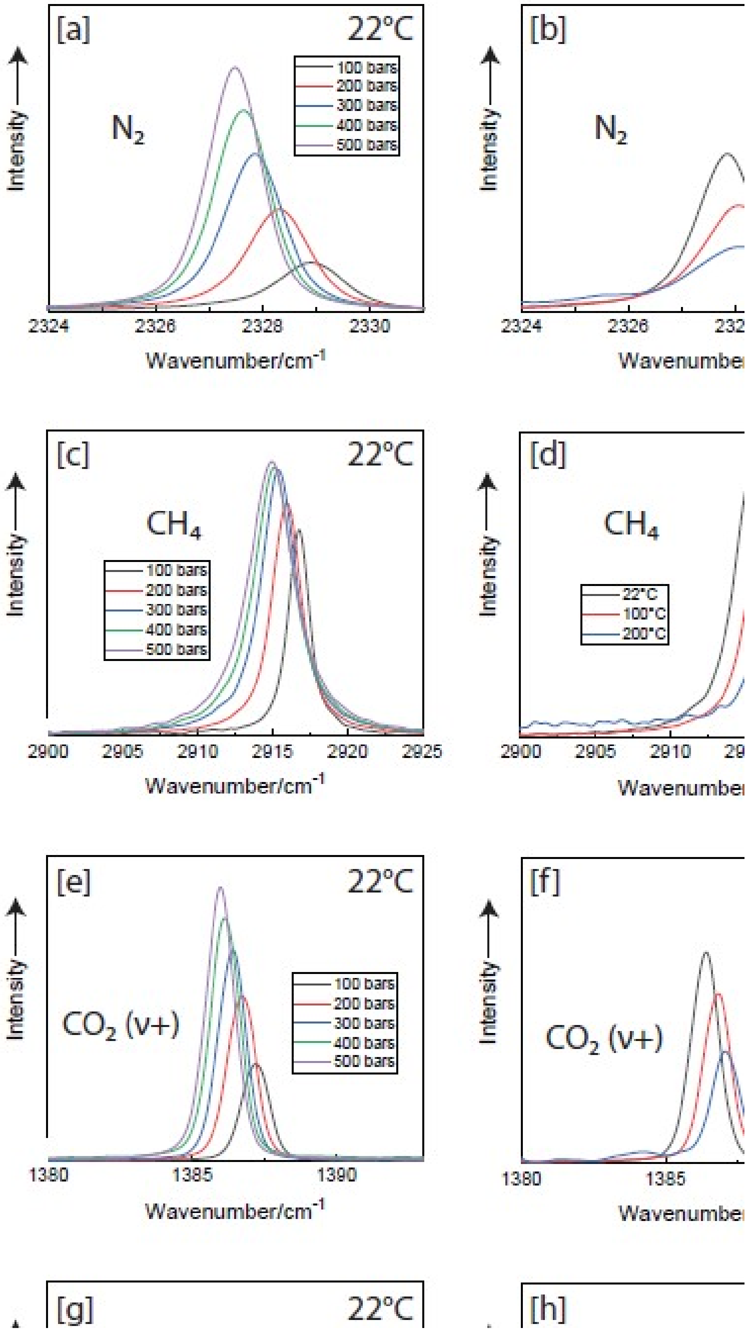

Fig. S1: Plot of wavenumber of the Raman peak of N_2, CH_4, and the more intense (*v*+) and less intense (*v*-) peaks that make up the Fermi diad for CO_2 vs intensity from 100-500 bars at 22°C and from 22-200°C at 300 bars for the 70/15/15 mol% $N_2/CO_2/CH_4$ gas mixture. The collection times for N_2, CO_2, and CH_4 are 20s, 30s, and 20s, respectively.

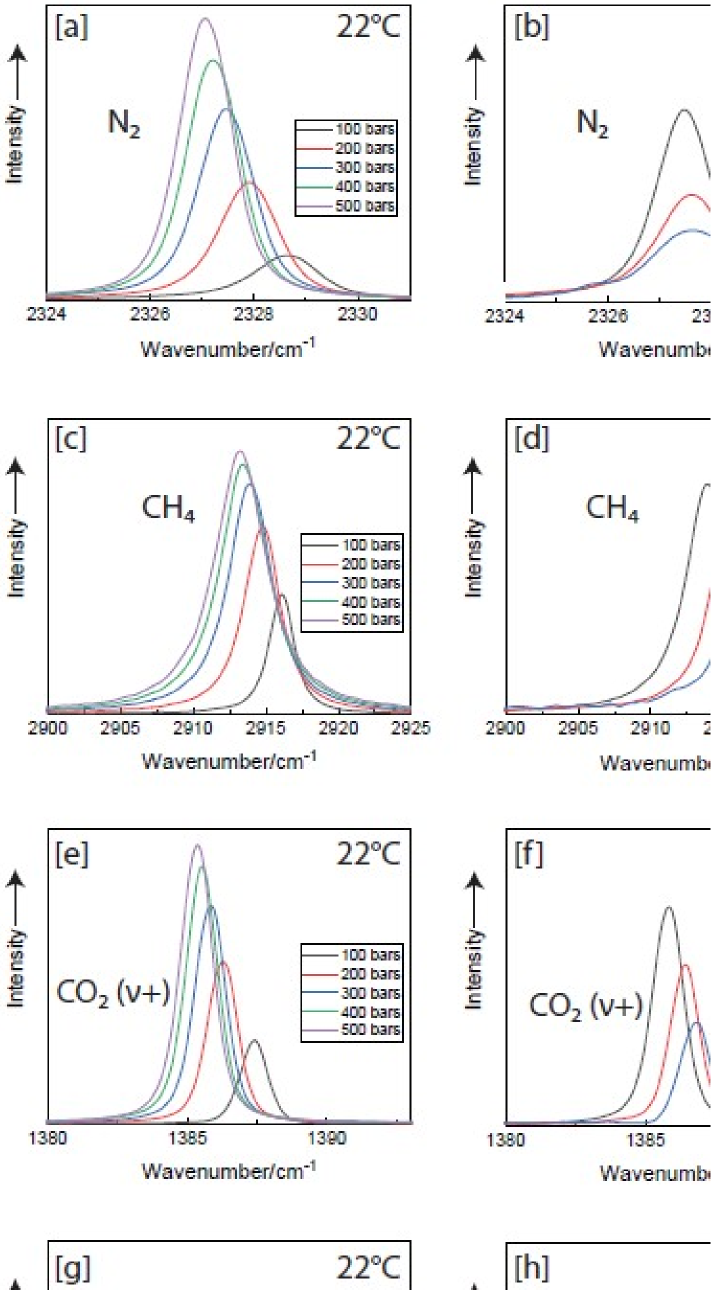

Fig. S2: Plot of wavenumber of the Raman peak of N_2, CH_4, and the more intense (*v*+) and less intense (*v*-) peaks that make up the Fermi diad for CO_2 vs intensity from 100-500 bars at 22°C and from 22-200°C at 300 bars for the 34/33/33 mol% $N_2/CO_2/CH_4$ gas mixture. The collection times for N_2, CO_2, and CH_4 are 60s, 60s, and 20s, respectively.

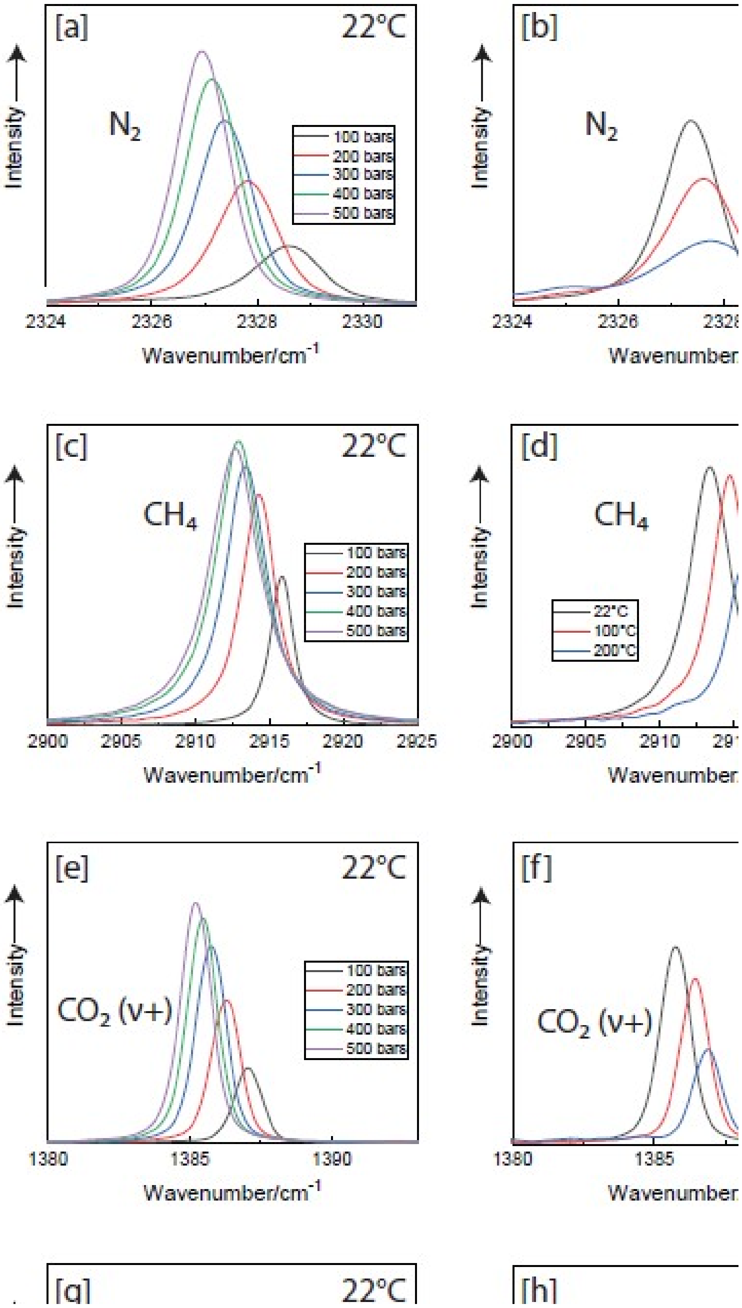

Fig. S3: Plot of wavenumber of the Raman peak of N_2, CH_4, and the more intense (v+) and less intense (v-) peaks that make up the Fermi diad for CO_2 vs intensity from 100-500 bars at 22°C and from 22-200°C at 300 bars for the 25/25/50 mol% N_2/CO_2/CH_4 gas mixture. The collection times for N_2, CO_2, and CH_4 are 30s, 30s, and 20s, respectively.

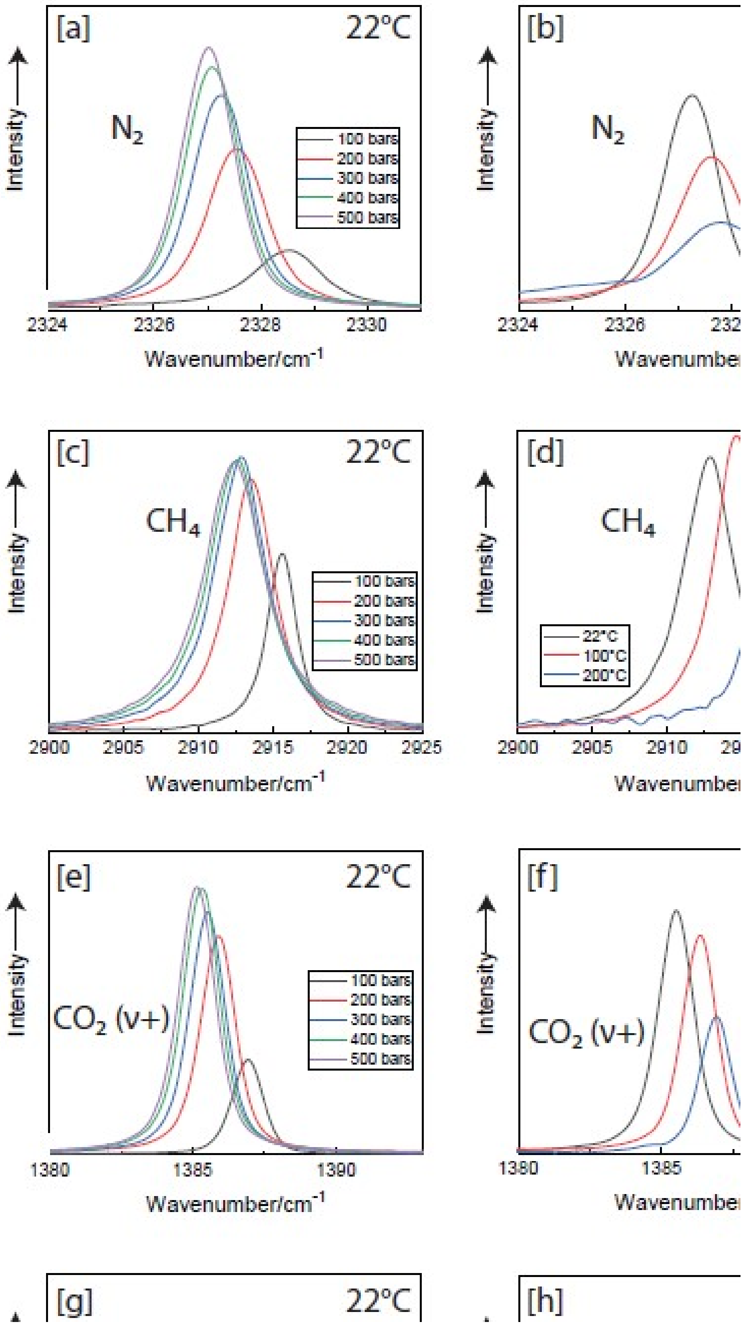

Fig. S4: Plot of wavenumber of the Raman peak of N_2, CH_4, and the more intense (*ν*+) and less intense (*ν*-) peaks that make up the Fermi diad for CO_2 vs intensity from 100-500 bars at 22°C and from 22-200°C at 300 bars for the 15/60/25 mol% $N_2/CO_2/CH_4$ gas mixture. The collection times for N_2, CO_2, and CH_4 are 60s, 30s, and 20s, respectively.

Tables

Table 1: Fitting coefficients for the N_2 mixture barometer (Eq. 4).

$A_{i,j,k}$	**Value**	**Error (±)**
1,0,0	-3.072	0.248
1,1,0	-4.683	0.914
1,4,0	-10.99	1.74
1,0,1	-1.4359	0.0856
2,0,0	9.929	0.961
2,1,0	-12.81	4.20
2,4,0	45.13	9.74
2,0,1	-4.454	0.676
2,0,2	1.290	0.233
3,0,0	-95.6	10.7
3,0,1	4.975	0.952
3,1,0	879	129
3,2,0	-3032	520
3,3,0	4090	781
3,4,0	-1905	383
4,0,0	187.6	22.4
4,1,0	-2019	282
4,2,0	7250	1160
4,3,0	-9890	1750
4,4,0	4514	851
0,1,0	18.479	0.522
0,1,2	-21.10	1.37
0,1,3	4.828	0.327
0,2,0	-55.89	3.19
0,2,2	38.07	4.69
0,3,0	70.56	5.68
0,3,1	40.30	2.70
0,3,2	-68.12	6.64
0,4,0	-32.91	2.91
0,4,2	-48.95	5.95
0,4,3	80.26	5.56
0,4,4	-22.55	1.57
0,0,2	4.168	0.175
0,0,3	-1.4064	0.0730